Synthesis of Copper based Nanowires for Optoelectronics and Electrochemical Applications

Assia Kasdi
Corpus Christi College

A thesis submitted in fulfilment of requirement for the degree of
DPhil in Materials at **the University of Oxford**

Abstract

This thesis introduces new methodologies for the synthesis of copper Nanowires (CuNW) with high aspect ratio as well as copper nickel (CuNi) alloyed and core-shell NW with enhanced resistance to oxidation. The potential applications of Cu-based NW as Transparent Conductors (TC) and as electrocatalysts for the Hydrogen Evolution Reaction (HER) are also investigated.

The effect of the addition of alkane and alkene non-coordinating solvents with a range of carbon chains- from C8 to C18- on the NW aspect ratio was investigated, using Scanning Electron Microscopy (SEM) and Fourier Transform Infra-Red (FTIR) spectroscopy. It was also established that non-coordinating solvents such as alkanes and alkenes tune the reactivity between the copper precursor and the capping ligand oleylamine (OLA). It was found that the chain length, the bond saturation as well as the concentration of the solvent have an effect on the NW aspect ratio. The addition of middle chain C12 alkane, dodecane, and long chain C18 alkene 1-octadecene (ODE) produced NW with the best aspect ratios reaching 800 and 1100 respectively. An optimal aspect ratio was attained for an ODE:OLA ratio of 1:4.

CuNW transparent conductors (TC) films were fabricated. Treatments including lactic acid ligand exchange on NW, plasma and anneal pre- and post-treatments on thin films were carried out. It was found that a combination of a lactic acid ligand exchange followed by an H_2/N_2 plasma treatment gave the

best optoelectronic performances with films presenting a sheet resistance Rs of 43 Ω/□ for a transmittance of 93%. The addition of a top layer was investigated to improve the resistance to oxidation of CuNW films. Different layers of coatings were compared, and it was found that 2 layers of ZnO stabilise the NW electrical properties for 50 days with a Rs of 27.5 Ω/□ for 76% transmittance.

CuNW were turned into bimetallic CuNi NW by transforming the original seed-mediated growth synthesis into a co-reduction method, using Zn^{2+} salts as catalyst for the reduction of both Cu and Ni precursors. It was found that the concentration of Zn precursor was critical to reduce Ni precursor into metallic Ni effectively. The counterion effect was also investigated: it was found that the presence of acetylacetonate ions resulted in the formation of core-shell NW preferentially while chloride ions favoured the formation of alloys. A mechanism for both CuNi core-shell and alloy formation was proposed. Structural differences between core-shell and alloys were studied using Scanning Transmission Electron Microscopy (STEM), TEM and X-Ray Powder Diffraction (XRD) analyses. The STEM study also showed that both bimetallic NW possess an oxide that reveals to be of a diffusive nature for core-shell NW and a protective nature for alloyed NW.

NW were investigated as potential electrocatalysts for HER. It was shown that core-shell NW have activities similar to NiNW ones. 1:1 Cu:Ni NW activity surpassed both CuNW and NiNW activities with a Tafel slope as low as 21 mV/decade and a current density of 0.31 mA/cm^2, values similar to the ones

exhibited by Platinum (Pt), therefore hailing a milestone in low-cost electrocatalyst for HER applications.

Acknowledgments

I would like to thank my supervisor Professor Andrew Watt for welcoming me in his lab and for his guidance and support to my research, especially when I embarked into the long journey of making alloy nanowires. I would like to thank Professor Hazel Assender for her support, valuable suggestions and feedback in meetings. I would like to thank Professor Nicole Grobert for having been such an amazing college advisor and always offering her help when needed. I would also like Professor Ian Thompson for allowing me to use his lab equipment and being always available when needed. I would like to thank Professor Nik Petrinic and all his team for their support and for always making me feel welcome in their lab. I thank Professor Mauro Pasta for helping me carrying experimental work in his lab and in particular for his help with the electrochemical experiments.

I would like to thank the Engineering and Physical Science Research Council for funding my PhD. I would also like to thank the Materials department and my college Corpus Christi for funding my conferences fees. I thank Dr Adrian Taylor, Marion Beckett and Rachel Pearson for their support and for being always available and helpful when needed.

Special thanks go to the characterisation teams in Begbroke. I would like to thank Dr Neil Young, Jennifer Holter, Greg Cook, Chris Salter, Dr Susan Warren and Dr Colin Johnston for training me in various instruments. Special thoughts

go to the late Gabriella Chapman, whom I will always remember for her constant help with the SEM.

I would like to thank past and current members, visitors and interns that made the lab such a happy and lively environment. I wish to all of you Nina, Zhanet, Nanlin, Yujiro, Wing and Daniel good luck for your thesis. Good luck in your studies to both of you, Claire and Solène, it was my great pleasure to mentor you during your stay with us.

I would like to thank Inji Yeom for having shared lab works, talks and for having been a close lab mate for all these years. I will always remember our trips with the little Honda.

Outside the lab, I would like to thank all of you that made my PhD time brighter. Lila for being the perfect best friend, Nataliia for our most insightful conversations around coffees , Maria for being the best travel and fitness companion, Cordelia and the hours we have spent theorising about cosmetics formulations, Lakshmi for being full of strength and positivity, Anissa my dance buddy, Lola and her wonderful wit, and many others. I will always cherish our conversations.

I would like to thank my parents and my three amazing brother and sisters for their love and support. Bien que très certainement vous ne lirez que quelques pages de cette thèse, je vous la dédie du fond du cœur car vous avez toujours été ma première source d'inspiration.

Finally, I would like to thank my fantastic boyfriend for having always been by my side, for his positivity and being the best mbare I could wish for. Sarò sempre grata del tuo constante support durante il moi dottorato.

"The voyage of discovery is not in seeking new landscapes but in having new eyes", Marcel Proust

Statement of originality

This thesis is an account of work carried out by the author in the Department of Materials, the University of Oxford under the supervision of Professor Andrew Watt. Any work of others that has been utilised, directly or indirectly, is duly acknowledged in the text, and a list of references is presented at the end of the thesis. No part of this thesis has been submitted towards the completion of another degree at the University of Oxford or elsewhere. Parts of the thesis have been submitted to or published in the following conference presentations:

A. Kasdi, C. Neo, J.H. Warner, A.A.R. Watt, **Copper nanowires in solar cell devices**, Nanowires 2014, Eindhoven, August 2014 (poster presentation).

A. Kasdi, J.H. Warner, A.A.R. Watt, **Copper nanowires transparent conductors**, E-MRS fall meeting, Warsaw, September 2015 (oral presentation).

Oxford University Innovation Limited, **Nanostructures and process for production**, Patent filling number 1805662.2.

Signed…… Date……

Contents

List of tables

List of figures

List of abbreviations

ODE	1-Octadecene
Acac	Acetylacetonate
AF	Area Fraction
Br^-	Bromide
CTAB	Cetrimonium Bromide
Cl^-	Chloride
Cu	Copper
EDX	Energy Dispersive X-Ray
FFT	Fast Fourier Transform
FTIR	Fourier Transform Infra-Red
Au	Gold
HDA	Hexadecylamine
HRTEM	High-Resolution Transmission Electron Microscopy
HER	Hydrogen Evolution Reaction
LSV	Linear Scan Voltammetry
NC	Nanocrystal
NP	Nanoparticle
NW	Nanowire(s)
Ni	Nickel
ODE	1-octadecene
OLA	Oleylamine
PEDOT: PSS	Poly(3,4-ethylenedioxythiophene) polystyrene sulfonate
Pt	Platinum
PVP	Polyvinylpyrrolidone
SEM	Scanning Electron Microscopy
STEM	Scanning Transmission Electron Microscopy
R_s	Sheet resistance
Ag	Silver
SPR	Surface Plasmon Resonance
TC	Transparent Conductors
XRD	X-Ray Powder Diffraction
Zn	Zinc
ZnO	Zinc oxide

1 Introduction

1.1 Nanoparticles and nanowires

The use of metallic nanoparticles (NPs) has been reported since the Antiquity where their exceptional properties were already exploited. A remarkable example is the Lycurgus Cup (Figure 1) manufactured by the Romans in the 4th century [1]. This cup made of a silver-gold alloy has the propriety to change colour depending on how it is illuminated: if the cup is seen with a reflective light such as the daylight, it appears green, if it is observed with a light coming from the inside of the cup (transmitted light), then it appears red.

Figure 1 The Lycurgus cup in British Museum dated back to the IVth century. On the left, the cup is illuminated with an external light such as daylight. On the right, the light is illuminated from the inside of the cup and transmitted through it [1].

At the beginning of the 20th century, researchers have started investigating the size-related properties of NPs: several decades of research efforts have led to

various synthetic approaches which have promoted the formation of NPs with a plethora of morphologies such as nanocubes, nanorods and nanowires (NW) for instance. NW are 1D dimensional NPs whose diameter is confined to the nanoscale while the length can reach up to 100 μm. The first reports of man-made 1-D materials can be tracked back to the 1940's [2] where they were firstly reported in the literature as "whiskers": cadmium[3] and tin[4] NW were already observed on metallic surfaces. Since then, a great deal of effort has been placed on developing solution-phase NW syntheses capable of controlling both their size and chemical nature to tune their properties. In only two decades, thanks to the effort of many research groups, a broad range of NW have been synthesised, well-suited for industrially relevant applications in photonics, electronics, energy as well as in several electrochemical reactions. Attaining a more precise control of NW morphology, composition and structure while pushing the research away from expensive metals are nowadays big challenges to solve in order to exploit further NW exceptional properties.

1.2 Aim of the thesis

Despite the numerous strategies developed in the last decades, metallic NW syntheses still suffer from polydispersity and poor repeatability. In addition to that, the pursuit of low-cost alternatives to noble metallic NW has opened up new issues: copper presents the advantage of being nearly as conductive as silver while being much cheaper but copper (Cu) suffers from its intrinsic oxidation. Even though, CuNW have shown a great potential as low-cost alternative technologies for several applications owing their excellent

optoelectronic properties, it remains however a challenge to retain their film performances. Therefore, the goal of this thesis is to show how a better understanding of the fundamental chemistry involved during NW synthesis can tune the size and chemical nature of CuNW with an enhancement of their properties. This thesis introduces for the first time the synthesis of CuNi alloyed NW with enhanced performances as catalysts for HER. The thesis will also address the following questions:

- Can the overall NW size and composition be tuned by modifying the dynamic between precursors and ligands with the addition of either non-coordinating solvents or other metallic precursors?
- Can the modification of the NW surface chemistry via ligand exchange improve the optoelectronic properties of CuNW films?
- Can the addition of a coating on top of CuNW improve their stability over time?
- Can the transition between CuNW to Cu based NW improve their electrocatalytic properties?

1.3 Structure of the thesis

Chapter 2 provides a literature review which covers the theory behind metallic NW synthesis and TC as well as the recent advances in syntheses, properties and applications of metallic NW and NPs. Chapter 3 details the techniques used for materials synthesis, characterisation and thin film fabrication. Chapter 4 treats the influence of the addition of a non-coordinating solvent on CuNW final length and diameter and a mechanism of

reaction will be proposed as well. Chapter 5 focuses on CuNW thin film fabrication. An optimisation of the thin film stability will be shown. Chapter 6 will show how the addition of a Zn precursor in the synthesis turns monometallic CuNW into bimetallic CuNi NW. This chapter will demonstrate that the concentration of Zn as well as the precursor's counterion are crucial parameters that influence the NW size and nature. At the end of the chapter, the electrocatalytic activities of monometallic and bimetallic NW will be investigated. Chapter 7 ends the thesis on the conclusion and further work to be carried out.

2 Literature review

2.1 Application of copper NW as transparent conductors.

2.1.1 Theory of transparent conductors

TC electrodes have gained increasing attention as essential components in technologies such as displays [5,6] photovoltaic devices [7] and thermal control glass [8,9]. Typically, ternary and quaternary metal oxides are used as TC electrodes such as InGaZnO and Sn doped In_2O_3 commonly called ITO [10]. However, their application on flexible substrates is limited due to their brittle nature and cost. There is therefore a need to develop a TC technology that is low-cost, flexible and robust.

This chapter reviews NW TC fabrication and synthesis and understand how fields of chemistry, physics and engineering can be brought together. The underlying principles of TC, figures of merit, synthesis methodologies and state of the art applications of NW are now reviewed.

2.1.1.1 *Technical requirement*

A TC requires two paradoxical conditions: to be optically transparent and highly conductive [11]. For some optoelectronic applications, it is often required to have as much light transmitted as possible and therefore, it is ideal to have a transmittance superior to 90% and sheet resistance lower than 100 Ω/□ [12]. Usually, there is an inverted relation between conductivity and transmittance for a thin film because the more conductive the film, the thicker it is and

therefore less light will pass through it [13]. Therefore, a trade-off between these two parameters is often required. Other parameters need to be defined as well and will be established in the next sections.

2.1.1.2 *Conductivity of a material.*

The sheet resistance R_s is the best parameter to characterise the electrical properties of a TC. The sheet resistance is defined by [13]:

$$R_s = \frac{1}{\sigma t} \ (1)$$

Where t is the film thickness in cm and σ is the conductivity of the film in Ω/□. The sheet resistance units are in Ω/□ where the square area is independent of the dimensions of the film.

The sheet resistance depends on many parameters such as NW dimension, their aspect ratio, NW density area, the resistance of a single NW and wire to wire contact resistance. In the specific case of NW, R_s depends also on the NW diameter size: Bid *et al.* [14] have shown that R_s tend to decrease when AgNW are thinner. This result is applicable to all kinds of metallic NW including CuNW.

For a given NW aspect ratio and area density, the resistance of the wires is dominated by the junction resistance between two NW. It is thus very important to ensure that this resistance is the lowest possible. Different

techniques exist to reduce the junction resistance and will be detailed later in this chapter.

2.1.1.2.1 Optical properties

The control of optical properties of NW TC is very important although not very well studied. Since NW dimensions are very distinct from the one of continuous films, the measurement of the transmittance needs to take into account their unique feature such as the aspect ratio. One way to measure the absorbance of a nanowire mesh is to calculate what fraction of the surface is blocked by the nanowires.

The optical transmission T is given by:

$$T\ (\%) = \ 100 - a * AF \ (2)$$

Where T is the transmission of the light in %, a is the fitting parameter which is dependent on the NW diameter and optical properties and AF is the area fraction of the film covered by the NW. AF corresponds to the resulting absorbed light by a nanowire network, considering that the amount of light blocked by a single nanowire is equivalent to its geometrical cross-section. AF is defined as:

$$AF = N * L * D\ (3)$$

Where N is the number of nanowires per area, L is the length of nanowires and D the diameter of nanowires.

2.1.1.2.2 Relationship between optical and electrical properties of NW.

As mentioned earlier in this chapter, the transmittance and sheet resistance of the films are often the parameters chosen to compare the performances of different TC and plotted against each other in order to assess the optoelectronical performances. Figure 2 plots the optical transmittance at 550 nm versus the sheet resistance for an AgNW film. The trade-off between transmittance and conductivity for TC can be clearly observed: on the left side of the plot, the films are highly conductive but less optically transparent whereas on the right side, the opposite phenomenon is observed. The closer the curve is to the Y axis, the more ideal the performances of the TC are. Therefore, researchers need to focus on treatments that could improve these performances. These will be detailed later in this chapter.

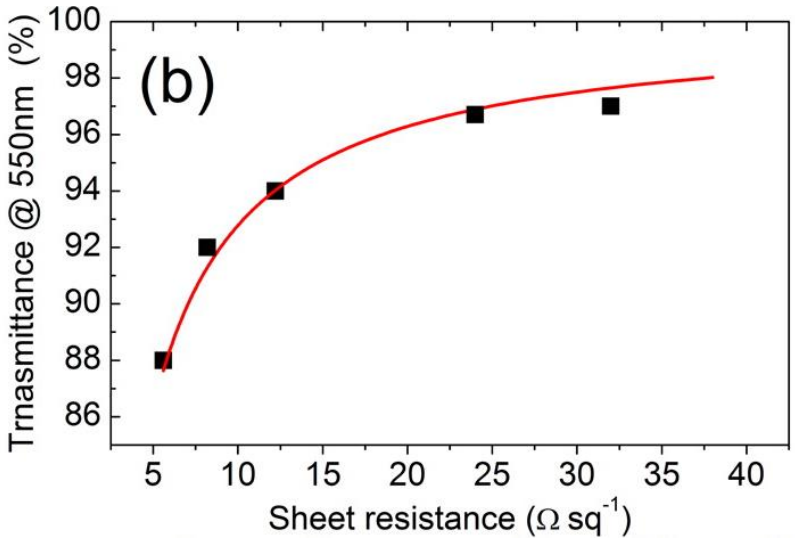

Figure 2. Plot of the optical transmittance at 550 nm versus the sheet resistance for an AgNW thin film.

The trade-off between the sheet resistance and the optical transmittance is often quantified as a figure of merit which is defined as the ratio σ_{op}/σ_{DC} in the Tinkham formula [15] :

$$T(\lambda) = \left(1 + \frac{Z_0}{2R_s}\frac{\sigma_{op}(\lambda)}{\sigma_{DC}}\right)^{-2} \quad (4)$$

Where $\sigma_{op}(\lambda)$ is the optical conductivity (at 550 nm) and σ_{DC} is the DC conductivity of the film [16,17], T is the transmittance of the film, Z_0 is the impedance of free space (377Ω) and R_s is the sheet resistance of the NW network.

2.1.1.2.3 Haze factor

The haze factor of the NW network is another important parameter to take into account. It is defined as [18]:

$$HF = \frac{I_s}{I_s + I_d} * 100\ (\%)\ \ (5)$$

Where HF is the haze factor and I_d and I_s are the light flux that are transmitted and scattered respectively. It is well known that NW are prone to scattering and therefore the haze factor is expected to be high for NW TC. Different research groups have shown that the haze factor is strongly dependent on the size of NW where HF increases with the diameter of NW [19,20]. The HF is a parameter that can be sometimes desired in applications such as photovoltaics where the scattered light can increase the amount of light received from the absorber layer [21]. However, in case of displays, the Haze effect needs to be avoided [22,23].

I have defined the parameters that are the most relevant for a TC. The next section will investigate the NW properties that make them suitable for TC applications.

2.1.2 NW as TC materials.

2.1.2.1 *Introduction*

Networks of metallic NW are very promising to replace ITO: researchers reported the fabrication of NW films with T ≥ 90% and R_s ≤ 100 Ω/ □, which is

comparable to ITO [24,25]. Noble metal NW have recently drawn an incredible amount of attention: unlike the other TC, metal NW deposition requires low-cost manufacturing process and is suitable for large-scale application [26]. This technology relies on the growth of thin, long, well dispersed [27] and pure metallic NW [12]. Many research group have reported the successful synthesis of gold NW (AuNW) [28,29], silver NW (AgNW) [30-32], iron NW (FeNW) [33] and nickel NW (NiNW) [34] for instance.

2.1.2.2 *Metallic NW as TC*

The synthesis of AuNW as thin as 5 nm [35] have been reported but these NW suffer from a rapid degradation [36] due to high surface to volume ratio. Among the metallic NW, AgNW TC are currently the most widespread technology [10,11] especially after the publication of the versatile polyol synthesis of AgNW by Sun *et al.* [30]. AgNW have achieved R_s that surpassed the one of ITO: the best electrodes exhibit R_s as low as 5-10 Ω/□ for a transmittance of 90% [24]. The advantage of these NW is that they are very stable and applicable to the large scale industry [37,38]. However, AgNW suffer from the high cost of Ag. Moreover, the results are not repeatable: the large diameter of NW (70-200nm) causes significant increase in the surface roughness [12] which is not desirable for TC applications. Electrical resistivity is in the long term increased due to the corrosion of Ag and nanosized metals in general [39,40]. These disadvantages need to be solved in order to promote the market of metallic NW based TC [41].

CuNW have garnered increasing attention in the last decade as a potential replacement for TC applications. Cu is nearly as conductive as Ag (only 6% less

conductive) but much more abundant (1000 times) and much cheaper [42]. Many researchers have reported that CuNW can achieve high optical transmittance with very low R_s [22,43,44]. However, some challenges still remain as Cu oxidises very quickly and quicker than Ag or Au. Therefore, ways of preventing this oxidation need to be explored in order to maintain the excellent properties of these NW. The next part will focus on the methods as well as the different mechanisms that drive CuNW synthesis.

2.2 NW synthesis

2.2.1 Introduction

NW are formed by the growth of assembled atoms either via organic chemical reactions (e.g. polymerization) or through inorganic atomic assembly, i.e. crystal nucleation, growth [45,46] or growth in a matrix [47-49].

In the last two decades, researchers have focused their attention in improving the techniques to synthesise metallic NW. Attention has mainly been focused on the so-called "soft" techniques which involve the presence of templates made of ligands, polymers and surfactants that promote the self-assembly of atoms, or their spontaneous organisation in liquid phase. The next section will review the theory behind NW growth and the different methods that fall under the soft template route.

2.2.1.1 *Mechanism of NW growth*

The control of the crystallisation steps (nucleation and crystal growth) is the essence of NW formation. Kinetic and thermodynamic parameters need to be precisely controlled so that the crystal will adopt the correct morphology and later, during the crystal growth, aggregation will be avoided [50].

2.2.1.2 *Nucleation theory*

Nucleation kinetic theory has been developed by Volmer in 1939 [51]. It is often admitted that the crystal nucleation process occurs in 3 main steps [52,53] represented in the model shown in Figure 3.

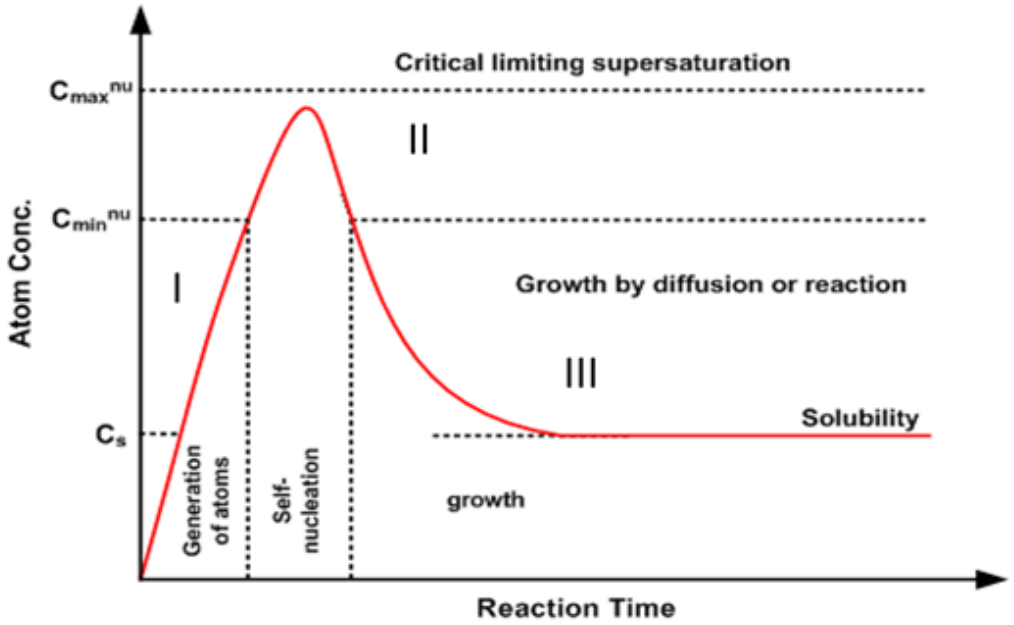

Figure 3. Different stages (I, II and III) of La Mer and Dinegar model of nucleation and crystal growth for monodispersed sols prepared through a dilution method [52] .

The model of La Mer and Dinegar can be summarized as follows:

In stage I, the concentration of atoms progressively increases with time as the precursors decompose by heating or reduction. The new atoms formed are called monomers.

In stage II, monomers tend to self-aggregate into nuclei: this is the self-nucleation. During this step, the concentration of "single" atoms still increases. Once the supersaturation level is reached, single atoms keep adding to the pre-formed nuclei. Consequently, the concentration of monomers starts to decrease, lowering the concentration below the supersaturation level after which no more nucleation occurs. The nucleation event is a pure thermodynamic process according to the theory developed by Becker and Doring [54] which predicts that a thermodynamic system tends to minimise its Gibbs free energy and thus, maximises the entropy of the whole system. This theory, originally used to describe phenomenon such as the condensation of liquid in vapor phase, was extended to other types of phase transitions including the growth process of NPs described by La Mer.

Finally, the decomposition of precursors takes place in stage III. No more nuclei are formed during this stage. Thus, the atoms produced are adsorbed onto the nuclei that will grow into nanocrystals (NCs). This step sees an increase in the average size of NPs until an equilibrium step is reached between the atoms on the surface of the nanocrystals and the atoms in the solution [55]. The surface energy of the newly nucleated NCs will have enough energy to induce an Ostwald ripening where smaller NPs will be "swallowed" by bigger ones, therefore increasing the particle size. Both concentration of

monomers and the degree of supersaturation determine the rate of nucleation. The mechanism of crystal growth will be detailed later in the following section.

It must be noted that the nucleation process mentioned above describes an "ideal" nucleation called homogeneous nucleation. A heterogeneous nucleation occurs when the newly formed atoms are adsorbed directly onto the surface of preformed seeds. When both nucleation types occur, the product will be characterised by polydispersity in terms of size and internal defects within its structure. Other parameters including the precursor reactivity (which depends on the oxidation state of the precursor, the counterion, etc.) affect the kinetics in which monomers are formed and therefore their concentration: a high monomer concentration leads to quicker nucleation events and therefore larger quantities of small nuclei whereas a low monomer concentration leads to a slower nucleation event with larger nuclei in reduced quantities. A fast nucleation event is always preferred because the size distribution of the NCs is better controlled [56]. A high monomer concentration leads to fast growth conditions producing either anisotropic shapes or monodisperse NCs. However, a fast nucleation event means that less free atoms are available for the crystal growth which reduces the aspect ratio of the wire. Therefore, a balance needs to be found in order to obtain high aspect ratio NW with a size distribution as narrow as possible.

Many parameters influence the shape and the final size of the NW among which the concentration of surfactants, the type of surfactant, the temperature

of reaction and the surfactant/precursor ratio [26,57,58]. These parameters have a strong influence on the reactivity of the monomer. The shape of the nuclei depends as well on the chemical potentials of the different crystallographic faces that depend on the chemical environment. The addition of capping ligands and surfactant agents participates to the shape control by restricting the particle growth [59].

2.2.1.3 *The crystal growth*

The crystal growth is the step that follows the nucleation event. It consists in the progressive addition of atoms or group of atoms on the already formed nuclei. The crystal growth can be described via different growth processes such as diffusion limited growth, aggregation or Ostwald ripening. The use of rate equations can predict the size evolution of NPs by considering the rate of certain changes such as the monomer attachment.

In crystal growth, two phases are present: the mother phase and the crystal phase. A system is at equilibrium when its Gibbs free energy G is at minimum. When a material, N is added to a system, a small change in G occurs and is described by the chemical potential, μ [55]. The relation between G and μ is given by:

$$\mu = \left(\frac{\partial G}{\partial N}\right)_{T,p} \quad (6)$$

Where T, the temperature and p, the pressure, are kept constant.

The difference in chemical potential between the mother phase m, and the crystal phase c, determines whether a crystal grows, dissipates or is in equilibrium with the mother phase. The difference, $\Delta\mu_{mc}$ called supersaturation, is the driving force of the crystal growth. The supersaturated solution is not stable in energy:

$$\Delta\mu_{mc} = \mu_m - \mu_C \quad (7)$$

Where μ_m and μ_c correspond to the chemical potential of the mother phase and the crystal phase respectively. If $\Delta\mu_{mC}$ is positive, there is a driving force that enables an addition of material in the crystal phase, i.e. the crystal growth is thermodynamically favourable: if the material (atoms or group of atoms) is continuously supplied to the mother phase, the crystal growth keeps on incorporating the new material in the crystal. On the other hand, if no more material is added, the supersaturation would decrease and reach an equilibrium i.e. $\Delta\mu_{mc} = 0$.

Even though the role of thermodynamics in the crystal growth is crucial, kinetics also plays a role by determining the final quality and structure of deposited material. Thus, kinetic controls the rate of the crystal growth and rules for instance the diffusion of the atom or cluster on a crystal surface.

In order to achieve high aspect ratio NW, a total control of the synthesis parameters is necessary in order to optimise both nucleation and crystal

growth events. Therefore, researchers have developed different techniques to synthesise NW which will be covered in the next section.

2.2.2 NW synthesis using soft technique processes

2.2.2.1 *Introduction*

The soft template techniques are arguably the easiest method in order to obtain NW because they require cheap manufacturing methods. Suitable precursors need to be selected to obtain the right shape of NW. This technique requires the assistance of either surfactants, ligands or catalyst which will be reviewed in the next sections.

2.2.2.2 *Surfactant-assisted soft-template NW synthesis*

2.2.2.2.1 Surfactant: Definition

A surfactant is an amphiphilic molecule containing both a polar hydrophilic part, the “head” and a hydrophobic carbon chain, the “tail” that is insoluble in water. Surfactants possess the ability to self-assemble into thermodynamically stable aggregates. If the surfactant is added to water, the hydrophobic tail of the surfactant tends to gather in order to minimize contact with water. The size and shape of this aggregate is controlled by many factors such as the length of the tail and the area occupied by the hydrophilic head group. The aggregation of surfactants is called micelles: various morphologies can be formed such as spherical, cylindrical or lamellae which consists on a flat

bilayer of surfactants [47]. An illustration of the different shapes that can be adopted by surfactants is given in Figure 4.

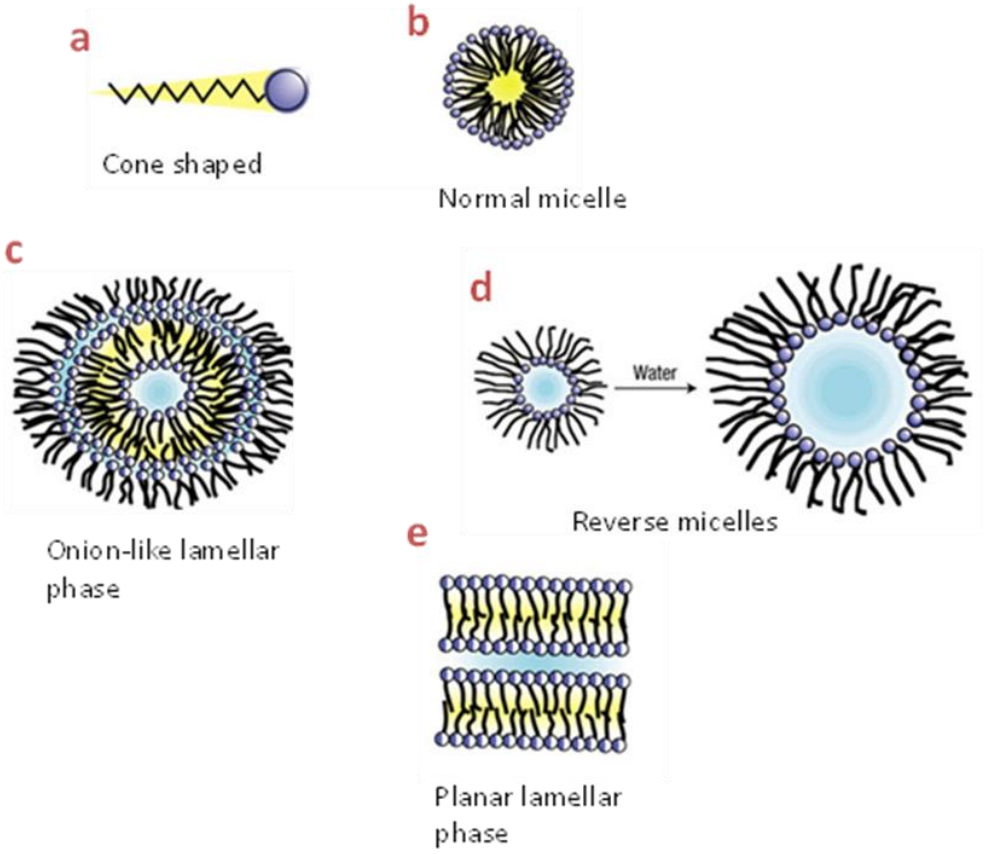

Figure 4. a) One shape of a surfactant and b-e) examples of self-assembled shapes of surfactants in colloidal solutions [47].

The design of NCs is very much linked to the shape of the surfactant, the concentration and the nature of the polar head. The flexibility in the control of the shape of assembled surfactant is an advantage for the fabrication of NPs with anisotropic morphologies [60]. Thus, surfactants are a key component for both NW and nanotubes synthesis.

2.2.2.2.2 Surfactant templated metal NW synthesis

In a surfactant templated synthesis, NPs are typically grown inside the micelles formed by the surfactants. By controlling the concentration of surfactant and the ratio between oil, surfactant and precursor, the architecture of the final product can be tuned [47] and different nanostructures can be obtained as shown in Figure 5. This technique is therefore largely dependent on the shape of the template that is formed.

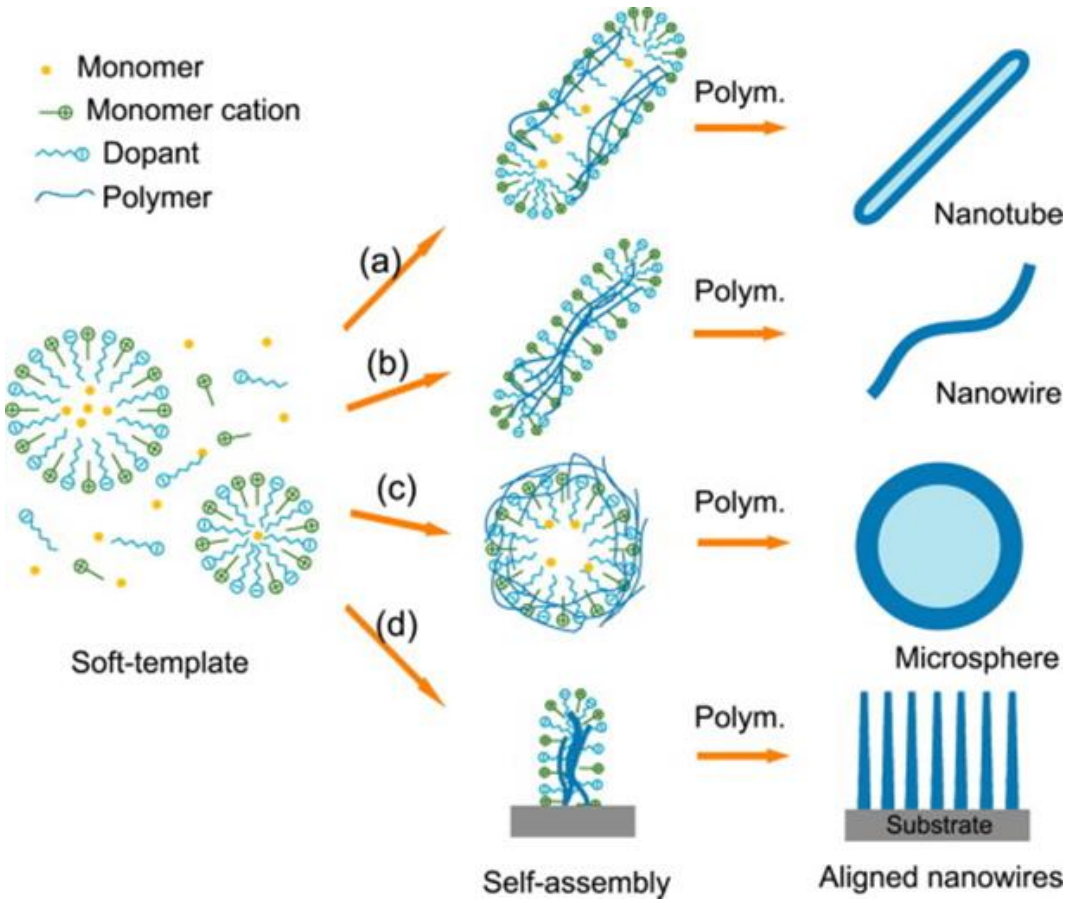

Figure 5. Schematic of the mechanism of formation of different shapes of nanostructures (a-d) through a soft-template synthesis [61].

Long chain cationic surfactants such as Cetrimonium bromide (CTAB) [62,63] and Sodium Dodecyl Sulfate (SDS)[64,65] are for instance very commonly used as

surfactants for the NW synthesis. Non-ionic surfactants like Oleylamine (OLA) and alkyl DNA [66,67] are also largely used because of their robustness and their ability to react with metallic precursors. Metal NW such as platinum NW (PtNW) have been synthesised using this technique: Song and co-workers [62] synthesised PtNW in a micellar solution made of CTAB and sodium borohydride ($NaBH_4$) as a reducing agent. The NW have a diameter of 2.2 nm and length scales of several microns. Other metallic NW such as AgNW [31,65] and CuNW [48,68,69] have often been synthesised using a soft template method. This technique is often considered as the most efficient for controlling NW aspect ratio. However, the synthesis often requires long hours and the cleaning process requires extra steps for the surfactant removal. The solution process uses shorter ligand chains and will be investigated in the next section.

2.2.2.2.3 Solution process methods

One other popular method for synthesising NW is the solution process method which doesn't require any template. The main technique to obtain anisotropic particles is based on the control of the crystal growth. This is controlled by creating an anisotropy in the structure which is enabled by the adsorption of a surfactant [27,30] or a capping agent [70] onto a specific face of the nanostructure. The passivation of one face of the crystal induces a symmetry breaking in the crystal, leaving a face active for the addition of atoms. The addition of a surfactant such as polyvinylpyrrolidone (PVP) has a double positive effect as it promotes the crystal growth and prevents aggregation [26]. However, this technique is mainly used in aqueous solution and is not as widespread as the

surfactant assisted NW method because it suffers from a poor control on the NW aspect ratio.

In conclusion, two techniques have been developed to synthesise NW. The next section will compare the validity of both techniques for the synthesis of CuNW.

2.2.3 Strategy methods to synthesise CuNW

2.2.3.1 *Interest in Copper and CuNW*

Copper is a well-known element since the Antiquity. It even gave its name for a period of the bronze age: the chalcolithic (from the Greek khalkos: copper and lithos: stone) or the "copper age" [71]. During this period, humans discovered the use of copper and how to alloy it with tin to from bronze [72]. Copper possesses remarkable properties: malleable and flexible in pure form, it becomes stronger and more ductile in its oxidized form. It possesses the property to alloy with several metals including zinc and nickel. Copper presents also the advantage to be cheaper compared to silver or gold.

In the nanoscale, CuNW have shown an increased interest after Zeng's group has published a rapid synthesis method to obtain ultralong CuNW [73]. This has been followed up by many other works and an aspect ratio above 1000 has been reached for CuNW [6]. Currently CuNW TC have shown similar optoelectronic properties than the one based on AgNW. The next section will present the different synthesis method developed to synthesise CuNW.

2.2.3.2 *Synthesis methods of CuNW.*

This section will compare CuNW synthesised using the main methods previously enunciated in section 2.2.2.

2.2.3.2.1 CuNW solution process route

The solution process synthesis of CuNW has been firstly reported in 2005 by Zeng's team [70]. The synthesis presented the advantage of being very quick (60 min long) and involved the reduction of Cu^{2+} salts with the help of a strong reducing agent. It did not require the presence of an inert gas and the anisotropic growth was promoted by reducing the supersaturation level of the solution using ethylenediamine (EDA) as a capping agent to bind Cu^{2+} ions. When EDA was not present, only NPs were visible confirming its crucial role in the promotion of the anisotropic growth of CuNW. The redox reaction occurred in a strong alkaline media to provide a suitable environment for the reaction: the higher the pH was, the higher the redox potential of hydrazine. Solution passed progressively from a deep blue to a red colour as shown in Figure 6. At the end of the reaction, all Cu^{2+} ions have reacted to form pure Cu in the form of NW and NPs. Even though the synthesis exhibited a high aspect ratio (above 200) producing long (about 20 μm) and relatively thin (90 nm) CuNW, it still suffered from polydispersity in the length, unwanted NPs and non-reversible aggregation which reduced the yield of the synthesis.

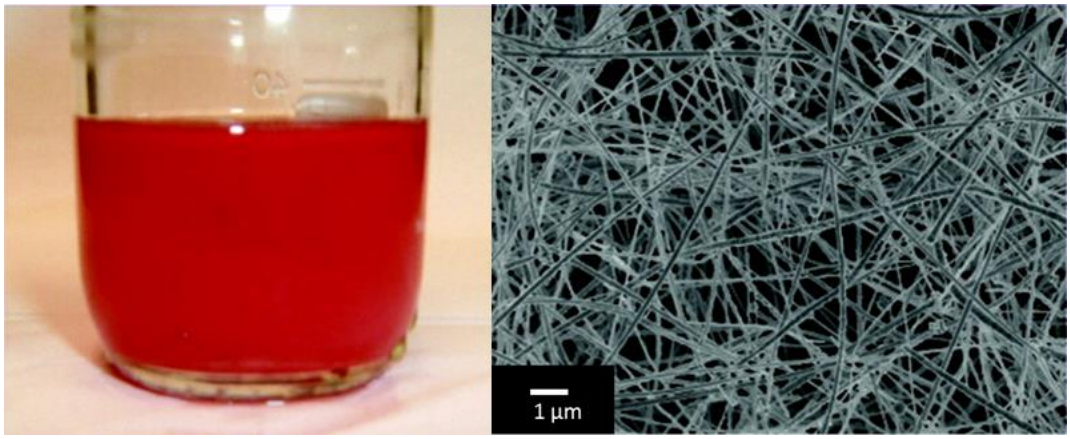

Figure 6. a) CuNW dispersed in water b) SEM micrograph of the as-synthesised NW [70].

Rathmell *et al.* [27] slightly modified the synthesis introducing a two-step process: the reaction temperature was increased up to 80 °C which shortened the reaction to 3 min only. These steps allowed the reduction of Cu precursors into Cu atoms forming nuclei while the crystal growth was promoted by adding PVP to the mixture and pouring the solution in an ice-bath for an hour. PVP helped to prevent the aggregation of NW as the well dispersed NW would be lifted to the top of the vial. This "two-step" formation of NW presented the advantage of producing well dispersed NW. However, a non-negligible amount of NW was removed from the final product. Meng and Jing [59] modified the concentration of the synthesis developed by Zeng and coworkers [70] using a Continuous Flow Reactor (CFR) to ensure that the precursors continuously flowed through the reactor at 60°C for 4h which resulted in an increase of the NW length, passing from 30 µm to 50 µm with an unchanged diameter of 200 nm. A schematic of the equipment is shown in Figure 7.

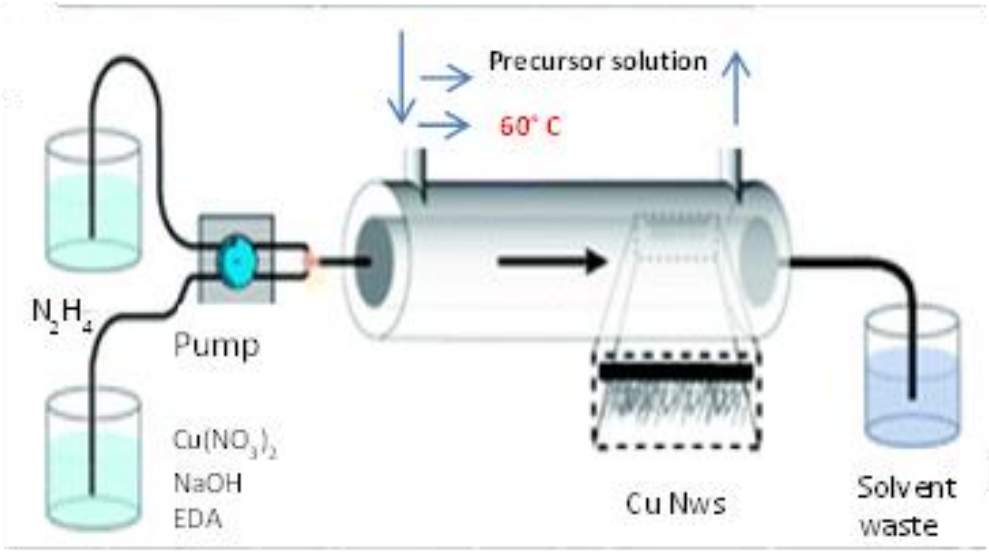

Figure 7. Schematic CFR used for the CuNW growth [74].

Therefore, CuNW formed with a solution process route are mostly synthesised using the method firstly developed by Zeng's group. It is a very easy method to obtain ultralong CuNW. However, the diameter remains very high for current NW standards which is due to the adsorption of moieties by the highly hygroscopic EDA. Long alkyl chains are known to provide a better control of the NC size by forming different templates according to their concentration. The next section will give an overview of different CuNW syntheses using long chain surfactants.

2.2.3.2.2 CuNW synthesis via a soft-template route

Several methods that are involving a soft-template route have been reported for the synthesis of long and uniform CuNW. Filankembo *et al.* [75] described a new method to produce CuNW in a micelle template system ($(AOT)_2$ – isooctane-water system). The shape of the NC was tuned by adding different salts while the template remained the same. A hydrothermal reaction in an

autoclave involving the glucose reduction of $CuCl_2$ in presence of Hexadecylamine (HDA) have been performed by Mohl *et al.* [76] in order to obtain high aspect ratio NW with a length of few micrometres and a diameter of 64 nm. Bicer *et al.* [77] prepared ultra-long NW using both CTAB and ascorbic acid as reducing agents. Yu *et al.* [78] proposed a single surfactant-assisted synthesis to obtain CuNW with a high aspect ratio using octadecylamine (ODA) as a ligand, surfactant and capping agent. The reaction took place in an autoclave, heated up to 180°C for 48h. The amine group of ODA reduced the copper salt: ODA molecules coordinated with Cu ions to transfer them from the aqueous phase to the interfacial one. When the temperature increased, the NW were formed in the interlayers of the ODA lamellar structure. The synthesis produced uniform NW and some bundles together. This work showed also that parameters such as temperature or the surfactant concentration were critical to the NW crystal structure and diameter size.

A subcategory of surfactant-assisted synthesis has emerged in the last decade. It involved the use of a metal precursor catalyst which initiated the reduction of CuNW via galvanic replacement. Following this method, Zhang *et al.* [43] obtained well dispersed CuNW through a self-catalytic growth of NPs in presence of Pt. Copper acetylacetonate $Cu(acac)_2$ was used as a precursor to promote the formation of NPs exhibiting a hexagonal cross-section. CTAB and HDA were used as surfactants to form an oily phase while their polar counter phase (amine group of HDA and bromide ions, Br^-) reacted with the copper precursor. The mechanism of formation of CuNW is described in Figure 8 below. The presence of Br^- ions has been shown to be necessary in promoting the NW anisotropic growth.

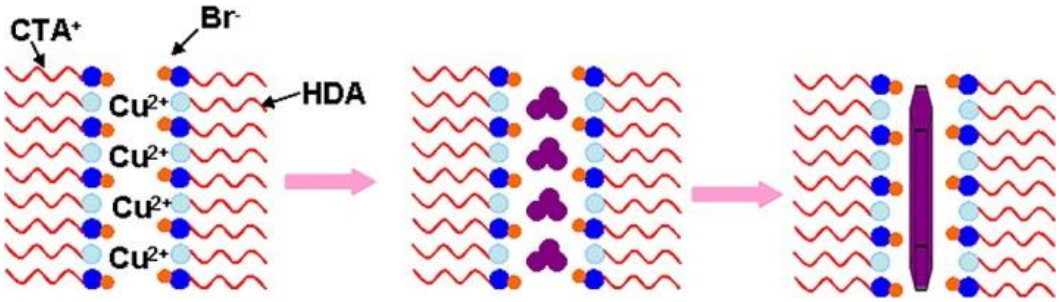

Figure 8. Mechanism of formation of CuNW showing i) the formation of a lamellar phase made of HDA and CTAB within which ii) Cu precursors are reduced into Cu clusters that iii) further grow into NW [43].

Similarly, Guo *et al.* [6] have synthesised ultralong CuNW using nickel acetylacetonate ($Ni(acac)_2$) as a catalyst. Copper chloride ($CuCl_2$) were reduced by OLA. The reaction was kept for 10h in a flow of argon at a temperature of 175°C. The NW produced, grew along the [110] direction and exhibited a penta-twinned pentagonal structure. Up to 40 µm long NW were reached while the diameter was ten times thinner than the previous CuNW reported. Although these NW possessed a better aspect ratio, the uniformity in length was not yet reached.

Soft-template processes allow the production of high aspect ratio CuNW but they present some disadvantages such as a long processing time and the use of an inert gas. However, the choice of a long chain surfactant allows this synthesis to be more stable than in an aqueous system. The surfactant assisted synthesis of CuNW is also the most adapted in fabricating ultralong NW [79] which makes this technique the most suitable for large-scale CuNW synthesis. The next part will explore the different methods to fabricate CuNW TC and their integration in devices.

2.3 Investigation on the fabrication of CuNW based TC.

2.3.1 The different technologies to fabricate TC.

NW TC fabrication can involve several steps among which treatments on the NW dispersion, NW thin film preparations, pre- and post- treatments of the NW films. The different steps will be presented in this section focusing mainly on CuNW TC fabrication.

2.3.1.1 *Thin film fabrication*

Many techniques can be used to deposit metallic NW on diverse substrates. Dip coating [80-83], Meyer road [27,84-86], spin coating, Langmuir Blodgett [87-90], roll to roll printing [73] are the most popular techniques to fabricate NW TC . Caution needs to be taken with CuNW because they suffer from corrosion due to the oxidation of Cu [86] and require therefore to be dispersed in a suitable ink to prevent their degradation [27]. Wu *et al.* [25] reported the fabrication of high performance CuNW TC using electrospun fibers as a mask. The nanofiber networks provided percolating paths that resulted in the formation of connections between the wires leading to a conductive composite/metal network. These CuNW-based TC offered higher performances than the one exhibited by ITO, Carbon nanotubes- and graphene-based electrodes. These low-cost methods have great potential to be scaled up and hence good candidates for industrialisation.

Several flexible devices have been fabricated using a Meyer rod: Hu *et al.* [84] deposited AgNW dispersed in methanol on a flexible polyethylene

terephthalate (PET) surface. Films exhibited a transmittance of 80% and a R_s between 8 to 20 Ω/□, which is comparable to ITO's optoelectronic performances on plastic substrate [91]. Yu *et al.* [92] obtained a transmittance of 75 % and a R_s of 175 Ω/□ by depositing AgNW, dispersed in isopropyl alcohol, on PET substrate. An HCl vapour treatment and a nail polish on top of the thin film helped to prevent the NW oxidation. These methods can be easily applied to CuNW. In a similar way, Rathmell *et al.* [27] deposited CuNW coated with nitrocellulose on PET substrates. Nitrocellulose increased the viscosity of the solution allowing the deposition of NW on the substrate. Films were annealed at 170°C to remove the polymer leaving a smooth network of NW. Films exhibited promising results: a R_s of 30 Ω/□ for a transmittance of 85% were reported, which is similar to the values obtained with AgNW films TC. An illustration of the thin film is shown in Figure 9.

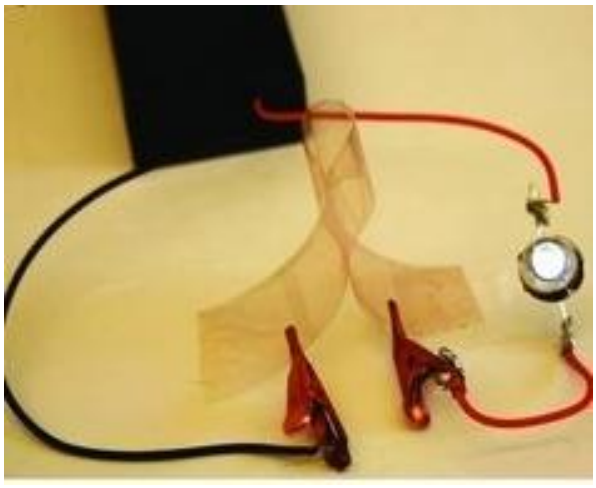

Figure 9 Picture of a conductive CuNW thin film TC deposited on a PET substrate [27].

Guo *et al.* [6] produced CuNW TC thin films achieving a R_s of 52 Ω/□ and a transmittance of 93%. CuNW were deposited onto flexible polymers using a

vacuum filtration method developed by De *et al.* [16] which is illustrated in Figure 10.

Following the same device fabrication method, Zhang *et al.* [43] produced thin film devices exhibiting a transmittance of 90% and a sheet resistance of 90 Ω/□.

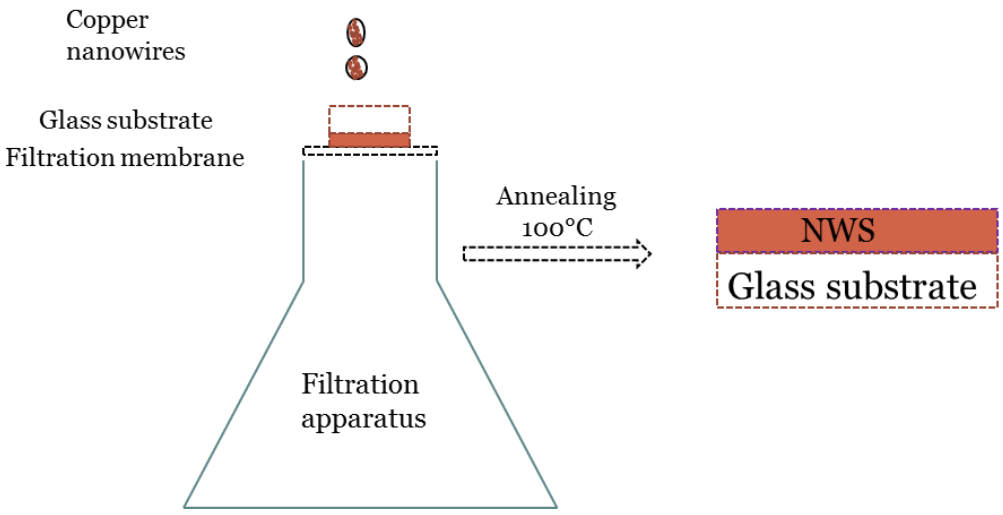

Figure 10. Schematic illustration of the vacuum filtration method for CuNW dispersions and their transfer onto either glass substrate or plastic substrates [16,93].

Therefore, different techniques exist to fabricate highly efficient NW TC. Greater optoelectronic performances can be obtained by identifying and improving the key parameters they are dependent on. The next section will review these parameters.

2.3.1.2 *Parameters that influence the thin film quality.*

NW require some ligands on their surface to be dispersible in solvents. However, the presence of an organic layer lowers the conductivity of TC or makes the NW network completely insulating. The longer the organic layer

chain, the more likely the resistivity of the film to be high. In many examples, thermal annealing [24,94] and optothermal heating [95] have improved the efficiency of NW based TC.

The roughness of the film is a parameter that needs to be taken into account. For application such as photovoltaic devices, the roughness is an important factor that can lead to short-circuits and leakage. Many ways to control the roughness of the film have been explored such as the addition of polymer coating [94], thermal annealing [96] and mechanical pressing [86]. Controlling both diameter and density of NW within the substrate can help to solve the issue.

The adhesion of the thin film onto the substrate is also another important parameter that can be critical for HER applications for instance. The adhesion of NW depends on many factors such as the affinity between the wire and the substrate [97]. Ways to improve the film adhesion include plasma treatment of the substrate [98] and embedding the NW in a matrix [99]. However, caution needs to be taken to ensure that the film is still conductive after any additional step.

In conclusion, CuNW TC have a great potential as substitutes to ITO due to their excellent optoelectronic performances. However, CuNW films degrade very quickly because of the oxidation of Cu. Many methods exist to passivate CuNW films from their oxidation and will be explored in the following paragraph.

2.3.2 Protection of CuNW TC against oxidation: addition of a coating

In order to avoid the oxidation of NW films, researchers have investigated the addition of a coating on top of the films. A good coating should protect the film while keeping its optoelectronic properties unchanged. For instance, Im *et al.* [100] have reported the fabrication of CuNW on glass-fabric reinforced plastic (GFRHybrimer) via vacuum transfer printing. The NW are then annealed, and subsequently UV cured in order to embed them in the GFRHybrimer. The transmission of the films after encapsulation in the plastic matrix remained unchanged and the resulting films possessed a R_s of 25 Ω/□ for a transmission of 82%. Films with a R_s= 18 Ω/□ showed no significant changes in the electronical properties after 14 days left at 80°C in air.

Recently, researchers have focused their attention on combining CuNW with reduced Graphene Oxide (rGO) in order to prevent the oxidation of the films. Zhu *et al.* [101] spun coat on top of a CuNW film a layer of ZnO, synthesised via a sol-gel method, and a reduced Graphene Oxide (rGO) layer as an overcoat. The optoelectronic properties of the film remained quite good: the transmission of the films dropped from 88% to 79% with the addition of both layers. However, the resistance of the film was improved. A scotch tape peel test showed that ZnO enhanced the adhesion of NW films on the surface while the rGO layer helped to passivate the film in harsh conditions: after 4 days kept at 85°C and 85% humidity, the R_s of CuNW/ZnO/rGO composites increased slightly while the R_s of CuNW/ ZnO films increased up to 20 times under the same conditions. Dou *et al.* [102] have synthesised a single step core-shell Cu/rGO NW with a diameter below 30 nm. The resulting films exhibited optoelectronic

performances similar to AgNW ones: R_s = 28 Ω/□, T= 90% and a haze factor of 4% as shown in Figure 11. The films showed an increase of only 2 Ω/□ when annealed at 80°C, over the 50-hours study and the films were air stable in a period of 200 days.

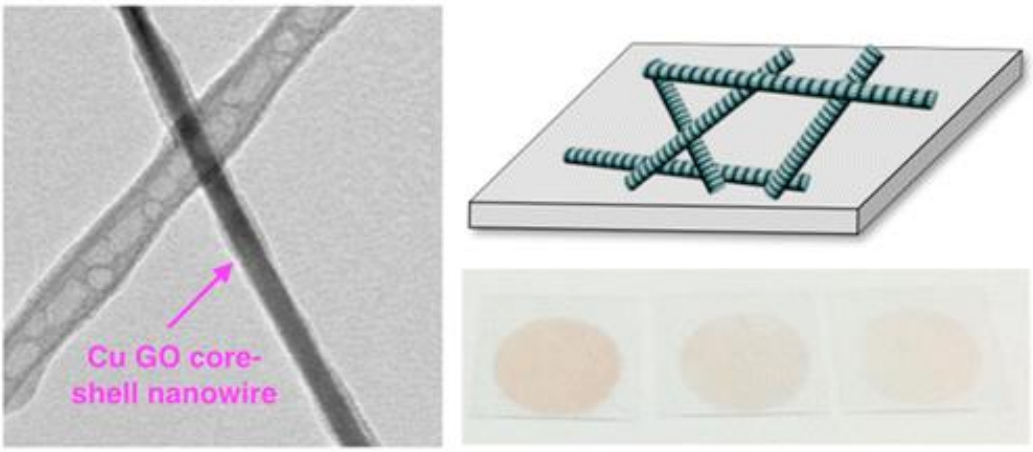

Figure 11. Left: TEM picture of CuNW coated with rGO. Upper right: schematic illustration of core-shell CuNW/rGO TC and bottom right: picture of the different TC films with different thicknesses [102].

Zhang *et al.* [103] have synthesised hybrid materials composed of CuNW and rGO nanosheets bridging between NW. The resulting films deposited on a polystyrene cloth which was prepared using a vacuum filtration method, exhibited a high conductivity (0.8 Ω/□). The rGO helped the passivation of CuNW: the conductivity of the film increased only to 3.8 Ω/□ with the addition of the nanosheets. Hsu *et al.* [104] used atomic layer deposition (ALD) to coat NW with both Aluminium doped Zinc oxide (AZO) and Aluminium oxide (Al_2O_3) passivation layers. They showed that AZO and Al_2O_3 had a synergetic effect where AZO improved the reliability of the network while Al_2O_3

increased its resistance to oxidation. The transmittance of the film remained excellent with only 1% transmittance decrease with the addition of the coating.

This section has shown that the addition of a suitable coating is an efficient method to prevent NW films oxidation. Recently, another interesting way to passivate NPs in general has emerged. The procedure consists in combining different metals in order to form either core-shell or alloyed NPs [58,105-107] and will be the focus of the next part.

2.4 Fabrication of bimetallic NW hybrids: core-shell, alloys and their applications

2.4.1 Introduction

Several research groups have directed a great deal of attention towards the synthesis of bimetallic NPs [108-110], which have shown different properties from their monometallic counterpart. Advantages of associating different metals to form NPs are multiple: more mechanical and chemical stability [86] and an increase in the NPs catalytic properties [105,111].

A great amount of efforts has been placed on developing syntheses methods capable of tailoring bimetallic NCs with specific atomic-scale features. Currently, many methods developed by diverse research groups have contributed to the synthesis of a wide-spectrum of bimetallic NCs: linked monometallic NPs [112], core-shell [105,113,114], alloys [115-117] and hollow [118-120] are among the structures possible. A representation of the different atomic organisations adopted by Platinum-Ruthenium (PtRu) NPs is shown in Figure 12. As for monometallic NPs, they can be synthesised either by chemical (soft-template synthesis [121], solution process [86,122]) or physical (atomic layer deposition [123], electrodeposition [124]) routes. Although comprised of only two elements, it is not quite easy to define bimetallic NPs as they can differ in many ways such as atomic ordering (alloys, intermetallics, core-shell…), crystal structure, internal structure (presence of twin defects or stacking faults) or a combination of these factors. In order to simplify this review, I will distinguish bimetallic NPs according to the spatial distribution of their atoms. Since this

field of study is very new, the review will be extended to metallic NPs in general.

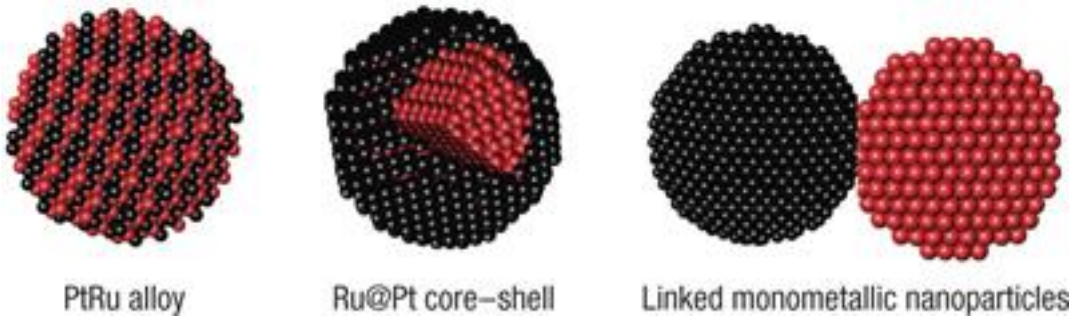

Figure 12 Representation of the different atomic organisations of Pt and Ru for an alloy, a core-shell and linked monometallic NPs structures [112].

2.4.2 Fundamental differences between core-shell and alloys

In this review two type of bimetallic atomic ordering will be investigated: alloys and core-shell structures. A bimetallic NC is considered to be an alloy when two metals are randomly distributed within the NC while core-shell structures imply that there is a well-defined boundary between both elements [125]. Alloys and core-shell structures tend to have different physical properties even though they have the same chemical composition. The synthesis of both alloy and core-shell NCs require different syntheses methods: thermodynamic consideration such as atomic interaction and surface energy will decide on the final configuration of the atoms within the crystals but kinetic (nucleation, growth rate…) needs also to be taken into account [126-128].

The formation of either alloys or core-shell NCs are based in some fundamental differences. In order to obtain an alloy, the mixing of two metals M and N will be favoured if the M-N bond is stronger than M-M and N-N bonds,

the two metal have similar lattices parameters and the metal have similar surface energy [129,130]. However, these parameters are only considered in thermodynamically stable environment: if the kinetic of the reaction is not met, for instance the temperature of the reaction is too low [89], the atoms are hindered from bulk diffusion and they might form a core-shell structure instead. Increasing the temperature of the synthesis is often required to promote the decomposition of the precursors and their interdiffusion. Choosing highly miscible metals M and N is a preferable requirement to form alloys. The thermodynamic can predict the formation of an alloy or an intermetallic NC by taking into account the Gibbs free energy of the mixture ΔG_{mix} that is defined by [127]:

$$\Delta G_{mix} = \Delta H_{mix} - T\Delta S_{mix} \quad (8)$$

Where ΔH_{mix} and ΔS_{mix} are the changes in enthalpy and entropy and T the absolute temperature.

Some bimetallic structures will naturally favour the fabrication of core-shell structures. They are often regarded to be easier to form than alloys, because they require less care during the synthesis. Currently, the synthesis of core-shell structures with ultrathin shells have garnered a great deal of attention because they enhance the properties of NCs while increasing their anisotropy in case of NW. When the shell metal has a high cost, ultrathin shell structures help to reduce the cost of the synthesis. Another advantage is that the ultrathin

shell enhances catalytic activity. For shell thickness superior to 6 atomic layers, it is often accepted that the properties (optical, magnetic) are dominated by the shell. In case of NW structures, the increase of shell thickness also reduces the anisotropy of the NW [86]. However, there are advantages in having a thick shell as it can tune the optical property of the NC by shifting the Surface Plasmon Resonance (SPR) [131] and in some cases it enhances the chemical and/or thermal stability. Different synthetic approaches are used to synthesise bimetallic NCs and will be reviewed in the next section.

2.4.3 Synthesis methods to produce core-shell and alloys

2.4.3.1 *Synthesis of alloys*

The co-reduction involves the simultaneous reduction of two metallic precursors M and N into zero valent M^0 and N^0 metals that will nucleate together and grow to form MN NCs. The co-reduction involves an extremely important parameter which is the standard reduction potential of the precursors [132]. It is often required that the reduction potential of two species M and N need to be close enough to form an alloy. This reduction potential depends on the nature of the coordinating ligand, the capping agent and the reaction temperature.

The kinetic of the reaction is also an important parameter as it defines the rate in which the metal precursor will be reduced to generate metal atoms. It implies the rate at which an electron is transferred from the reducing agent to

the metal precursor which is defined by the Marcus theory [133] and is related to the distance between the electron donor and acceptor. The expression of the rate constant for the electron transfer is expressed by:

$$k = A.e^{-\Delta G/k_B T} \quad (9)$$

Where A is a factor dependent on the distance between the molecule that donates the electron and the one that accepts it, ΔG is the free Gibbs energy, k_B is the Boltzmann constant and T the absolute temperature.

Therefore, the kinetic of an electron transfer and the thermodynamic stability of reactants, products and other interacting species are linked.

The reduction potential of the species is an important parameter for bimetallic NCs [58]: species with higher standard reduction potential (more noble) will reduce first than species with lower standard reduction potential. Therefore, in case of a co-reduction method, metal species with quasi similar standard reduction potential are privileged. In some cases, the co-reduction of metal species can be achieved by increasing the concentration of one metal precursor that can compensate a slower reduction. For instance, Wang *et al.* [58] have been able to synthesise AuAg alloys by increasing the content of $AgNO_3^-$ over $HAuCl_4^-$ despite the fact that Au^{3+}/Au and Ag^+/Ag have reduction potential of 1.5 V and -0.8 V respectively. The role of chloride ions has been evidenced as the driving force for the alloy formation. Kim *et al.* [134] have used the same technique in order to simultaneously reduce $Au(acac)_3$ and $Cu(acac)_2$ to produce Au, Au_3Cu, $AuCu_3$, AuCu and Cu nanosphere alloys by varying the

concentration of the precursors. The effects of the chemical composition on the optical and structural properties of the NC are shown in Figure 13. This method works also for species that have very similar reduction potential: Liu *et al.* [135] have shown that Pd-Pt alloyed NCs can be prepared in OLA using $Pd(acac)_2$ and $Pt(acac)_2$ as precursors.

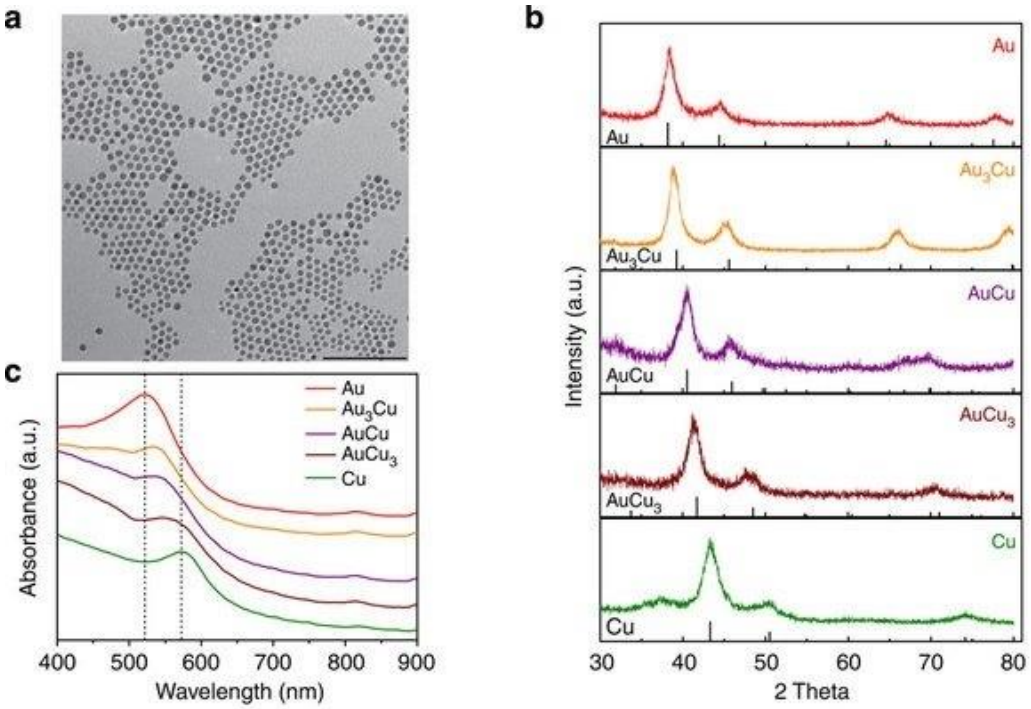

Figure 13. a) TEM image of $AuCu_3$ NPs, the scale bar is at 100 nm, b) XRD patterns of Au–Cu bimetallic NPs compared with XRD patterns of Cu and Au and c) Ultraviolet–visible spectra of Au–Cu bimetallic NPs compared with the SPR peak of pure Au (~523 nm) and Cu (~570 nm) NPs shown by the dotted lines [134].

Very few alloyed NW have been reported, mainly for PtNW and ultrathin AuNW [136,137]. Peng *et al.* [138] have synthesised worm-like dependent composition growth PtAg NW. Similarly, 1:1 AgAu NW alloys have been reported by Krichevski *et al.* [137] which are obtained by increasing the Ag^+

concentration up to 2:1 Ag:Au initial molar ratio, lowering the pH to 5, and increasing both surfactant and reducing agent concentrations.

2.4.3.2 *Synthesis of core-shell NCs*

Regarding core-shell structures, several reports have shown the successful synthesis of bimetallic NCs. The formation of a core-shell follows usually the seed-mediated growth explained in the section 2.2.3.2.2. Habas *et al.* [139] have for instance demonstrated that the formation of PdPt core-shell NCs was due to the addition of Pd atoms on Pt nanocubes. Gao *et al.* [140] have synthesised AuAg core-shell nanoplates using the same method. The Au shell helped the chemically reactive Ag to resist against harsh environments such as low and high pH solutions, enhancing the chemical stability of the nanoplates. The core-shell fabrication follows a sequential reduction of the different precursors where the M precursor which reduces first (the more noble material) will act as a heterogeneous site for N precursors. Li *et al.*[141] for instance, have shown that Au decahedral seeds formed first and served as base for the nucleation of Ag in the AgAu nanorod synthesis. This technique is very popular for the synthesis of core-shell NW. Regarding CuNW, many research groups have focused their attention in synthesising CuNi core-shell structures. Although Cu and Ni are highly miscible, Cu^{2+} and Ni^{2+} species have a reduction potential of 0.34 V and -0.25 V respectively, rendering difficult the synthesis of alloys in normal conditions. The team of Zheng [122] was the first one to report a one-pot synthesis of CuNW coated with Ni. Similarly to their previous synthesis on CuNW [43], the reaction took place in a chemical bath and was

heated up to 80°C. Ni and Cu precursors were added into the alkaline solution of NaOH, Ethylenediamine (EDA) was used as a capping agent and hydrazine was added as a strong reducing agent. This synthesis of cupronickel NW relies therefore on the difference of potential between the couple Cu^{2+}/Cu and Ni^{2+}/Ni, resulting in the formation of NW with a Cu core and a Ni shell. The authors attributed the origin of the formation of the Ni shell to the presence of defects on the surface of CuNW, prone to surface oxidation upon exposure to air [86]. This one-pot synthesis produced long NW with an average length of 20 µm and a diameter of 200-300 nm. They have also shown that the addition of a Ni shell changed the properties of these NW by making them magnetic, therefore confirming that the NW properties are now influenced by the shell.

Rathmell *et al.* [27] reported a two-pot synthesis of Cu_{core}/Ni_{shell}. CuNW synthesised following the procedure explained in 2.2.3.2.1, were dispersed in ethylene glycol while PVP, nickel salt and hydrazine were added sequentially. The NW exhibited a 2:1 Cu:Ni molar ratio for an average length of 25 µm and a diameter of 116 nm. As a result of the addition of nickel, cupronickel NW crystalline structure differed from their monometallic counterpart exhibiting a 5-fold twinned crystal structure and a pentagonal cross section. The research group has been successful in fabricating TC based on this material: the resulting core-shell NW films exhibited a sheet resistance of 60 Ω/□ while the transmittance passed from 94% to 85% with the addition of the shell [86]. The decrease in transmittance can be attributed to an increase of the diameter and the increase in R_s to the lower conductivity of Ni over Cu. However, CuNi core-shell films shown in Figure 14 were 1000 times more resistant that CuNW films. In comparison, in an oven at 85°C, the R_s started to increase by an order

of magnitude after 1 day for CuNW films and 13 days for AgNW films while CuNi core-shell films remained stable over a period of a month.

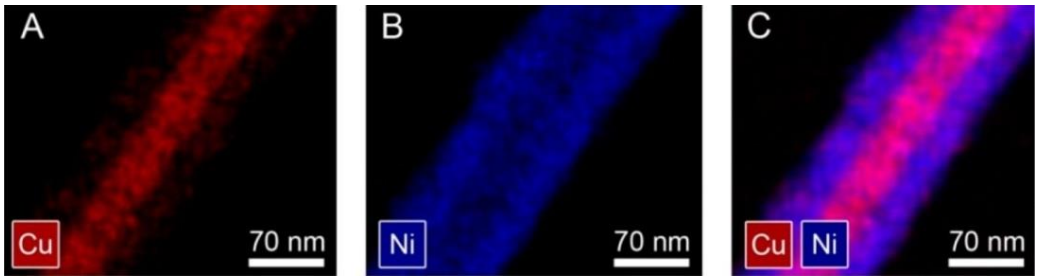

Figure 14. Energy dispersive X-ray spectroscopy images of CuNW coated with nickel [86] .

One advantage of coating CuNW with Ni is that the colour of the film changes from red to grey and therefore these core-shell NW might be more suitable for application such as displays. Other metals have been coated instead of Ni, such as Zn, Sn and In [142] using a two steps solution approach and the optoelectronic properties of the film remained the same with a loss of transmittance of about 7%. In order to improve the transmittance, the authors proposed to expose the thin film to oxidising solutions such as a diluted solution of H_2O_2 for 15 min. This improved the transmittance of the film passing from 75% to 84% while keeping the same value of R_s. The gain in transmittance was probably due to the NW etching that resulted in a decrease in diameter. Song *et al.* [143] have successfully synthesised Cu@Cu-Ni NW elastomer composites in a single phase synthesis using $CuCl_2$ and $Ni(acac)_2$ in presence of OLA. The resulting films exhibited a transparency of 80% with a R_s of 62 Ω/□. These composite films were very stable, and the conductivity remained constant for up to 1200 days. Mehta *et al.* [144] have reported the fabrication of $CuNW_{core}$/ $graphene_{shell}$

films resulting in an improvement of both thermal and electrical conductivity of the films. These results have been attributed to a passivation of CuNW with graphene and a partial elastic surface scattering that increased the electron transport through the wire.

2.4.3.3 *Other parameters influencing the synthesis of bimetallic NCs*

According to Marcus theory, the addition of chemicals that link with the metal precursor can affect the reduction potential and the reduction kinetic [133,145]. Therefore, researchers have focused their attention towards the addition of additives in order to enhance the reduction of metal precursors. Any species added to the reaction might have an effect on the reduction of metal precursors. For instance, ligands have been found to be critical in the formation of metal shaped NPs. Therefore, Dimitrov *et al.* [146] have shown that Pt-Cu nanocubes alloys can be formed with the addition of a dial derivative (1,2-tetradecanediol or TDD) in presence of OLA and other ligands. They demonstrated that TDD was responsible for the co-reduction of Pt^{2+} and Cu^{2+} ions and that the ratio between the metal precursors, the amount of stabilising/coordinating agents as well as reaction temperature could tune the final composition of the nanocubes.

The capping agent is another parameter that can modify the final shape of the NCs. A non-exhaustive list of capping agents such as ions, gases, ligands, surfactant, and polymers [107,147-150] have shown to be effective in the shape control of NPs for monometallic synthesis. In case of bimetallic NCs, the capping ligand that are effective for the monometallic counterpart might not

produce the same results. However, some cases have reported that capping ligands designed the final shape of bimetallic crystals. For instance, Yin *et al.* [151] have found that in presence of CO_4^{2-} ions, Pd-Pt alloyed NCs presented a tetrahedral shape while in the presence of Br^- and low quantities of I^- ions, nanocubes alloys were formed.

2.4.4 Application of bimetallic NCs

The formation of bimetallic NCs is proven to be an excellent tactic to unveil new optical and catalytic properties capable of overcoming issues encountered with their monometallic counterparts. Bimetallic NCs have directed a growing attention for catalytic applications such as Oxygen Reduction Reaction (ORR), Formic Acid Reaction (FAO) and Hydrogen Evolution Reaction (HER). The ability to tune the chemical composition, morphology and even the shape of the edge of bimetallic NCs have proven to enhance the activity of these particles. The next section will present an overview of the different applications of bimetallic NPs and NW.

2.4.4.1 *Pt-based NCs*

Pt is arguably the most promising catalyst, but Pt is also very scarce and therefore very expensive. Many groups have combined Pt with different elements in order to decrease the cost while enhancing its activity. For instance, PtCu NCs have emerged as an alternative catalytic material with enhanced activity as well as CO tolerance improvements PtCu nanocubes of

different compositions have been synthesised by Xu *et al.* [146] and they used cyclic voltammetry to assess the electrochemical activity toward FAO. They have shown that the electrocatalytic activity reached a maximum when the composition of the alloy was 80:20 Pt:Cu and the performance was overpowering the one of pure Pt even after 300 h cycling. After 300 h, they observed an electrochemical activity decrease which was attributed to the degradation of the core-shell NPs in acidic environment. Therefore, the electrochemical reaction of bimetallic NPs is dependent on their composition. Recently, Wang *et al.* [152] have synthesised PtCu NW with an aspect ratio superior to 10000 and exhibited superior methanol and ethanol electrooxidation in alkaline conditions with an anodic peak value of 0.055 $A.cm^{-2}$ for PtCu NW which is higher than pure PtNW (0.045 $A.cm^{-2}$). The shape activity dependency has been pointed out regarding Pt_xNi NCs. Pt_3Ni nanoframes [153], octahedra and icosahedra have been studied in the last years where Pt_3Ni have shown the best performances towards ORR. Doping Pt_3Ni octahedral with Mo was proven to be effective with a specific activity of 10.3 $mA.cm^{-2}$ [154]. Therefore, combining Pt with non-noble metals allows the reduction of the cost while improving the electrocatalytic performances. This strategy is also proven useful for the fabrication of enhanced photocatalysts: by designing Au nanorods decorated with Pt NPs on the tip, Zheng *et al.* [155] have managed to fabricated dual photocatalyst capable of reducing water to H_2 at the Pt tip while methanol was oxidised at the Au nanorods upon irradiation in the visible and near IR light. They attributed this photocatalytic activity to a transfer of the charge carriers from Au nanorods to the Pt tip. The

effect of the addition of Pt on the PL as well as both mechanism of reduction of H_2O and oxidation of methanol are shown in Figure 15.

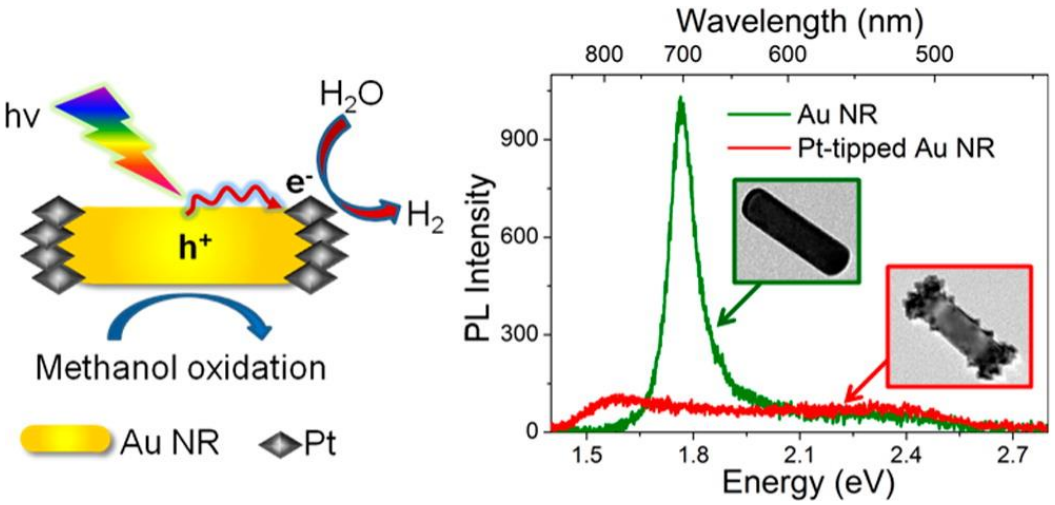

Figure 15. Left, illustration showing the reduction of H_2O to H_2 by Pt NPs at the tip and the oxidation of methanol by the Au nanorod. Right, normalised PL spectra for both Au nanorods and Pt decorated Au Nanorods [155].

By controlling the composition, size, shape of structure of the NCs, the suitable electrocatalyst can be obtained for each application. The next section will cover non-noble bimetallic catalysts and investigate whether the same trend is observed.

2.4.4.2 *Other bimetallic NCs*

Aside from Pt based, other bimetallic materials have been investigated because they present the advantage of being cheaper than Pt and they have proven to enhance electrochemical activities as much as Pt based NCs [156,157]. Combining bimetallic metals outperform the properties of the corresponding pure metal in many examples. For instance, CuAu NCs have enhanced the CO_2 reduction while improving CO oxidation compared to both Cu and Au NPs. The

authors noted a peak of activity for Au_3Cu [134]. Bimetallic NPs of Au/Ag coated in silica have improved a Dye Synthesised Solar Cell (DSSC) performance by 26% [158]. The authors attributed this improvement to an increase of the light absorption with the apparition of a multipolar SPR resulting in a broader capture of the solar light. They have also demonstrated that the addition of an Ag shell around the Au NPs increased the light scattering by ten times than Au NPs on their own.

Wang *et al* .[159] have shown that electrocatalytic activities of CuNi were shape-dependent as shown in Figure 16 where nanocubes displayed higher catalytic activities than octahedral NPs of similar composition. Ni based NCs have shown to be the most promising non-noble alloys for HER applications even though Ni possesses a low electrocatalytic activity. Ni-Mo alloys are the most active catalyst in alkaline solution owing an overpotential of 0.1V at 300 mA/cm^2 [157].

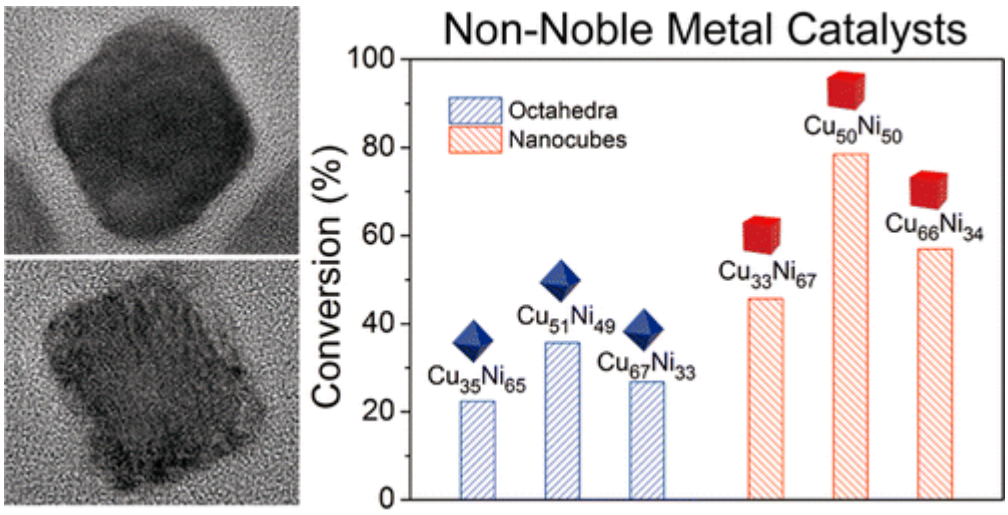

Figure 16. Left: TEM pictures of Ni-Mo octahedral (top) and nanocube (bottom) alloyed NPs, right: classification of the catalytic activity of the Ni-Mo alloys according to their chemical composition and shape [159].

Nanopowders of Ni-Mo which can be deposited in any substrate have been fabricated [160]. The advantage is that with a very few catalyst loadings, an overpotential as low as 100 mV and current densities of 10 mA/cm^2 was obtained. Wang *et al.* [161] have studied further the Ni-Mo NPs by eletrodepositing them onto a Cu foam which increased the surface area, overpowering the Pt standard with a 34 mV overpotential at a current density of 20 mA/cm^2 and presented a good stability for 1000 potential cycling. Gong *et al.* [162] exploited the ability of non-noble metals to form oxides by creating a Ni/NiO core-shell structure on carbon nanotubes with catalytic activities similar to Pt.

Fewer non-noble bimetallic NPs were reported to be efficient in acidic environment due to a rapid corrosion of the elements. Tavakkoli *et al.* [163] overcame this problem by fabricating hybrid carbon nanotubes decorated with Fe NPs coated with graphene. The graphene shell proved to be efficient in protecting the core against corrosion in 0.5M H_2SO_4 solutions. This structure showed similar performances than Pt standards and an excellent stability.

In conclusion, I have shown that bimetallic NPs and NW have a huge potential in electrocatalytic applications. This area being quite new, fewer studies on NW as electrocatalysts were reported compared to other NPs. However, with their high surface/volume ratio as well as their capacity to form more complex structures, I believe that bimetallic NW for electrocatalytic application will be the new emerging area in the upcoming years.

2.4.5 Conclusion of the bimetallic NC study

This section has revealed that the synthesis of bimetallic NCs in general is a very complex procedure. Differences in the crystalline structure and the atomic ordering lead to materials with different properties. Thermodynamic parameters as well as kinetics considerations need to be considered in order to obtain the desired material. The complexity of the synthesis allows the design of diverse materials: metal-metal alloy NPs and NW have been successfully obtained by adjusting the reaction parameters allowing their simultaneous reduction. Various core-shell structures with ultrathin to very thin shells can be obtained nowadays which unveils a palette of new properties and new applications. For instance, hybrid core-shell CuNi and Cu/rGO TC have been fabricated with better optoelectronic properties and a better resistance to oxidation. These core-shell NW still suffer from an increase of their resistance due to an increase of their diameter, however.

A better understanding of the parameters required for the synthesis of bimetallic NCs allowed researchers to tune their shape and chemical composition and some have shown outstanding electrocatalytic activities in different domains such as HER and ORR. Therefore, in order to pursuit the best optoelectronic and electrocatalytic performances possible, the research needs to move towards the fabrication of Cu based NW alloys and explore the broad new applications they can offer.

2.5 Conclusion of the literature review

CuNW have the potential of being the next generation TC as well as a treasured catalyst owing their excellent optoelectronic properties and their low cost. In the last few years, CuNW films have improved greatly due to a better understanding of the material and a better control of the NW defects. Combining CuNW with other materials such as graphene oxide or other metals to obtain core-shell structures is a very effective method to passivate the surface of the wire. Therefore, highly conductive, transparent and stable CuNW thin film hybrids have been achieved. Regarding the performances of TC, CuNW is now similar to AgNW and ITO.

Therefore, this thesis will focus on the synthesis of CuNW and Cu based NW and investigates the fabrication and application of CuNW based TC in the next chapters. The next chapter will show the different experimental techniques used for NW synthesis, TC fabrication and application.

3 Materials and methods

This chapter discusses the different experimental methods used to produce both NW and NW TC. These comprise the methods to synthesise NW, their surface modification, NW characterisation, thin film fabrication and testing.

3.1 NW synthesis

3.1.1 General method

3.1.1.1 *CuNW synthesis*

CuNW were synthesised using a modified version of the method reported by Guo et al[6]. In a typical procedure, 2.4 mmol of $CuCl_2.2H_20$, 1 mmol of $Ni(acac)_2$ and 20 mL of OLA were added to a three neck round bottomed flask with a Liebig condenser attached. A summary of the quantity of reagents are summarised in Table 1 and a schematic of the apparatus is shown in Figure 17.

Reagents	Quantity (mmol)
$CuCl_2$	2.4
$Ni(acac_2)$	1
OLA	60.8

Table 1. Summary of the reagents and the quantity used for the synthesis of CuNW.

Under a gentle flow of argon, the mixture was first heated up at 80°C until all the precursors had dissolved and then heated to 180°C for 3h. After reaction, the mixture was left to cool to room temperature. 20 mL of hexane was added to the mixture and transferred to a 50 mL vial. A 1:1 mix of a non-polar/ polar (acetone/hexane) solvents was then added. Acetone helps to remove excess surfactant while hexane is a good solvent for dispersing NW. The mixture was then vortex mixed, sonicated for 5 min and centrifuged at 6000 rpm for 5 min three times to remove the excess of ligands. CuNW were finally re-dispersed in toluene and stored in a N_2 environment. The product was primarily composed of NW. By-products in the form of cubic and spherical nanoparticles of different diameters were also present.

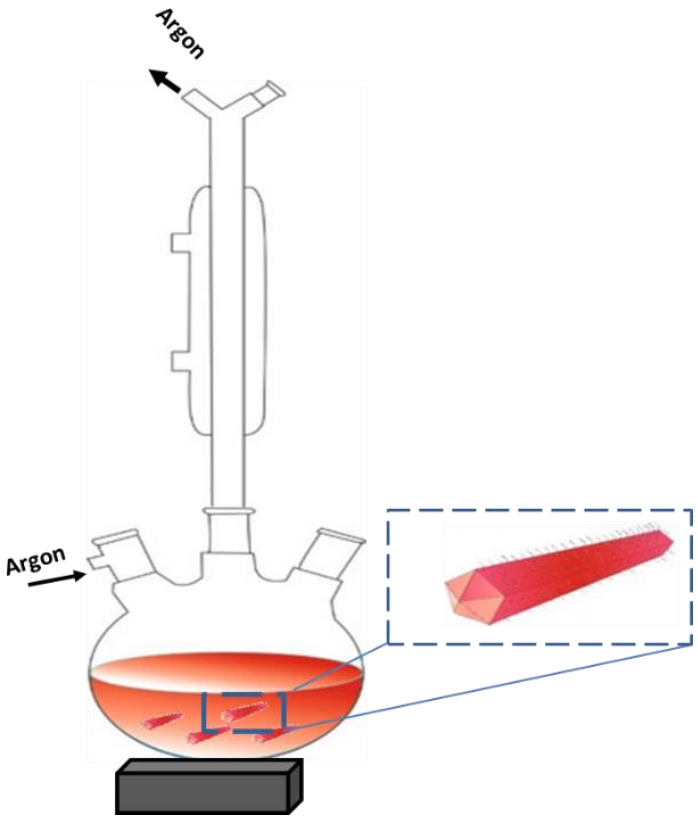

Figure 17. Schematic of an apparatus containing CuNW, zoom on a wire.

3.1.1.2 *NiNW synthesis*

In a typical synthesis, 2.1 mmol of $NiCl_2$, 0.8 mmol of $Zn(acac)_2$, 15 ml of OLA and 5 ml of ODE were added to a three-neck flask and the synthesis was carried out in the same way than for CuNW synthesis which was detailed in the previous section.

3.1.2 Lamellar phase

CuNW grow within a lamellar phase composed of hydrophobic alkyl chain bilayers and amine groups. OLA is used here to reduce $CuCl_2$ into copper seeds which further grow into CuNW as shown in Figure 18. After the synthesis, cleaned CuNW are redispersed in hydrophobic non-polar solvents.

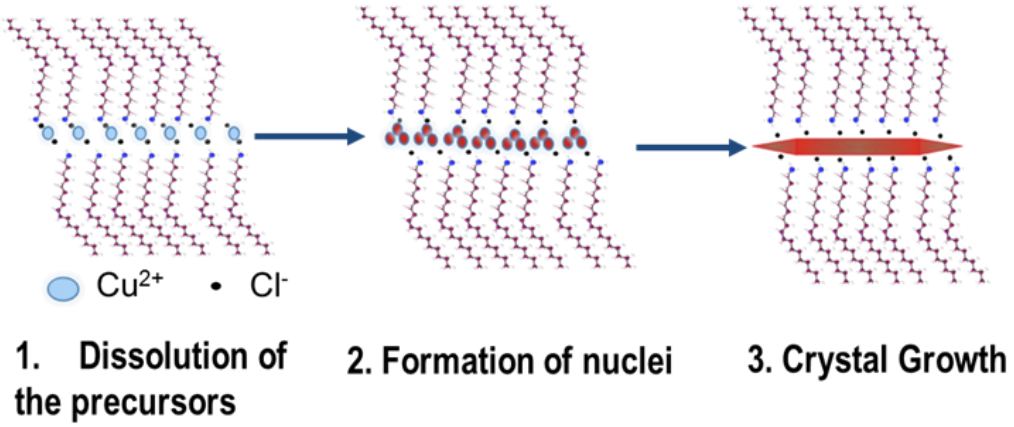

Figure 18. Schematic of a lamellar phase.

3.1.3 Effect of Ni precursor

Regarding CuNW synthesis, the presence of $Ni(acac)_2$ helps to decrease the amount of time necessary to reduce the Cu^{2+} precursor. In fact, without the nickel salt, Yang *et al.*[164] have synthesised CuNW with a length of 30 µm and a diameter of 63 nm using CuCl and OLA at 170 °C in a total period of 61h. This time was necessary to increase the length of the NW. The mechanism can be described as follows: first OLA reduces a small amount of Ni into Ni^0 and a potential difference between the metallic Ni and Cu^{2+} results in the reduction of Cu^{2+} into metallic Cu and metallic Ni^0 goes back to its original state. The Ni^{2+} ions are washed away during the cleaning process described above.

3.2 Fabrication of TC

Thin films were fabricated using a transfer stamp method which will be detailed in the following paragraphs.

3.2.1 Substrate pre-treatments

Depending on the nature of the NW (either hydrophilic or hydrophobic), the substrate needs to be treated in consequence. I will explain the two mains methods I developed depending on the nature of the NW.

3.2.1.1 *Hydrophobic treatment: Silane treatment*

CuNW in toluene are wrapped with an organic layer of OLA that renders them hydrophobic. Therefore, NW can adhere more easily onto hydrophobic substrates. Glass is naturally hydrophilic due to the presence of OH bonds. In order to make it hydrophobic, a silane treatment of the glass was proceeded as follows: glass substrates were soaked in a 5 wt% solution of trimethoxy(propyl)silane in toluene for a minimum of 24 hours then left to dry for 10 min in a fumehood. No further treatments were required.

3.2.1.2 *Hydrophilic treatment*

Due to the presence of defects, Cu is a naturally hydrophilic element and a hydrophilic treatment can be applied.

3.2.1.2.1 Lactic acid treatment

First , a lactic acid treatment has been proceeded using the method developed by Won *et al.*[165] with slight modifications. Few drops of a commercially available lactic acid solution were added to the pre-centrifuged NW which were then redispersed in ethanol, vortexed for 1 min and centrifuged at 3000 rpm for 2 min. Then, 10 ml of ethanol were added, and NW were centrifuged at 2000 rpm for 1 min and redispersed in ethanol. The formula of lactic acid is given in Figure 19.

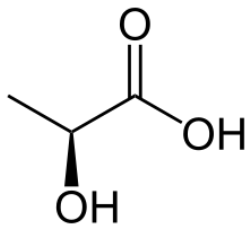

Figure 19. Skeletal formula of a lactic acid isomer.

3.2.1.2.2 O_2 plasmod glass treatment

To improve the adhesion of the lactic acid-treated NW with the substrate, Nanotech PLASMOD plasma chamber purged with O_2 gas was used to treat the glass top surface with charged O_2 plasma. The chamber was initially evacuated to below 100 mTorr using a rotary pump. The chamber was then purged three times with O_2 gas for 10 seconds. Then, a plasma was formed at a power of 100 mVolt under constant H_2/N_2 gas flow of 120 mTorr and the glass was treated for 10s.

3.2.2 Vacuum filtration method

100 µm of the as-synthesised NW were diluted in either 10 ml of toluene (hydrophobic treatment) or 10 ml of isopropanol (hydrophilic treatment). Between 50 µl to 500 µl of solution were dropped onto either a PVDF membrane (hydrophobic treatment) or a cellulose mixed membrane (hydrophilic treatment). Depending on the method chosen, a treated glass substrate was applied on top of the membrane with some pressure. The structure was flipped over, and the membrane was gently peeled off

transferring the NW network onto the glass. A schematic of the procedure is shown in Figure 20.

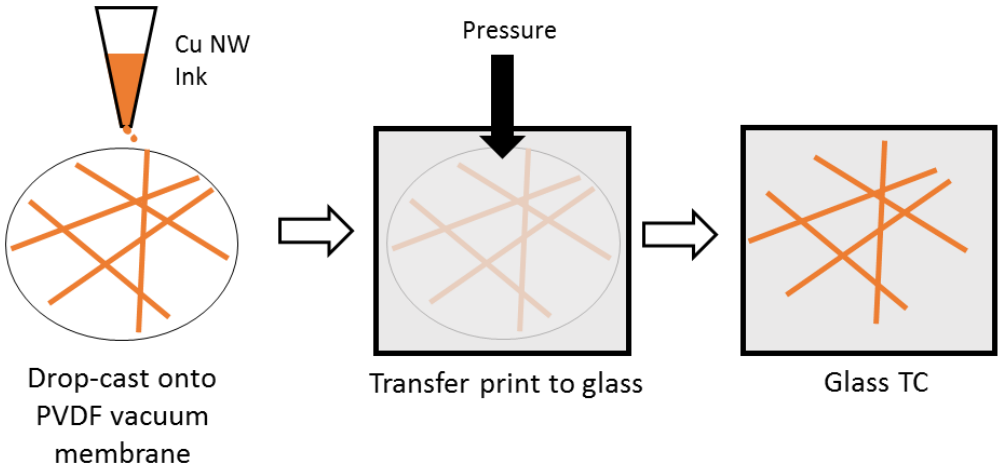

Figure 20. Schematic of the vacuum filtration process.

3.2.3 NW thin film anneal

NW thin films prepared according to the hydrophobic method mentioned above, were not conductive yet due to the presence of the organic layer. Therefore, an anneal step was required in order to remove the conductive layer. Prior to the anneal, NW surface was treated with an H_2 plasma for 30 s at 120 mTorr. This pre-annealing step helped to remove a part of the organic layer. Then the films were inserted in an oven and annealed at 200°C for 2h under a H_2/N_2 flow. The anneal step allowed to fuse NW contacts and therefore reduced the overall resistance of the film. For films treated using the hydrophilic method, the effect of the annealing on these films will be investigated in chapter 5.

3.2.4 NW composite film fabrication

3.2.4.1 *Top layer preparation*

3.2.4.1.1 Zinc Oxide (ZnO) synthesis

ZnO NCs were synthesized using the method adapted from Pacholski *et al.* [166] and Li *et al.*[167]: 2.95 g of zinc acetate dehydrate ($Zn(ac)_2$) were dissolved in 125 ml of methanol and kept, under stirring, at 60°C while 1.48 g of potassium hydroxide (KOH) were dissolved in 65 ml of methanol. Then, the solution of KOH was added dropwise to the $Zn(ac)_2$ solution and the reaction mixture was kept, under stirring, at 60°C for 2.5 h. The mixture was centrifuged at 6000 rpm and washed twice using methanol. Finally, a mixture of 5 ml of chloroform and 5 ml of methanol was added to dissolve the ZnO precipitate and the solution was filtered using a 0.45 μm polyvinylidene fluoride (PVDF) filter (bought from Merck Millipore).

3.2.4.1.2 PEDOT: PSS, Ethylcellulose, PVP and polystyrene

Poly(3,4-ethylenedioxythiophene) polystyrene sulfonate (PEDOT: PSS) was bought from Sigma Aldrich and was filtered using a 0.45 μm PVDF filter before spin coating. The 1wt% polystyrene, ethylcellulose and PVP solutions were prepared by mixing 1.15 g of polystyrene or ethylcellulose in 10 ml of toluene and 1.3 g of PVP in 10 ml of ethanol. The solutions were then sonicated using an ultrasonic bath at 35°C until complete dissolution.

3.2.4.2 *NW TC film preparation*

The as-prepared polymers and ZnO solutions were then deposited on top of the NW film using a spin coater at 2000 rpm spin for 1min. The films were kept in the fumehood for 20 min to ensure that all the solvent had been evaporated. NW composites films were stored in a glovebox under a N_2 environment until characterisation.

3.2.5 NW surface treatment: plasma treatment

Different plasma treatments were used to treat the NW film. H_2/N_2 and O_2 plasma treatments were carried out using the procedure described in paragraph 3.2.1.2.2. The thin films were treated for 10 s regardless of the gas used. A more detailed procedure will be explained in chapter 5.

3.3 Characterisation of NW

3.3.1 UV-VIS

UV-Vis is an absorption spectroscopy in the UV-Visible region. For transition metal NPs such as Au, Ag and Cu, it is used to assess the SPR peak. Light absorption of CuNW was measured on a Cary Varian 4000 UV-VIS-NIR spectrophotometer. For solution measurements, diluted CuNW solutions (5 mg/ml in toluene) were added in a quartz cuvette. For solid films, CuNW thin films on clean glass substrate were analysed. Before each measurement, a baseline setting both the 100% transmission and 0% transmission were

measured. Measurements were always taken against a reference sample which was either pure toluene for solution measurements or a clean glass substrate for film measurements.

3.3.2 FTIR

Fourier Transform Infrared (FTIR) spectroscopy is a powerful tool to identify the functional chemicals groups of a sample by measuring the molecular absorption in the infrared. In order to assess the changes in chemical functional groups of ligands and solvents used in this thesis, OLA, non-coordinating solvent and their mixture with the addition or not of Cu^{2+} salts were measured using a Varian UMA-600 spectrometer in the Attenuated Total Reflection (ATR) mode. Details of the measured samples are listed in the relevant sections of chapter 4. Samples were prepared by drop casting solutions on glass. The final spectrum of a sample is an average of 64 scans and the background is taken into account and deducted by the software. The scans were then analysed using *Origin*® as a software.

3.3.3 XRD

XRD was used in this study to identify CuNW and CuNi NW crystalline structures. XRD analysis was performed using a Philips Theta-2-Theta X-ray diffractometer with Cu K radiation (L=1.5418 Å). The scanning speed was as low as 15min/1° due to the small thickness of the film. Samples were prepared

by drop casting thick (15 mg/ml) NW dispersions onto 20*20 mm^2 glass substrate.

3.3.4 SEM

SEM images were taken using a JEOL JSM-840F Scanning Electron Microscope (SEM), equipped with a cold cathode field emission gun, at a voltage of 5 kV. Typically, Cu and CuNi NW were drop cast onto a 10*10 mm^2 silicon chip glued on a 12.5 diameter metal holder. A 3-nm platinum coating was deposited on top of NW to render the film conductive. Images acquired by SEM were used to assess NW quality as well as determining the averaged aspect ratio of about 100 synthesized Cu and CuNi NW. *ImageJ*® software was used to measure both NW length and diameter.

3.3.5 TEM

To assess the morphology of NW, determine their composition and their crystallinity, NW were examined under a JEOL 2010 TEM, with EDX capability, operating at 200 kV and the Oxford JEOL 2200MCO Aberration Corrected, Monochromated FEG-TEM operating at 200 kV. The JEOL 2200MCO was operated and was used to obtain more precise images. TEM samples were prepared by making dilute dispersions of NW and drop cast few µl on a TEM grid (lacey carbon Au grid) that was dried in ambient conditions. No additional treatments were performed unless specified. High-Resolution Transmission Electron Microscopy (HRTEM) analyses were carried out by Miss Inji Yeom, a colleague in our lab, Dr Christopher Allen and Professor Andrew Watt.

3.3.6 STEM

Scanning transmission electron microscopy (STEM) was used to obtain elemental mapping and line scans of NW composition and elements distribution via Energy Dispersive X-ray Spectroscopy (EDX). They were performed using the JEOL 2100 with LAB_6 source and the JEOL 2200MCO Aberration Corrected, Monochromated FEG-TEM operating at 200 kV. The STEM analyses were carried out by Miss Inji Yeom, Dr Judy Kim and Professor Andrew Watt.

3.3.7 MicroXam

2D and 3D Maps and roughness values of the CuNW network were assessed using an Omniscan MicroXAM 5000B 3D. For each image, the arithmetic average of 3D roughness R_a was measured in a region of 0.6617 mm^2 by summing the averaged roughness of surfaces of peaks and valleys. Both surface and confocal images were taken.

The advantage of the MicroXAM is that it is a non-contact surface analysis technique and therefore it does not damage the surface of the film. Images processing and data analysis were later performed using the free *Gwyddion*® software.

3.3.8 Four-point probe

Measuring the resistivity of NW films helps to assess how well NW are interlinked together i.e. how well the film can conduct the electricity from one

point to another. The four-point probe is the technique chosen to measure the film resistance owing its capacity of measuring an intrinsic resistance of the thin film regardless of its thickness.

The four-point probe consist on four tungsten probes that are equally separated. Two outer probes display a current which is made to flow between the two outer probes while the two inner probes measure the corresponding voltage, making the resistivity of the probes insignificant. This technique presents therefore an advantage compared to a classic multimeter (or two-points measurement) where the high resistance of the probes can throw off the reading.

The resulting voltage, ΔV, was then measured between the two inner probes. Since the thin film measured is of semi-infinite volume and the interprobe spacings s1=s2=s3=s, the R_s can be calculated using the simplified equation below [168]:

$$R_{sheet} = \frac{2\pi}{ln(2)} \frac{V}{I} = 4.52 \frac{V}{I} \quad (10)$$

3.3.9 Dektak

A Veeco DekTak 6M Stylus Profilometer was used to assess the average thickness of each CuNW thin films according to the volume of CuNW solution deposited on the substrate, as well as the film thickness for deposited polymers. A diamond-tipped stylus profilometer with a radius of 12.5 μm was put into contact with the film surface, was subsequently dragged across the surface with a force of 3 mg and measured the height differences (steps) of the thin film during the course of a scan. Setting up both stylus radius and stylus

force helped to control the depth of measurement and therefore control the surface roughness of the film. Prior to the measurement, the NW film was cleaned away using a cotton tip dipped in chloroform in order to form a CuNW thin film band on the glass substrate so that a zero reference will be taken on both sides of the film during the scan.

3.3.10 Integrating sphere

Due to the scattering effects of Cu which are related to the presence of the SPR peak at 580 nm, a part of the incoming light is then reflected in a mirror-like reflection (specular) and in many other directions (diffuse). Therefore, an ISP-REF integrating sphere was used to measure the amount of light reflected. The integrating sphere was coated with a specific white diffusing material that allowed the light to be evenly distribute over the sphere surface.

This technique is very efficient to determine the amount of light reflected. Measurements were taken between 350 nm and 810 nm. An ocean optics STAN-SSH mirror was used as a reference for reflectance measurements.

3.3.11 Hydrogen Evolution Reaction (HER)

NW synthesised in this thesis were investigated as catalysts for HER. All electrochemical measurements were carried out in a three-electrode cell using a Multi Potentiostat VMP3 from Bio-Logic. The HER measurements were carried out with the help of Professor Mauro Pasta in his lab. Dispersions of CuNW, NiNW, 1:1 and 2:1 CuNi alloys (synthesised with the addition of $ZnCl_2$

with 0.81 and 1.23 Zn/Cu initial ratio respectively), and core-shell CuNi NW (obtained with the addition of $Zn(acac)_2$ with a 1.23 Zn/Cu initial molar ratio) were cleaned using a lactic acid treatment detailed in 3.2.1.2.1 and were deposited on a nitric acid pre-treated 1*1 cm^2 glassy carbon. The acid treatment helped to improve the adhesion between the substrate and the NW. Cyclic voltammetry were performed at 100, 50, 20, 10 to determine the surface area. The reference electrode (RE) was Ag/AgCl in saturated KCl, the counter electrode (CE) a graphite rod and the electrolyte, a 1M $HClO_4$ (pH=1) solution purged with nitrogen. Samples were first electrochemically purged in the N_2-purged electrolyte for 10 min. Linear scan voltammetry (LSV) were taken between 0.25V to -0.25 V at a sweep rate of 5 mV/s. The LSV was used to measure the Tafel slope and current density for each sample.

The Tafel equation which is defined for overpotential η higher to 120 mV, is expressed as:

$$\eta = a + b\,log(j) \quad (11)$$

Where:

$$a = -\frac{2.3RT}{\alpha nF} log(j_0)$$

$$b = \frac{2.3RT}{\alpha nF}$$

The LSV generated during the HER measurement will be plotted in the form of the overpotential, η, vs. log(j) in order to determine the Tafel slope.

The overpotential is defined as the difference between the potential E at which the reaction takes place and E_{HER}, the reversible hydrogen electrode (RHE) potential given by the Nernst equation. The resulting graph is known as a Tafel plot, and a and b can be determined by fitting the linear portion of the plot. The intercept will be then used to determine the current density j_0.

4 CuNW synthesis using non-coordinating solvents

4.1 Introduction

4.1.1 Interest in synthesising longer and thinner nanowires

Since the publication of the first CuNW synthesis method by Zeng's group in 2005 [73], several research groups have reported the successful synthesis of high aspect ratio NW in either aqueous solutions [26,27,59] or in organic solvents [6,22,169]. In order to fabricate CuNW based TC with the highest optoelectronic performances possible, it is necessary to obtain longer and thinner CuNW that will minimise the contact between them and therefore reduce the contact resistance. A high yield as well as a minimum of by-products (NPs for instance) are required.

Guo *et al.* [6] have reported a CuNW synthesis with aspect ratios above 1000. However, their synthesis takes more than 10h to obtain less than a gram of NW. In order to obtain high aspect ratio NW with a higher yield and in a shorter time, this chapter will focus on the effect of the addition of a non-coordinating solvent in the synthesis. It is well known that organic ligands have an effect on the growth mechanism and physical properties of the final product [170,171]. This reactivity can be tuned by adding a non-coordinating solvent; non-coordinating solvents are compatible with many ligands and tune the ligand concentration [171,172]. For instance, in the case of CdS NPs, the addition of ODE helps to dilute the ligand which affects the reactivity of the monomer [172]. ODE is a well-established standard non-coordinating solvent

used in various systems [171,173-175] . It has a high boiling point, 320°C that allows it to remain stable during the synthesis of CuNW. It is important to note that the non-coordinating solvent does not participate in the synthesis but modifies the ligand-ligand and ligand-NW interactions. In this chapter, I will study the effect of the addition of different alkyl chain lengths (between C8 to C18) of alkenes and alkanes in the synthesis and study their impact on the morphology and size of the final product.

In the first part of this chapter, I will investigate the effect of a non-coordinating solvent in different systems:

1) Addition of different volumes of ODE in a Cu(OLA) system;
2) Addition of different ratio of OLA:ODE with a given volume of ODE;
3) Effect of the double bond using different sizes of alkane chains;
4) Effect of the size of the chain of the non-coordinating alkene.

In the second part, I will understand the interactions occurring between the non-coordinating solvent, the capping ligand and the precursor.

4.1.2 CuNW synthesis

The XRD in Figure 21)a) shows that the as-synthesised CuNW possess the diffraction peaks associated with the (111) and (200) planes of a face-centered cubic (fcc) structure with a lattice constant equal to a_0 = 3.615 Å. Using an absorption spectrometer, I observe that the NW exhibit a typical 580 nm SPR as shown in Figure 21)b). While the SEM picture in Figure 21)c) shows the

wire-like shape of the NW. I observe that NW form well aligned bundles separated by a thin organic layer that are seen more precisely in the HRTEM pictures in Figure 21)d).

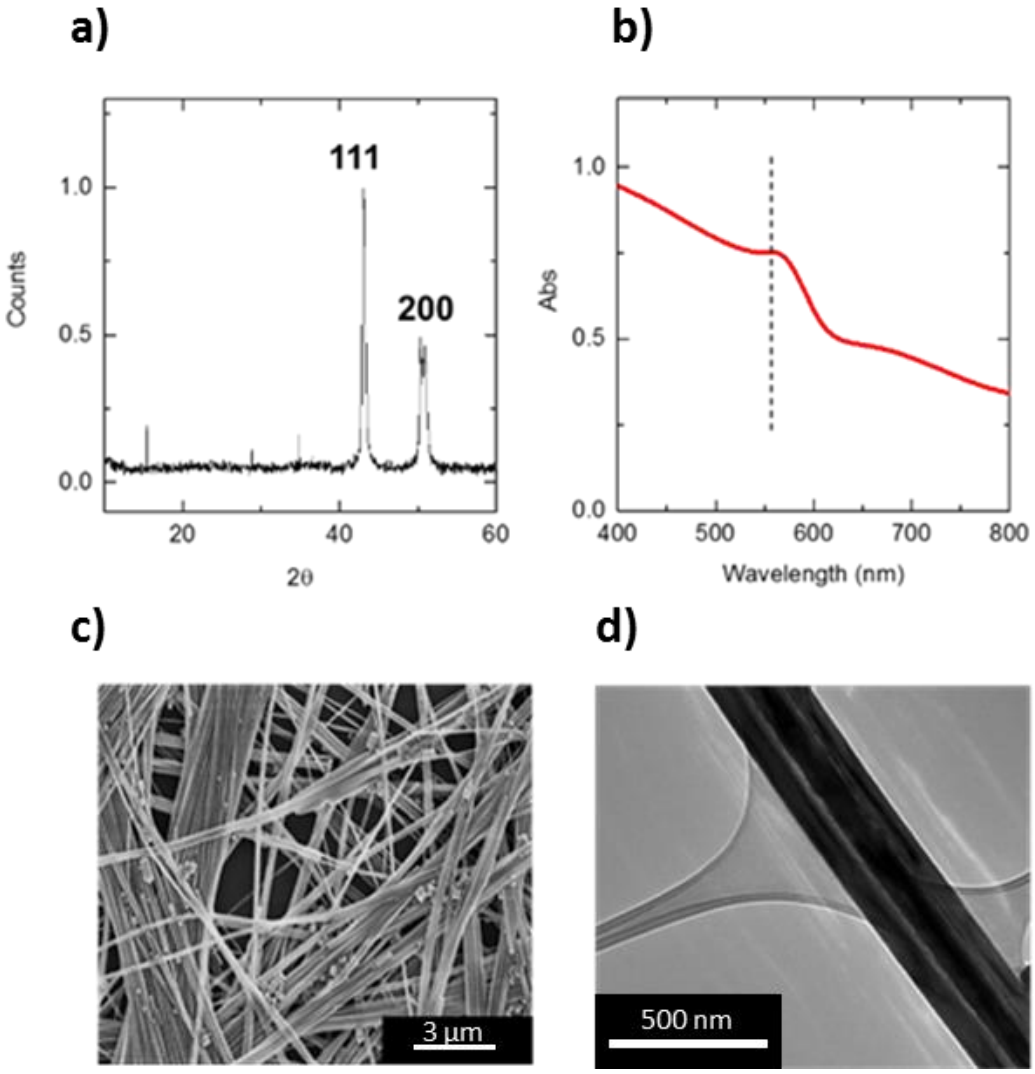

Figure 21. a) XRD of a CuNW film, b) UV-VIS of CuNW dispersed in toluene showing an SPR peak at 580nm, c) SEM of few NW dropped on a silicon chip d) HRTEM image of highly anisotropic NW separated by organic layers.

4.2 Addition of a non-coordinating solvent

4.2.1 Non-coordinating solvent concentration effect

In this section, I will examine the evolution of the CuNW size and morphology upon addition of ODE. The synthesis remains the same as described in 3.1.1 with the addition of between 0 ml to 20 ml of ODE. Table 2 summarises the volume of ODE and corresponding ODE:OLA ratio used in this study.

OLA volume (ml)	ODE volume (ml)	ODE:OLA ratio
20	0	0:1
	5	1:4
	10	1:2
	15	3:4
	20	1:1

Table 2. Corresponding ODE:OLA ratio for each ODE volume added in the synthesis.

Representative SEM images for each volume of ODE are shown in Figure 22 with 0 ml (Figure 22)a)), 5mL (Figure 22)b)), 10mL (Figure 22)c)), 15mL (Figure 22)d)), 20 mL (Figure 22)e)) of ODE added. Both length and diameter size distributions are shown in Figure 23 (average of around 100 NW selected from the SEM images). The size distributions of the NW show that NW length and diameter exhibit a greater polydispersity for volumes above 5 ml. NW formed with 5 ml ODE exhibit less polydispersity in both length and diameter.

The TEM image displayed in Figure 24)a) shows that after the synthesis, NW are wrapped in a very thick organic layer. The HRTEM image in Figure 24)b) shows that the NW are single crystalline with high lattice perfection (lattice fringe, d_{111}= 0.221). The growth direction of these wire is along the <110>. There is no evidence of a copper oxide layer being formed indicating that the organic layer protects the NW from oxidising.

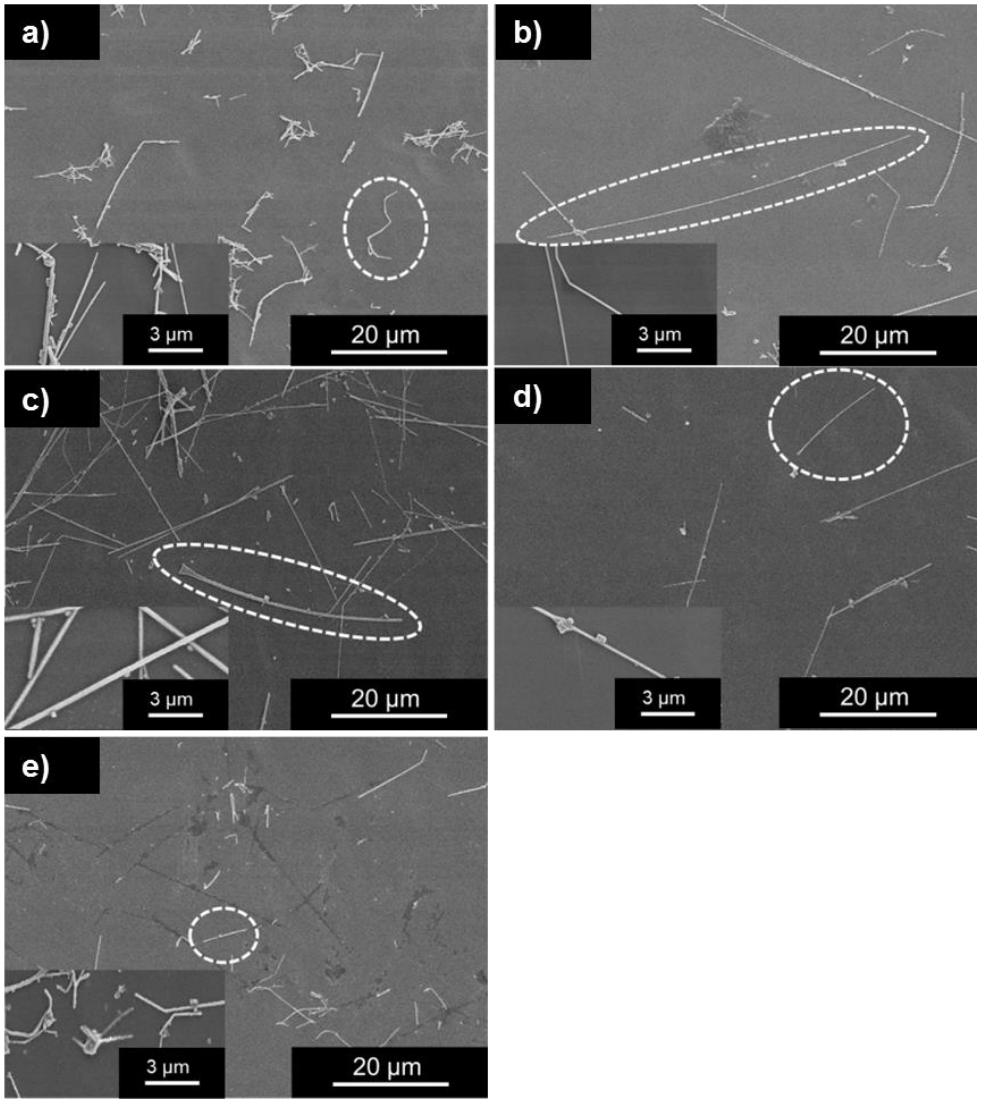

Figure 22. Typical SEM micrographs of NW with an initial ODE volume added of a) 0mL b) 5mL c) 10mL d) 15mL and e) 20mL.

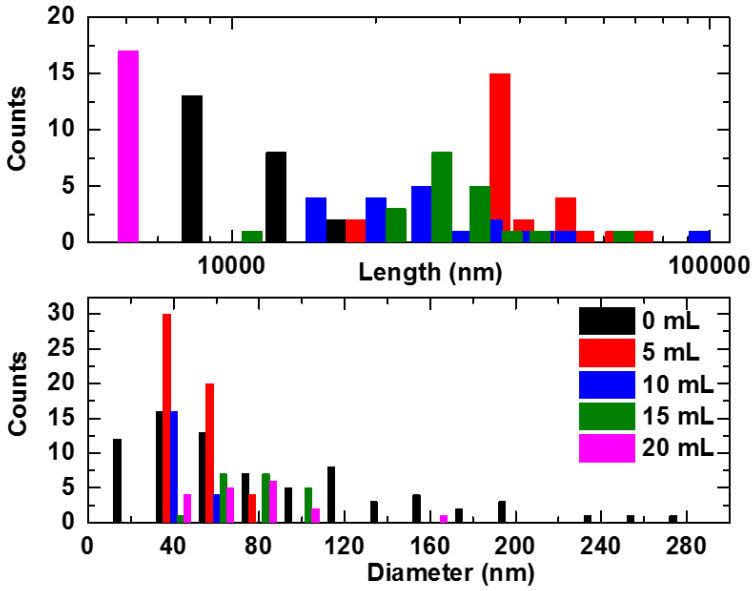

Figure 23. NW length and diameter size distributions for different volumes of ODE added.

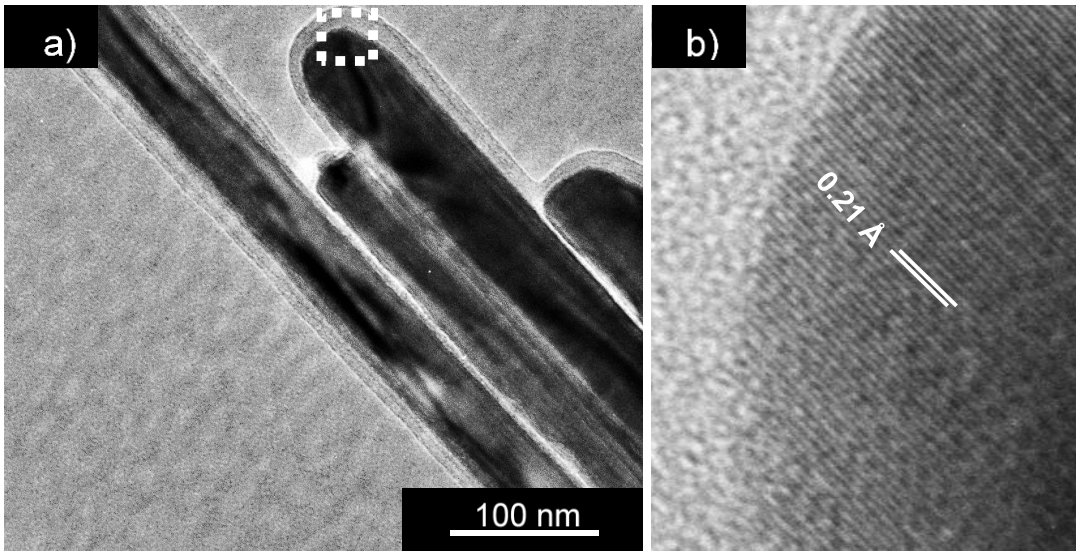

Figure 24. a) TEM image of a single NW before annealing, b) HRTEM of a CuNW end looking down the <111> zone axis.

The EDX STEM images displayed in Figure 25)a) represents the maps of Cu, Ni, carbon and oxygen for NW synthesised using 5 ml ODE. Cu is present while no

trace of Ni is found (Figure 25)c)) confirming that Ni is taking part in the reaction only as a catalyst as suggested in 3.1.3. It is important to note that a small amount of Ni is detected though and is shown in the Ni map in Figure 25)a) and in Figure 25)b). I hypothesise that Ni is present in the small NPs that are by-products of the synthesis therefore explaining their low count. I also observe the presence of carbon and oxygen. Carbon is present in large quantities as shown in the table in Figure 25)c). This is due to the excess of the organic layer surrounding the NW and the carbon support. Oxygen is present as well in small quantities but the mapping in Figure 25)a) shows that it is present on the edges of the NW, close to the organic layer, and probably appears during the cleaning step.

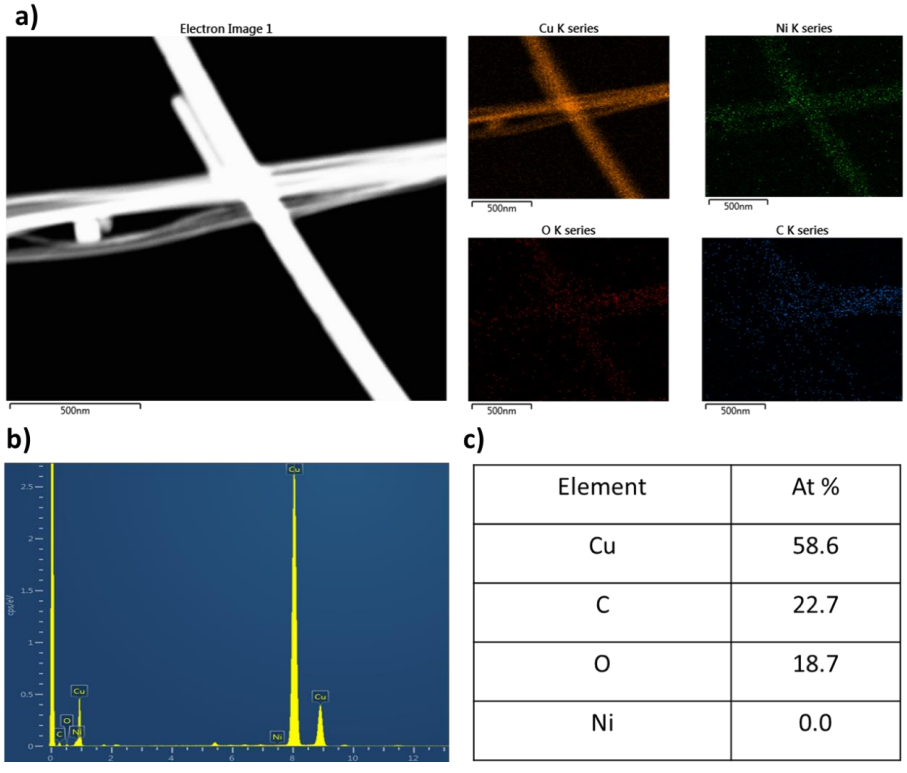

Element	At %
Cu	58.6
C	22.7
O	18.7
Ni	0.0

Figure 25. a) STEM-EDX images of CuNW synthesised with 5 ml ODE after cleaning and EDX mapping of copper, nickel, carbon and oxygen, b) Elemental analysis graph and c) table of the atomic percentage of each element.

Figure 26 shows that changing the ODE concentration induces a change in the aspect ratio. For an ODE:OLA ratio of 1:4, NW are formed with an aspect ratio of 1100, while for a 1:1 ratio, the aspect ratio of the NW drops to 10. Figure 26)a) shows how the length and diameter of the NW varies according to the ODE added volume. Figure 26)b) plots the corresponding aspect ratio for given ODE volumes. The diameter decreases from 85 nm to 40 nm when 5 mL of ODE is added (1:4 ratio) and increases up to 65 nm for a 1:1 ratio while the length passes from 10 μm to 45 μm for a 1:4 ratio and down to 6 μm for a 1:1 ratio. Therefore, the ODE:OLA 1:4 ratio gives the best result in terms of length and diameter. I hypothesise that ODE expands the lamellae structure up to a critical concentration after which the colloid becomes de-stabilized and smaller lamellae are formed. Therefore, the variation of the volume of a non-coordinating solvent induces a change in the final size of the NW. The next section focuses on the influence of the non-coordinating solvent in a system where the volume of the capping ligand (OLA) is varying while ODE remains constant.

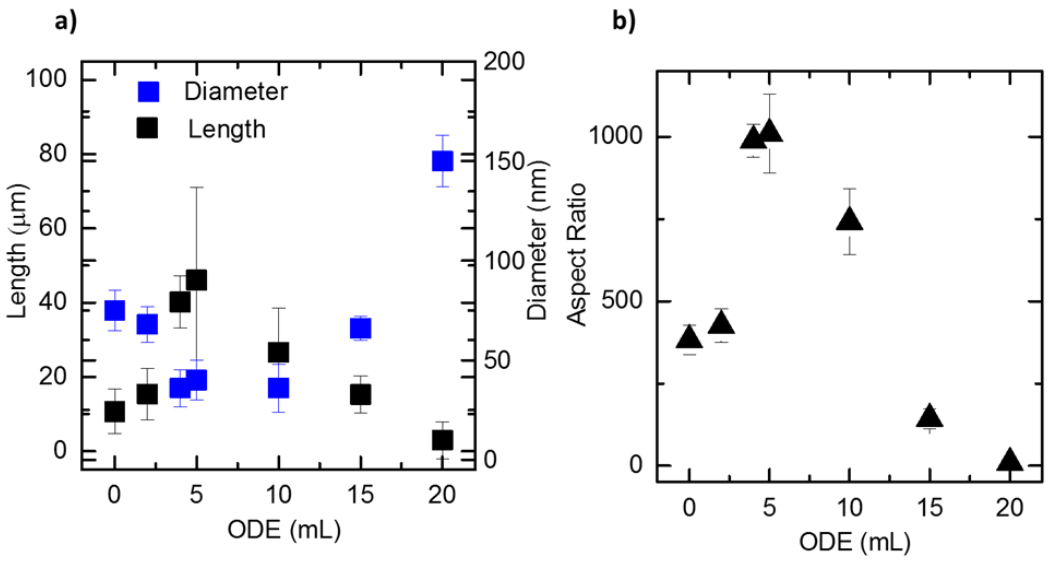

Figure 26. a) Length, diameter and b) the corresponding aspect ratio evolution according to the volume of ODE added.

4.2.1.1 *Effect of the precursor/ ligand ratio*

4.2.1.1.1 With the presence of ODE

In the previous section, I have shown that the addition of a non-coordinating solvent for a given volume of OLA affects strongly the size of the NW. This section will explore the impact of the evolution of OLA concentration on the NW aspect ratio synthesis for a given ODE volume.

For a typical synthesis, the concentrations of Cu and Ni precursors as well as ODE do not vary. OLA volume varies between 8 mL to 25 ml. Table 3 summarises the ODE:OLA ratios studied for a fixed ODE volume.

OLA volume (mL)	ODE volume (ml)	ODE:OLA ratio
8	5	5:8
10		1:2
15		1:3
20		1:4
25		1:5

Table 3. Variation of OLA volumes for fixed ODE volume and corresponding ODE:OLA ratios investigated in this section.

The length, diameter and aspect ratio variation according to the volume of OLA are shown in the graphs in both Figure 27)a) and Figure 27)b). I observe a similar trend than what I have seen previously. A 5:8 ratio in ODE:OLA gives a corresponding length and diameter of 14 μm and 270 nm respectively and thus, an aspect ratio of 50. When increasing the volume ratio of OLA in the system, I observe that the NW length increases, and their diameter decreases for up to 20 ml of OLA. The maximum aspect ratio is obtained for a 1:4 ratio in ODE:OLA which was already discussed in the previous section. A further increase in the OLA volume results in a decrease of the length and an increase in the diameter (11 μm and 140 nm respectively) giving an aspect ratio of 80.

The size distributions displayed in Figure 28)a to Figure *28*)e) for both NW lengths and diameters according to the volume of ODE added, shows that they get narrower when increasing the OLA concentration for up to 20 ml in volume. Higher concentration leads to a decrease in the size distribution of

both length and diameter for volumes of OLA up to 20 ml, and an increase in size distribution for volumes above 20 ml.

These observations go along what have been reported before. In fact, Wang *et al.* [176] showed that the volume of the capping ligand plays an important role in defining the shape of NW.

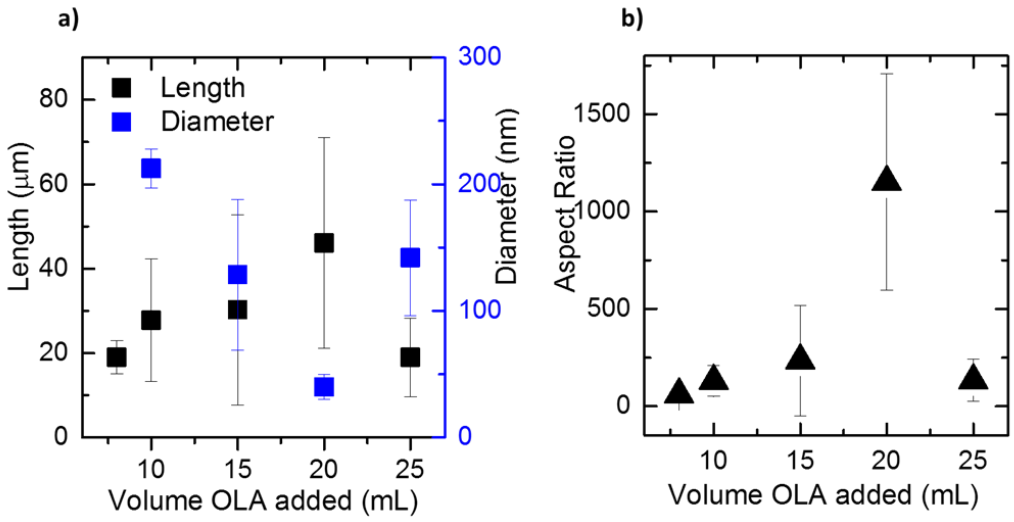

Figure 27. Plots of a) Length and diameter, b) aspect ratio of NW synthesised with different volumes of OLA in the presence of ODE.

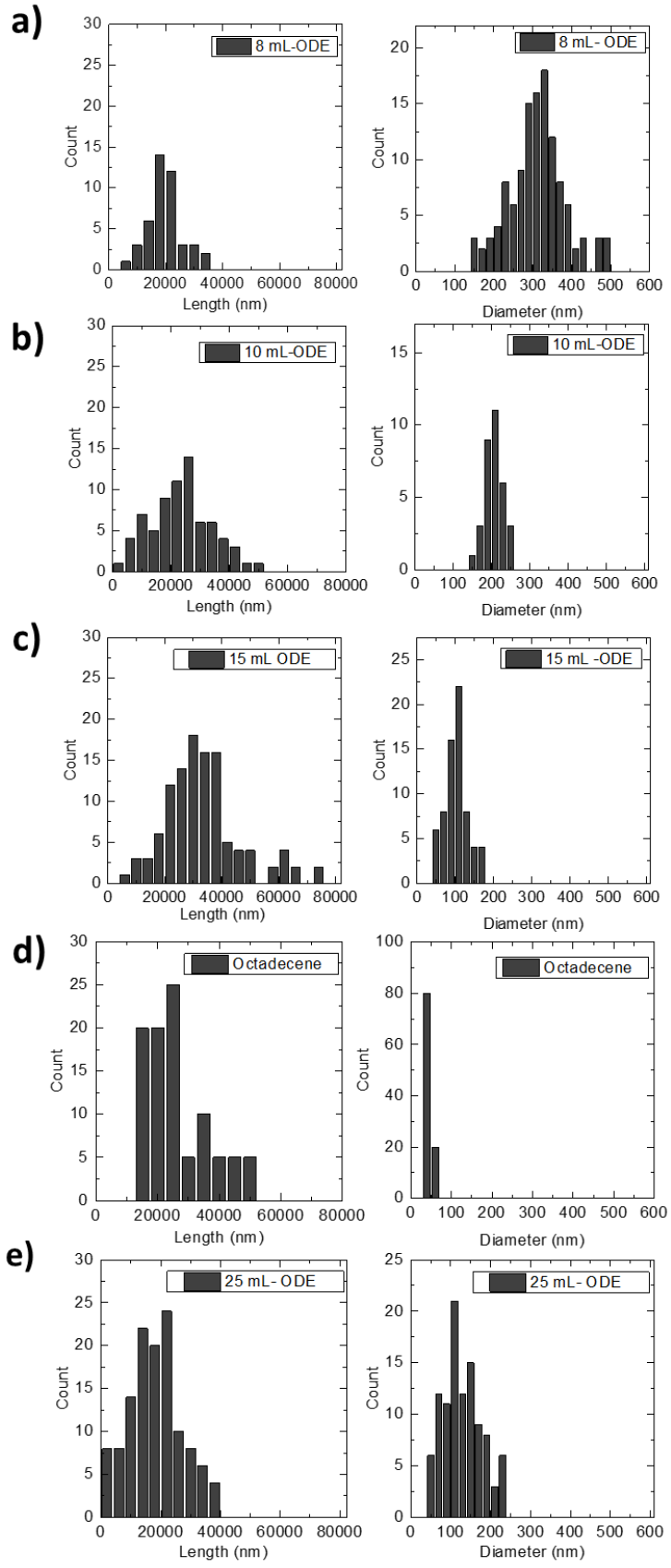

Figure 28. Length and diameter size distributions of NW synthesised with different volume of OLA: a) 8ml, b) 10 ml, c) 15 ml, d) 20ml and e) 25 ml in the presence of ODE.

4.2.1.1.2 Influence of ODE addition

The graph in Figure 29 shows the influence of the non-coordinating solvent on the aspect ratio of NW synthesised using different volumes of the capping ligand, OLA. If the aspect ratio trend is the same in both systems, it is clear that using ODE increases the aspect ratio of the NW with OLA volumes up to 20 ml where the addition of ODE increases the aspect ratio from 130 to 1100 as explained in the previous paragraphs. Further increase of OLA volumes shows that the presence of ODE does not have any more effect on the NW size where the aspect ratio of NW synthesised with and without ODE are nearly identical. Therefore, this result shows that for volumes up to 20 ml of OLA, the addition of ODE has an influence on the morphology and final size of the NW.

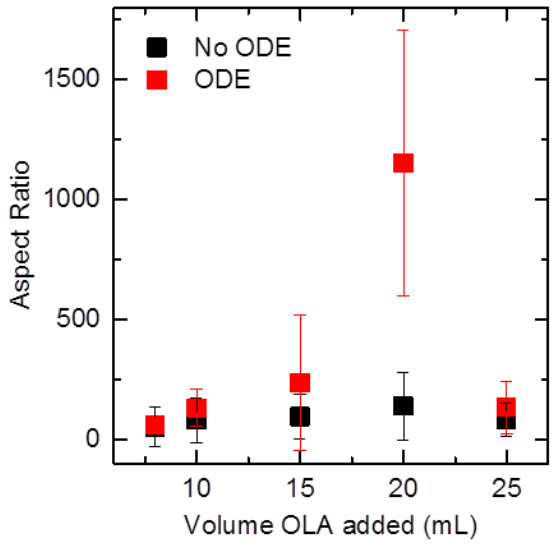

Figure 29. Comparison of the NW aspect ratio for different OLA volumes with and without the initial addition of ODE.

4.2.2 Double bond effect

I have shown in the previous section that the addition of ODE improves greatly the NW aspect ratio for OLA volumes up to 20 ml. In this section, I will explore the addition of alkanes as non-coordinating solvents to see if they induce a change in the aspect ratio as well. Unlike alkenes like ODE, alkanes are saturated solvents that do not possess a double bond and thus, are less likely to react with hydrogen bonds. Different alkyl chain lengths of alkanes (octane, decane, dodecane, tetradecane, hexadecane and octadecane) will be investigated. Alkane volumes are determined so that the Alkane:OLA molar ratio matches the ODE:OLA molar ratio.

Table 4 provides the volume added to attain the equivalent molar ratio of the 1:4 ODE:OLA system studied in 4.2.1, for each alkane studied in this section.

Alkane	Volume added (ml)	Equivalent ODE:OLA ratio
Octane	2.6	1:4
Decane	3.1	
Dodecane	3.6	
Tetradecane	4.2	
Hexadecane	4.7	
Octadecane	5.2	

Table 4. Corresponding volume to obtain the 1:4 ODE:OLA molar ratio for each alkane studied.

The graphs in Figure 30 plot the length and diameter (Figure 30)a)) and the resulting aspect ratio (Figure 30)b)) according to the length of the alkyl chain of the alkane that was added at the beginning of the synthesis.

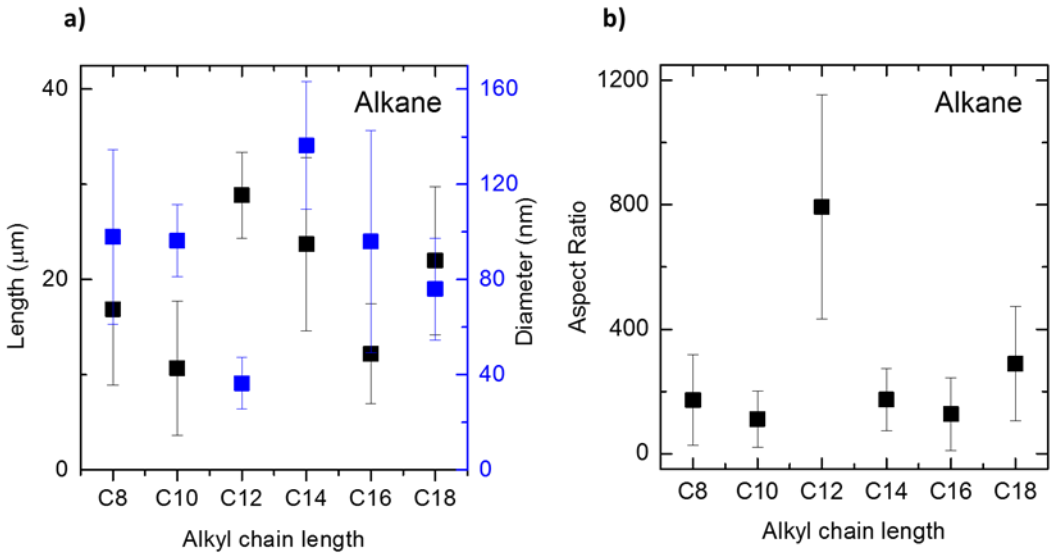

Figure 30. Plots of a) length and diameter and b) the corresponding aspect ratio of NW according to the length of the alkane alky chain.

Unlike the previous observations in section 4.2, the variation in the average length does not follow a trend when passing from one length of chain to another: NW synthesised in presence of either octane (C8), decane (C10) or hexadecane (C16) have an average length in the 10 µm–20 µm range, while dodecane (C12), tetradecane (C14) and octadecane (C18) form NW with lengths between 20 µm to 30 µm. The length is optimal for the middle alkyl length C12 (29 µm). The diameter is more stable with C8, C10, C16 and C18 giving NW with an average diameter between 70nm to 100 nm. However, the smallest diameter is obtained using C12 as a non-coordinating solvent and the

highest diameter is obtained with C14. The aspect ratio is between 40-50 for all the alkane chain lengths studied with the notable exception of C12 where the aspect ratio jumps up to 800. A summary of the length, diameter and corresponding aspect ratio according to the type of alkane chosen, is shown in Table 5 below.

Non-coordinating solvent	C	Boiling point (°C)	L (µm)	D (nm)	Aspect Ratio L/D
Octane	8	125	17±8	98±37	173±146
Decane	10	174	11±7	96±15	115±91
Dodecane	12	216	29±4.5	36±11	805±360
Tetradecane	14	253	24±9	136±27	176±100
Hexadecane	16	287	12±5.2	96±46	125±116
Octadecane	18	317	22±7.8	76±21	290±184

Table 5. Boiling point, Length (L), Diameter (D) and corresponding Aspect Ratio (L/D) of the CuNW synthesised in presence of different alkyl chain lengths (C) of non-coordinating alkane.

A number of conclusions can be drawn from these results:

1) The aspect ratio of the NW is higher for mid-length alkyl chains. In addition to that, a drop in the diameter size is observed for C12. This result is even more surprising given that with C14 alkane whose carbon chain length has only 2 more carbons than C12, the results are completely different. I can conclude that for a medium length ligand, the anisotropy of the NW is greater than for any other lengths.
2) It is also interesting to note the effect of the absence of the double bond on the aspect ratio of the NW. When replacing ODE with alkanes, I

observe that the aspect ratio of the NW is significantly smaller. A hypothesis is that the presence of a double bond might contribute to the increase of the number of atoms reduced. A question yet to be answered is to know whether this reduction occurs, before or after the nucleation.

The ligand chain length can affect the size of the NCs. Dumestre *et al.*[177] have observed that using intermediate chain length (i.e. C14 and C16) ligands improve the anisotropy of cobalt nanorods by increasing the aspect ratio. A possible explanation is that monomers bound to shorter length ligands are more reactive because they are less sterically hindered. They reduce quickly and produce more nuclei[176]. However, the presence of more nuclei means that fewer atoms are formed to promote the formation of longer NCs therefore explaining the presence of shorter lengths. On the other hand, a longer chain ligand makes the monomer more hindered which means that it is less reactive. In other terms, less nuclei will be formed but more precursors will be reduced in the form of atoms which means that the system will have less control on the anisotropy of the NW [171,178]. A trade-off between these two phenomena is to choose middle length ligands that will help forming a significant amount of both nuclei and atoms for the crystal growth while controlling the elongation of the NW.

4.2.3 Effect of the size of chain of the non-coordinating solvent

The ODE study in paragraph 4.2.1 showed that the addition of different volumes of ODE has a direct influence on the final aspect ratio of the synthesised NW. In the present section, I will investigate the effect of the alkyl chain length on the final size of NW using different alkenes: 1-octene (C8), 1-decene (C10), 1-dodecene (C12), 1-tetradecene (C14), 1-hexadecene (C16) are compared with ODE (C18) studied previously. The concentration of Cu and Ni salts, OLA and the alkene are kept the same than previously. The only variable is the alkyl chain length of the non-coordinating solvent. Alkene volumes are determined so that the Alkene:OLA molar ratio matches the 1:4 ODE:OLA molar ratio. Table 6 provides the volume added to attain the equivalent molar ratio of the 1:4 ODE:OLA system studied in 4.2.1, for each alkene studied in this section.

Alkene	Volume added (ml)	Equivalent ODE:OLA ratio
1-Octene	2.51	1:4
1-Decene	3	
1-Dodecene	3.5	
1-Tetradecene	4.1	
1-Hexadecene	4.6	
1-Octadecene (ODE)	5	

Table 6. Corresponding volume to obtain the 1:4 ODE:OLA molar ratio for each alkene.

I hypothesise that the variation of the alkyl chain length of the non-coordinating alkene solvent will induce a change in the reactivity between OLA and the Cu precursor.

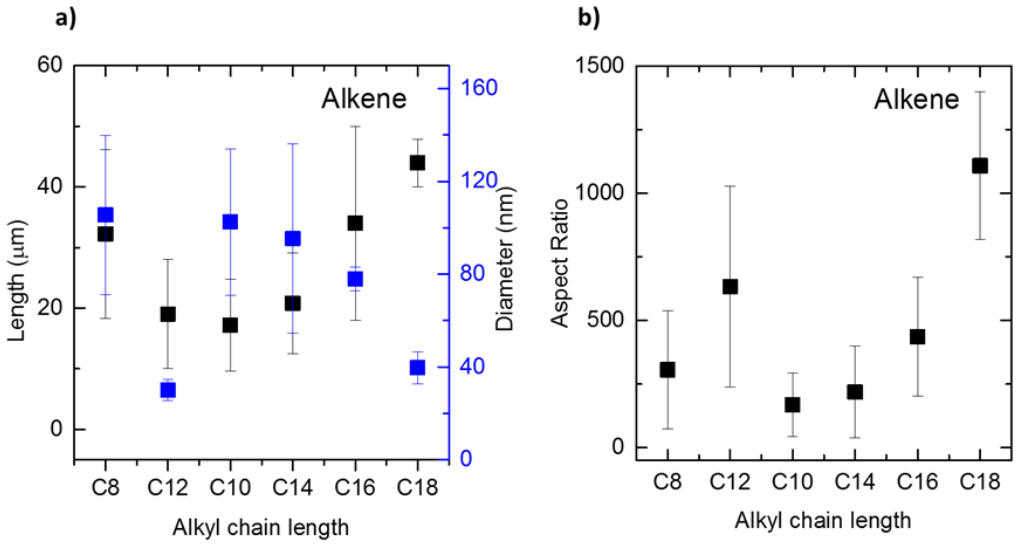

Figure 31. Plots of a) length and diameter and b) the corresponding aspect ratio of NW according to the length of the alkene alky chain.

The length of the NW decreases from 32 µm to 18 µm when the alkyl chain passes from 8 to 10 carbons and increases up to 20 µm for C14 and 44 µm for C18 as shown in Figure 31)a). Fewer changes are observed for the diameter: the diameter decreases slightly from 105 nm for C8 to 95 nm for C14. However, I observe that the diameter dramatically decreases for C12 and C18 reaching 30 nm and 40 nm respectively. The resulting aspect ratios show that NW exhibit ratios ranging from 300 to 170 for C8 to C10 respectively and increases up to 1100 for C18 (Figure 31)b). NW are thinner with the presence of C12 alkene in the synthesis giving an aspect ratio of 630. The influence of

the alkyl chain length of the alkene on the length, diameter and corresponding aspect ratio is summarized in the Table 7 below.

Non-coordinating solvent	C	Boiling point (°C)	L (µm)	D (nm)	Aspect Ratio L/D
Octene	8	121	32±14	105±35	305±230
Decene	10	170	17±9	102±5	167±395
Dodecene	12	214	197.5 ±	30±32	630±125
Tetradecene	14	233	21±8.3	95±41	221±180
Hexadecene	16	284	34±16	78±5	435±230
Octadecene (ODE)	18	315	44±4	40±7	1100±300

Table 7. length (L), diameter (D) and corresponding aspect ratio (L/D) of CuNW synthesised in presence of different alkyl chains (N) of non-coordinating alkene.

NW are smaller in size when short alkyl chain non-coordinating solvent are used but their diameter is bigger. Therefore, a general trend is that the aspect ratio of the NW is smaller when using short length alkenes. NW synthesised using 1-octene have an aspect ratio slightly bigger than NW synthesised using 1-decene for instance. Octene like octane has a boiling point lower than the temperature of reduction of Cu^{2+} salts which means that 1-octene will evaporate before CuNW are formed. It is interesting to note that the length, the diameter and the resulting aspect ratio of the NW using 1-octene as a non-coordinating solvent are still much higher than the ones synthesised without the presence of a non-coordinating solvent as shown in Figure 29 (section 4.2.1.1.2). This shows that even though the alkene is not present when the NW are formed, it still plays role in tuning the total size and morphology of the NW. Therefore, I can deduce that the non-coordinating solvent plays a role in the reactivity of the monomer prior to its reduction into atoms. This result goes in

the sense of what many have observed before. Different research groups have shown that the use of a non-coordinating solvent allows to tune the reactivity of the monomer in various systems [171,172,176].

I have shown in the previous section that middle length alkanes are the best candidates for increasing the aspect ratio of the NW. This phenomenon is not observed with the alkenes. The double bond that the alkene possess might play a key role in the formation of highly anisotropic NW. Alkene provide longer aspect ratio than alkane for all the lengths with the exception of the C12 chain. The presence of a double bond could be the reason for the increase of the aspect ratio. An explanation can be that the double bond of the alkene participates in the reduction of Cu precursor [73]. Therefore, even though the chain length is higher, the double bond will provide more nuclei than single bonds which explains NW longer lengths obtained when using for alkenes.

The addition of both middle chain ligands C12 dodecene and dodecane in the synthesis form thin NW with diameter of 30 and 36 nm respectively suggesting a better control of the NW anisotropic growth with the presence of these non-coordinating solvents regardless of the presence of the double bond.

4.3 Ligand precursor interaction study

4.3.1 Principle

To understand the ODE effect on NW aspect ratio, I investigate the interaction between OLA, ODE and $CuCl_2$ using FTIR techniques. The FTIR spectra of

mixtures of reaction precursors after heating under argon at 80^{0}C for 20 minutes are show in Figure 32. Spectra are presented in the range of a) 1000-1500 cm^{-1} and b) 3000-3600 cm^{-1} to show clearly the most relevant bands. All peak height changes described here are normalised to the C-C stretch peak at 720 cm^{-1}.

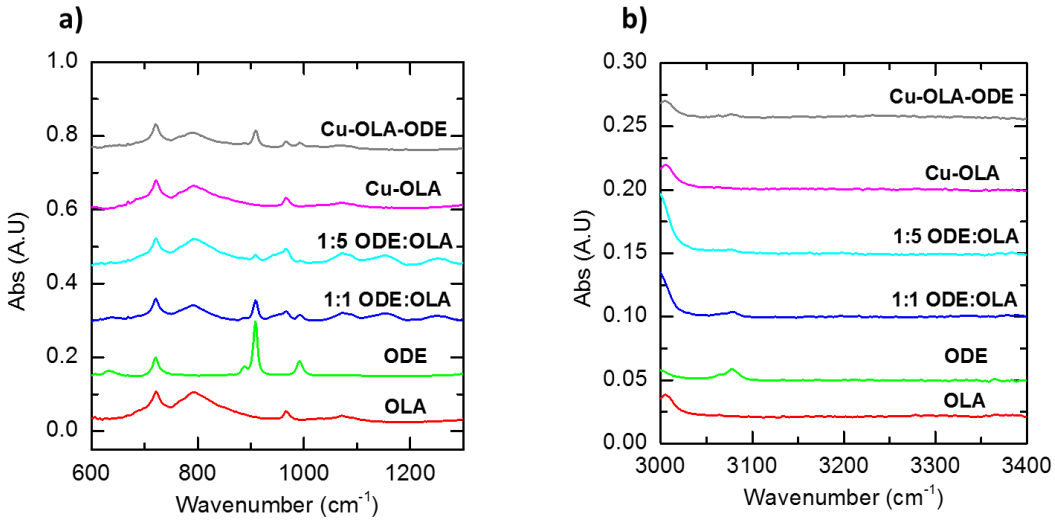

Figure 32. FTIR spectra of OLA, ODE, 1:4 and 1:1 ODE:OLA mixtures, Cu(OLA) and Cu((OLA)(ODE)) mixtures in a) the 600 cm^{-1}- 1400 cm^{-1} region and b) the 3000 cm^{-1}- 3400 cm^{-1} region.

In a mixture of OLA and ODE with no presence Cu^{2+}, two new features at 1150 cm^{-1} and 1250 cm^{-1} are observed in the C-N region, indicating the formation of a new bond between the N-H bond of the OLA and the double bond of the ODE. This is further supported by the decrease of the ODE double bond peak at 3077 cm^{-1}. If more OLA is added, then this double bond completely disappears, suggesting a dynamic system where a bond between N-H of the OLA and C=C of ODE is easily formed and broken. Upon addition of the Cu precursor to the ODE:OLA mixture, the C-N peaks at 1150 cm^{-1} and 1250 cm^{-1} disappear

suggesting that it is preferential for a Cu-ammine complex to form. I hypothesise that a competing reaction between ODE:OLA and Cu:OLA occurs which is more in favour of Cu:OLA than ODE:OLA. The Table 8 summarize the peaks observed and their corresponding assignment.

It is well established that long alkylammine chains self-assemble into lamellar phases in the presence of metal halides precursors [43,179]. Du *et al.* [180] showed that a CuCl(OLA) mixture forms a lamellar structure in presence of octylamine. Co-solvent/surfactant effects have also been observed by Larche *et al.* [181] who showed that a lamellar lyotropic crystal in a surfactant-water system can be swollen by the addition of an alcohol. While Lagaly *et al* .[182] showed that in the case of an alkylammonium silver precursor, long chain alkane addition swelled the lamellar phase. In a similar way, the addition of ODE might disrupt the lamellar phase formed by Cu-OLA leading to either an increase or a decrease of the aspect ratio of the NW.

Peak intensity	Group band
720 cm^{-1}	C-C stretch
800 cm^{-1}	N-H wag
910 cm^{-1}	=C-H bend
960 cm^{-1}	=C-H bend
990 cm^{-1}	=C-H bend out of plane
1072 cm^{-1}	-C-N stretch
3077 cm^{-1}	=C-H stretch

Table 8. Representative peak intensity and allocated band name for OLA and ODE.

4.3.2 Case of the alkenes

4.3.2.1 *Principle*

In the previous work, I have identified a key region where a potential bond might be formed between OLA and ODE. In this section, I will focus on the alkyl chain size interaction effect with the capping ligand and with the Cu precursor. I will focus on the 600-1400 cm^{-1} region as it seems that it is the region where the most important changes occur.

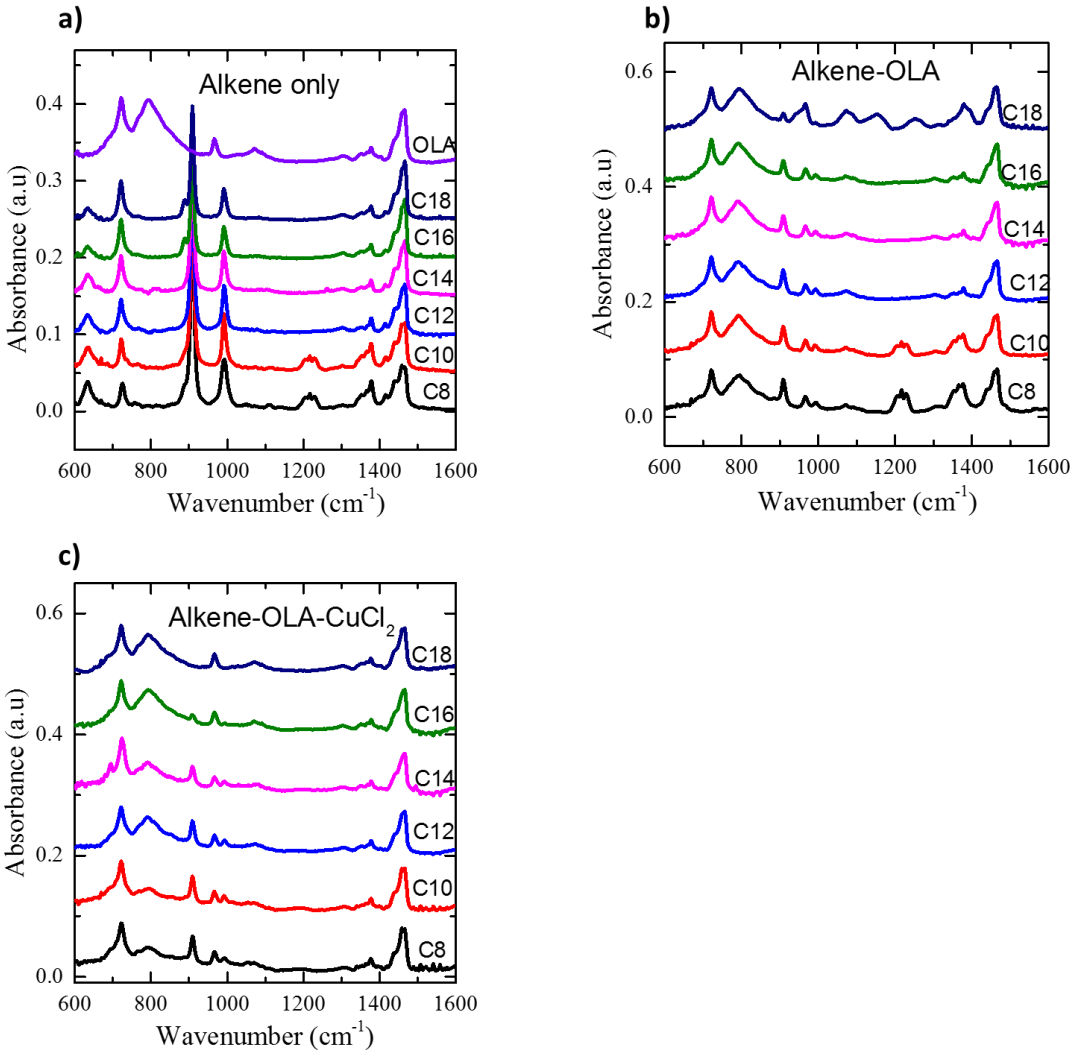

Figure 33. Plots of the FTIR spectra for different sizes of alkyl chains of a) alkenes, b) alkenes-OLA mixtures and c) alkenes-OLA-$CuCl_2$ mixtures in the 600 cm^{-1}- 1400 cm^{-1} region.

4.3.2.2 *Effect of the chain length (alkene only)*

The spectra shown in Figure 33)a) looks similar for different alkyl chain lengths but some differences remain. The main features are a decrease of both 910 C=C cm^{-1} and =C-H 990 cm^{-1} peaks intensity with the increase of the alkyl chain length and the presence of a broad peak at 1210 cm^{-1} in the C-N region for the shorter alkyl chains only.

4.3.2.3 *Effect of the chain length (with OLA only)*

Upon addition of OLA, I observe the apparition of OLA peaks at 720 cm^{-1}, at 800 cm^{-1}, at 1200 cm^{-1} and at 1400 cm^{-1} (Figure 33)b)). The =C-H peak at 990 cm^{-1} has decreased in intensity due to the interaction between OLA and the alkene.

It is very important to note that the intensity of the N-H peak at 800 cm^{-1} remains unchained independently of the alkyl chain length which indicates that the nature of the interaction between OLA and the alkene is not involving the alkyl chain length. I hypothesised earlier that the interaction between OLA and ODE involves the double bond of the ODE and the amine group of the OLA. This result gives a confirmation of this hypothesis.

In the specific case of the C18 alkene (ODE), I observe a new feature that is not seen for the other types of alkenes. I have mentioned earlier the introduction of two peaks when ODE and OLA are mixed together. Another interesting feature is that for C18, the C=C peak is broader than for the other chains. A

possible explanation is that the peaks that appear are due to a stronger interaction of OLA with ODE than with the other alkenes.

4.3.2.4 *Effect of the chain length ($CuCl_2$ and OLA)*

The Cu(OLA:alkene) mixture has been studied for different lengths of alkyl chain. All the attributed peaks are shown in the plot in Figure 33)c). At 800 cm^{-1}, the N-H peak intensity decreases even more for shorter alkyl chains. This confirms that the alkyl chain length has an influence on the bonding strength between OLA and Cu precursor. Therefore, in the case of the alkenes, when the alkyl chain length decreases, the OLA binds more strongly to the precursor. I hypothesised previously that the size of the chain has an effect on the monomer reactivity. Here depending on the alkyl chain length, the ligand binds with a different intensity to the precursor.

In which term can a ligand bind differently to the precursor? A stronger intensity can be translated as monomer reactivity. The more the ligand is strongly bound to the precursor, the more reduction occurs during the stage of pre-nucleation, therefore leading to the formation of more nuclei. I observe that the length of the non-coordinating solvent has also a strong influence on the binding strength of the ligand with the precursor. Other features appear to indicate that the binding strength is different according to the chain. The N-H peak observed at 1072 cm^{-1} is not seen any more for the shorter carbon chains, i.e. C8 and C10. In addition to that, the=C-H peak at 990 cm^{-1} decreases when the alkyl chain length increases. This suggests that for shorter alkyl chain solvents, the interaction between the Cu^{2+} salt, OLA and the alkene system is

more in favour of a binary complex Cu:OLA while for longer chain solvents this interaction is less powerful. Therefore, I can deduce that the length of the alkyl chain has an influence on the reactivity of OLA with the precursor. The longer the chain, the less reactive is OLA. Therefore, longer alkyl chain will be more stable within the lamellar phase than shorter chains.

4.3.3 Effect of the nature of the chain: study of the Alkane

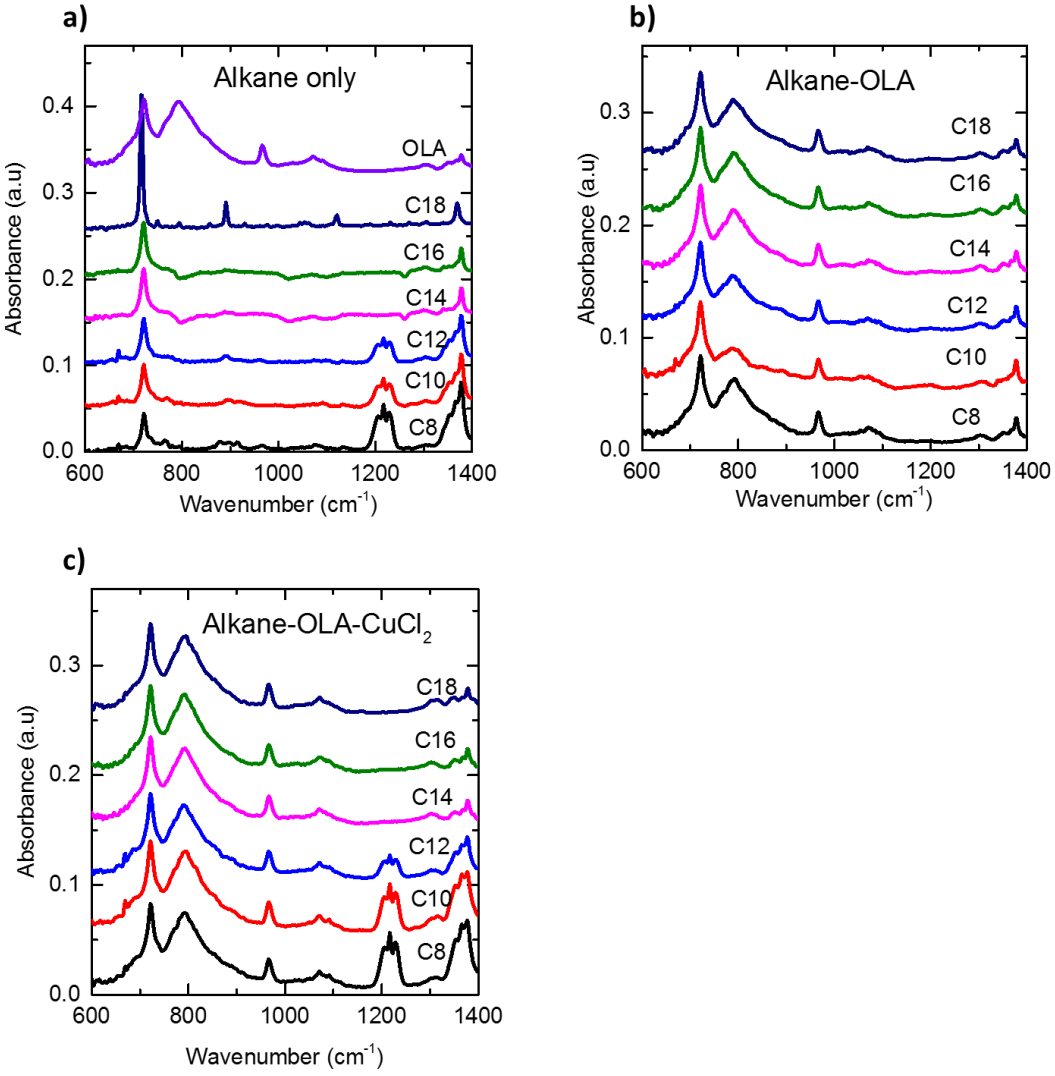

Figure 34. Plots of the FTIR spectra for different sizes of alkyl chains of a) pure alkanes, b) alkanes-OLA mixtures and c) alkanes-OLA-$CuCl_2$ mixtures in the 600 cm^{-1}- 1400 cm^{-1} region.

4.3.3.1 *Alkane only*

In the case of alkanes, fewer peaks are seen in the 600 cm^{-1} – 1400 cm^{-1} region as shown in Figure 34)a). A 860 cm^{-1} peak is observed for C18, a C-C peak at 720 cm^{-1} and for shorter ligand a broad peak at 1200 cm^{-1}. It is interesting to observe that the C18 FTIR spectra looks different than the other alkane chains with the presence of more defined peaks. A peak at 780 cm^{-1} appears for longer chains and looks broader for C14 and C16 along with a new broad and weak peak at 1150 cm^{-1}. The shoulder at 780 cm^{-1} disappears for C18 and the broad peak looks sharper but still weaker.

4.3.3.2 *Alkane-OLA interaction*

The mixture of OLA and different alkyl chain lengths of alkane shows that both features of the OLA and the alkane are found in the FTIR spectra in Figure 34)b). Interestingly, it appears that no change in intensity occurs for the OLA and C-C peaks. This is very different from the alkene chain length study where the addition of OLA leads to a decrease of the OLA N-H peak, thus confirming that ODE and OLA interact through the double bond of ODE. However, one peak in the C-N region, at 1370 cm^{-1} decreases with an increase of the alkyl chain length. In addition to that, the broad peak at 1200 cm^{-1} disappears for C8, C10 and C12 suggesting that the addition of the alkane still influences the reactivity between OLA and the Cu precursor and the shorter the alkyl length the bigger the influence.

4.3.3.3 *Alkane-OLA-$CuCl_2$ interaction*

Very small differences are observed with the addition of the Cu precursor as shown in Figure 34)c). The OLA N-H peak intensity is reduced for all peaks. However, this reduction is more visible for middle length alkyl chains such as C10 and C12. This is a very surprising result knowing that the presence of the C10 alkane gives a very poor NW aspect ratio while the addition of the C12 alkane produces NW with very high aspect ratio.

If I compare these results with the previous study, I can see that the absence of a double bond influences strongly the interaction with OLA. For an alkane, no interaction with OLA is possible except few hydrogen van der Waals bonds. Upon addition of the Cu precursor, I can deduce easily that for middle length alkanes, the interaction of OLA with Cu^{2+} salts, is stronger. When this interaction is important, the resulting aspect ratio of the NW is very small. When the interaction is not strong, the amount of monomer is smaller which means that less nuclei are formed. In other terms, the anisotropy of the NW is less respected since more atoms (after nucleation) will be formed and therefore it will be hard to control the elongated shape. When the interaction is too strong, more nuclei are formed but less free atoms are present. Therefore, the length of the NW will be shorter. In fact, in the presence of C10 alkane, NW with shorter lengths are observed and in the presence of C14, the NW diameter gets bigger. A middle chain length such as C12 provides a good balance between nuclei formation and NW length. Table 9 summarize the main groups bands found in the two studies.

Peak intensity	Group band
720 cm^{-1}	C-C stretch
800 cm^{-1}	N-H wag
910 cm^{-1}	=C-H bend
960 cm^{-1}	=C-H bend
990 cm^{-1}	=C-H bend out of plane
1072 cm^{-1}	-C-N stretch
1150 cm^{-1}	-C-N stretch
1210 cm^{-1}	-C-N stretch
1400 cm^{-1}	-C-H bend

Table 9. Main representative peaks intensity and allocated group band found in both alkene and alkane studies.

However, if I compare these results with the results obtained with the alkenes, I can observe that the alkenes are more effective than the alkanes in modifying the reactivity of the ligand with the precursor.

4.3.4 Summary of the alkane-alkene study

I have shown that the size of the alkyl chain has a strong influence on the final length and diameter of the NW. The FTIR spectra have shown that this influence is happening during the pre-nucleation stage of the NW synthesis. In fact, before the nucleation, the non-coordinating solvent tunes the reactivity of the OLA binding with the Cu precursor. When this binding is too strong the monomer reactivity is high: more nuclei but less post-nucleation atoms are formed. Therefore, the NW end up with a larger diameter. When the binding is weak, less nuclei but more atoms are formed, therefore the NW have a

shorter diameter and a shorter length. A trade-off is to take middle length alkane and alkene that contribute to the formation of thinner NW. This observation is very surprising because even though many have reported that the alkyl chain of the ligand has an influence and that the addition of a non-coordinating solvent can tune the reactivity of the monomer by diluting the ligand, no-one has clearly shown in which terms the non-coordinating solvent has an influence on this reactivity and that this reactivity can be tuned using different sizes of alkyl chains. The effect of the double bond has been evidenced as well, where alkenes give better results than alkane in terms of NW size. I have also demonstrated that the double bond and the NH bond of the OLA interact together. This interaction is important because it helps to tune the reactivity of the monomer. Therefore, longer alkenes are more suitable for this system because the reactivity is lower.

4.4 Conclusion

I have shown that by simply adding a non-coordinating solvent to the synthesis, the final aspect ratio of NW can be tuned depending on the ratio of this solvent to the capping ligand. By using FTIR techniques, I have demonstrated that the presence of the non-coordinating solvent tunes the monomer activity by controlling the binding force between the capping ligand, i.e. OLA and the Cu precursor. The role of the double bond has been emphasised as well: longer chains alkenes increase the aspect ratio of the NW by reducing more atoms during the nucleation phase that are later added to the wire. Therefore, the presence of the double bond is crucial for the non-

coordinating solvent to be effective. Both middle length alkanes and alkenes are also very efficient in increasing the aspect ratio because they successfully balance the reactivity of the capping ligand and the Cu precursor which leads to a decrease in NW diameter. In the following chapter, I will investigate the potential application of the NW synthesised in this chapter as TC.

5 Fabrication of CuNW TC

5.1 Introduction

Due to their wire-like structure, metallic NW are suitable candidates for TC applications. Since Cu is earth-abundant, cheap and non-toxic, CuNW are the material of choice for low-cost TC. The CuNW described in the previous chapter will be investigated as potential TC materials. I have shown that single NW are wrapped in an organic layer rendering them insulating. Therefore, a treatment is required in order to make NW conductive. It is well-known that Cu oxidises quickly especially in the nanoscale which renders the application of CuNW as TC difficult. Treatments need to be applied which require often the use of gases such as Argon or H_2. However, even the best treatments applied on these NW do not prevent them from oxidising over time. In this chapter, I will focus on different ways to improve CuNW optoelectronical performances and lifetime. CuNW films are prepared using a vacuum filtration method and, when specified, polymers are added on top of the NW mesh using a spin-coater. Pre- and post-treatments such as gas plasma and/or anneal, lactic acid etching and a combination of these treatments are also investigated and compared to each other. These techniques and treatments are chosen based on the price and ease of fabricating conductive and oxidant-resistant CuNW thin films.

5.2 TEM study of NW

5.2.1 Introduction

In this chapter, I will study different pre- and post- treatments of CuNW thin films to improve the conductivity of the films. I will investigate the effect of different plasma (either H_2/N_2 or O_2), anneal and chemical treatments on both NW shape and films optoelectronic performances, using optical and electron microscopes.

5.2.2 NW Plasma and anneal treatments

5.2.2.1 *Plasma post-treatment*

In this section, different treatments on NW thin films deposited onto a silicon nitride grid are investigated using HRTEM techniques: the effect of a 2h-anneal at 200°C under different gases (H_2/N_2 or O_2) and plasma post-treatment are studied. The TEM pictures of both non-annealed and annealed NW before and after a 10 s H_2/N_2 plasma treatment are shown in Figure 35.

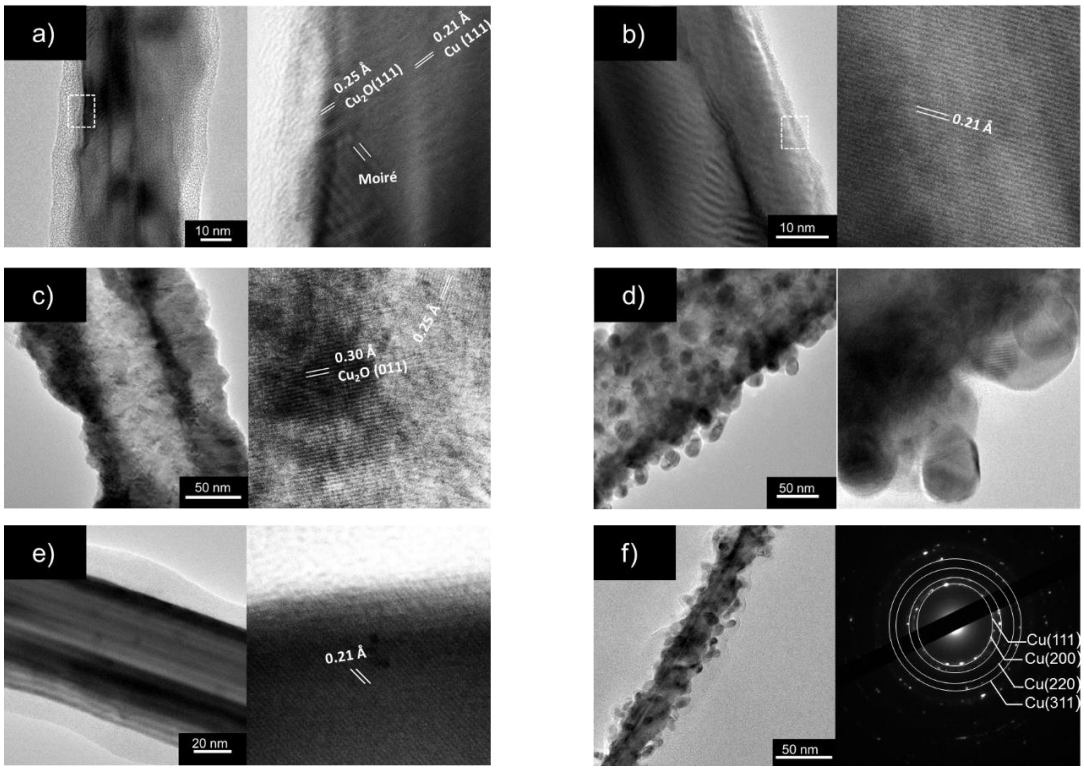

Figure 35. a) Non-treated NW (left) and zoom (right) showing the presence of both Cu and Cu_2O, b) NW after H_2/N_2 plasma treatment. and zoom on the edge (right) where only Cu is observed now, c) NW after air anneal (left), zoom in the middle where lattices of Cu_2O are observed (right), d) H_2/N_2 plasma post-treatment after air anneal (left): NW surface becomes rougher with the formation of sphere nanoparticles on the surface, zoom on one sphere (right), e) NW after H_2/N_2 anneal (left) where only Cu is present now (right) , f) H_2/N_2 plasma post-treatment after H_2/N_2 anneal creating spheres-like nanoparticles on the surface (left) and SAED pattern (right) showing the polycrystallinity of the NW and the corresponding peaks.

5.2.2.1.1 TEM of NW without treatment

A TEM picture of a NW before any treatment is shown in Figure 35)a where a thick organic layer which is made of the capping ligand used during the synthesis, is surrounding the NW. Both Cu (111) and Cu_2O (111) peaks are indexed. Moiré pattern can be identified and might be present here due to the overlapping of crystalline domains. Since the NW synthesis is kept under argon, I hypothesise that the oxide appears after the synthesis as suggested by

Meng *et al.*[59]. This oxide layer appears either during the cleaning process or during the storage of the NW in toluene.

5.2.2.1.2 TEM of NW after gas annealing

When NW are treated with different gases as shown in Figure 35)c and Figure 35)e), the morphology of NW changes: when annealed in air (Figure 35)c)), the diameter of NW increases while the edge remains roughly the same. NW composition changes with a rapid diffusion of O_2 leading to the formation of a pure Cu_2O NW as observed in previous works. When the NW is annealed in H_2 (Figure 35)e)), the diameter of the organic layer is smaller, but the NW remains in the same shape. However, no trace of Cu_2O is visible anymore on the surface showing that the annealing process is an effective method for the reduction of the copper oxide layer.

5.2.2.1.3 Effect of plasma post-treatment on non-annealed and annealed NW

A 10s H_2/N_2 plasma performed on a non-treated NW removes a significant amount of the organic layer as seen in Figure 35.b). However, when the plasma is performed after annealing in either air (Figure 35)d)) or H_2/N_2 (Figure 35)f)), NW shape becomes rougher with the apparition of spheres-like NPs on the surface leading to an increase of the surface area and therefore a significant increase of the NW roughness. The SAED pattern on the right of Figure 35)f) indicates that the NW is polycrystalline but still made of pure Cu. It is interesting to observe that the change in NW morphology occurs only

when the plasma treatment is performed after annealing and is independent of the gas chosen during annealing. When the plasma is performed on a non-treated NW, no change is observed in terms of morphology. Plasma reacts strongly with the pure material formed after annealing, i.e. pure Cu_2O for an air treatment or pure Cu wrapped in an organic layer, transforming the shape of the NW while for a non-treated NW, plasma only removes the organic layer and attacks Cu_2O, leaving the Cu part intact.

5.2.2.1.4 Effect of a post-treatment on the NW network

NW SEM pictures displayed in Figure 36)a show that before any treatment, NW are organised in bundle-like structures due to the presence of an organic layer. The Figure 36)b) of H_2/N_2 plasma treated NW confirms that no more organic layer is present. After a 2h-air anneal at 200°C (Figure 36)c)), NW increase in size but most of the NW have lost their anisotropic shape. After an H_2/N_2 anneal followed by a plasma treatment shown in Figure 36)d), NW surface is rougher and forms sphere-like particles, which confirms what has been observed in Figure 35)f). NW are also partly broken, showing that a post-plasma treatment gives very bad results in terms of cleaning the surface and keeping the anisotropy of NW intact.

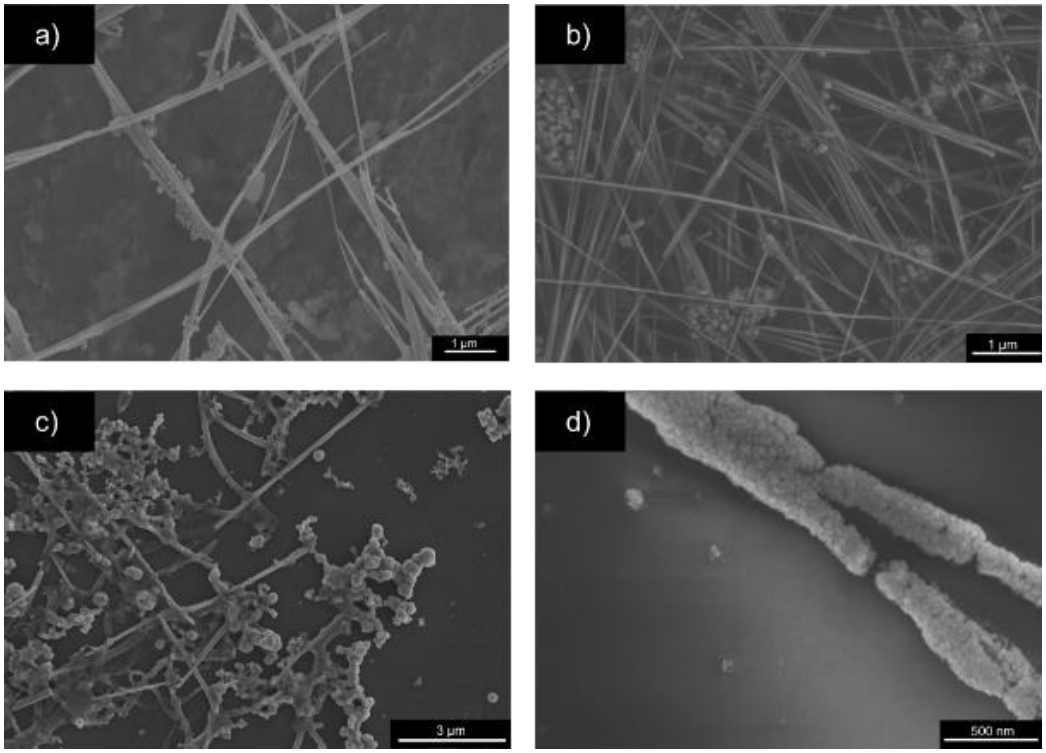

Figure 36. SEM images of a) as-synthesised CuNW organised in bundles due to the presence of an organic layer, b) NW after H_2/N_2 plasma cleared from the organic layer, c) NW after O_2 anneal and plasma, d) NW after H_2/N_2 anneal and plasma.

5.2.2.2 *Plasma pre-treatment*

Interestingly, when plasma is performed prior to annealing, NW morphology is not modified for both gases investigated here as seen in both Figure 37)a) and Figure 37)b). When the NW surface has a thick organic layer, plasma "attacks" the organic layer first and reduces the oxide layer through diffusion of the hydrogen. However, when this surface is free from an organic layer, plasma reduces primarily the oxide surface, which causes a modification of the surface morphology. It is interesting to observe that in case of a plasma post-treatment, the roughness increase is dependent on the gas used. In case of an O_2 anneal, the pure copper formed by the plasma treatment oxidises into copper (II) oxide which explains why no surface modification is observed. A

plasma performed before an H_2 anneal treatment allows the formation of a pure Cu surface where the passivation of the surface occurs via diffusion of hydrogen into the dangling bonds of copper. However, the SAED pattern in Figure 37)b) (right) shows that NW are polycrystalline and therefore I hypothesise that some changes in composition have occurred during both plasma and anneal processes. Although the TEM picture in the middle of Figure 37)b) confirms that NW are made of pure Cu, the shape of the NW (Figure 37)b) ,left) is not straight as it was before H_2 anneal. Therefore, plasma treatment leaves NW in a "weaker" shape to undergo any further treatment.

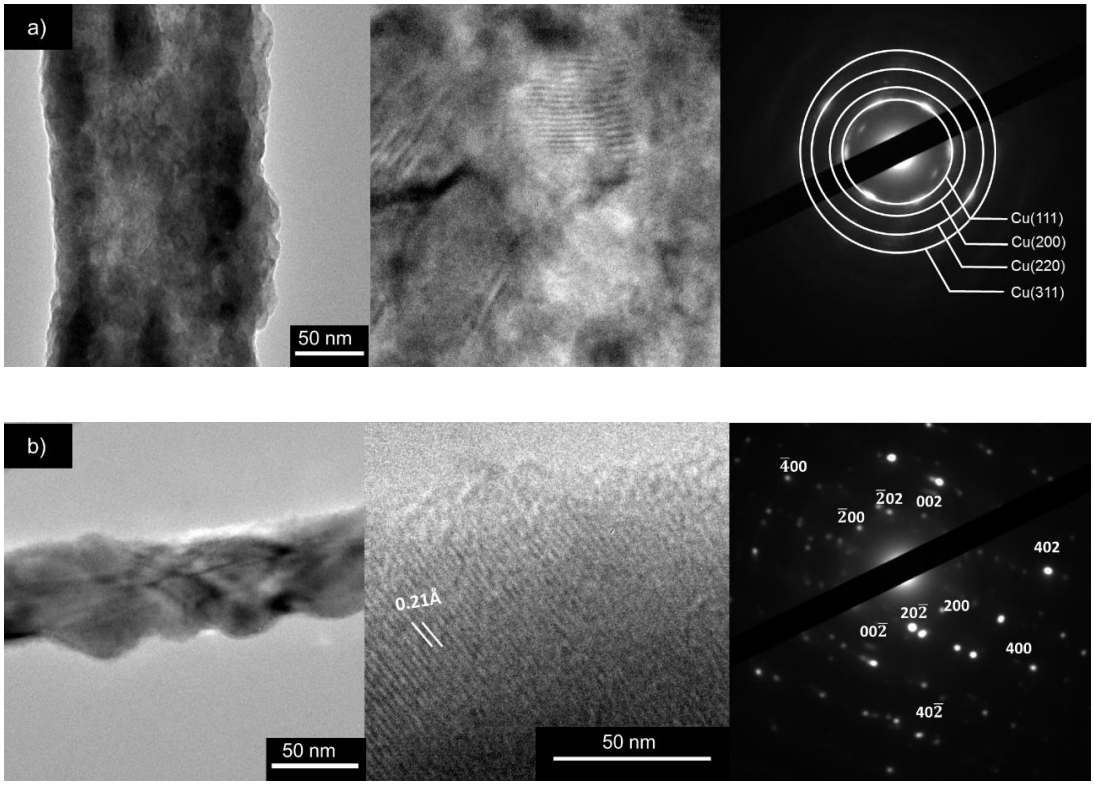

Figure 37. a) NW after plasma and O_2 anneal (left), zoom in the middle of the wire (middle) and SAED pattern (right) showing that the NW is made of Cu_2O. b) NW after plasma and H_2/N_2 anneal treatments showing that although the surface becomes slightly rougher (left), the NW is made of pure Cu (middle) but the SAED pattern suggests that the NW is polycrystalline (right).

5.2.2.3 *Effect of pre- and post- treatments on the size of the NW*

Figure 38 plots the evolution of the average NW diameter (taken for 5 NW each) depending on the post-treatment strategy chosen. A general trend is that O_2 anneal produces NW with larger diameter due to the formation of the denser Cu_2O with an average diameter passing from 42 nm to 160 nm for both an O_2 anneal and plasma and O_2 anneal and to 180 nm when plasma is performed before O_2 anneal. Hydrogen treatment gives more heterogeneous results: a single annealing treatment reduces slightly the diameter from 85 nm to 80 nm, a plasma post-treatment increases the surface of NW up to 115 nm. A plasma pre-treatment followed by an H_2/N_2 anneal decreases the diameter of the NW to 35 nm due to the removal of both oxide and organic layer while a plasma without any annealing treatment reduces the diameter up to 50 nm. This confirms my previous hypothesis: an H_2/N_2 treatment after plasma helps the diffusion of hydrogen which passivates dangling bonds and further reduces remaining oxide left which explains the decrease in size [27].

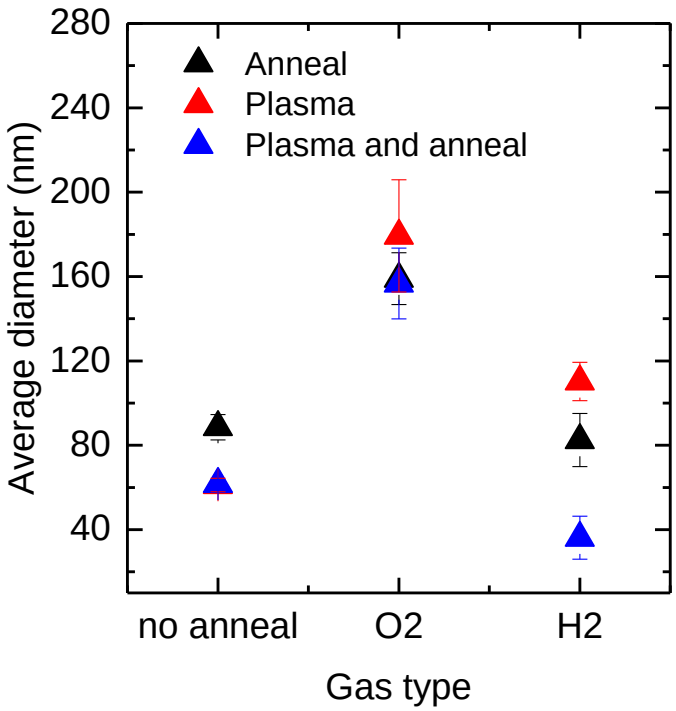

Figure 38. Plot of the average diameter of NW for different treatments (anneal and/or plasma or no anneal) according to the gas chosen (H_2/N_2 or O_2).

A summary of the different treatments effect on NW studied in this section is given in Table 10.

Treatment	Diameter	Roughness	Presence of an organic layer	NW composition
No treatment		No	Yes	Cu and Cu_2O
H_2/N_2 anneal	No effect	No effect	Yes	Cu
O_2 anneal	Increases	Increases	No	Cu_2O
H_2/N_2 plasma	Decreases	Minor	Minor	Cu
O_2 anneal and post-H_2/N_2 plasma	Increases	Increases	No	Cu_2O?
H_2/N_2 anneal and post-H_2/N_2 plasma	Decreases	Increases	Yes	Cu
Pre-H_2/N_2 plasma and O_2 anneal	Increases	Increases	No	Cu_2O
Pre-H_2/N_2 plasma and H_2/N_2 anneal	Decreases	Increases	No	Cu

Table 10. Effect of anneal and/or plasma treatments on NW diameter, roughness, organic layer and nature. A non-treated NW is shown as a reference.

5.2.2.4 *Optoelectronic properties*

A H_2/N_2 plasma pre-treatment effect on the sheet resistance for different thin films annealed at 200 °C for 2h under a flow of H_2/N_2 are shown in Figure 39.

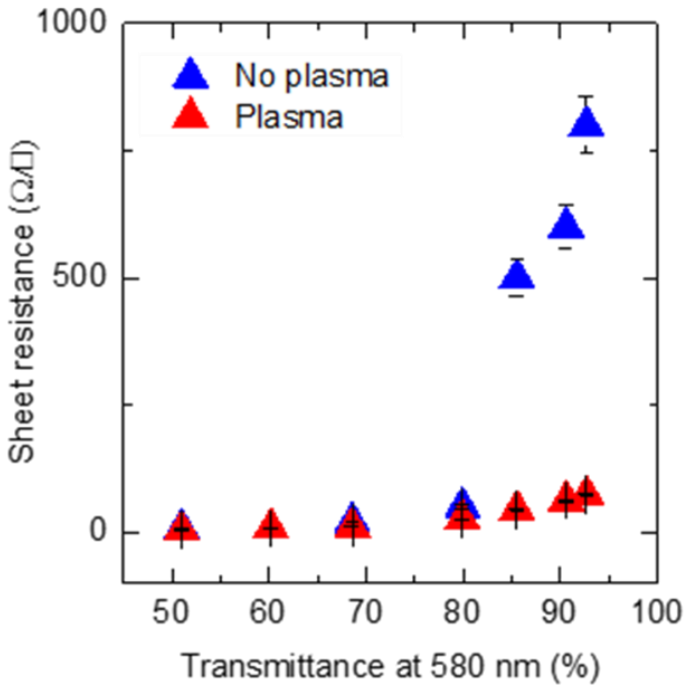

Figure 39. Plot of the sheet resistance of H_2/N_2 annealed thin films with and without plasma treatment according to the transmittance of the film.

Non-plasma treated NW have a higher sheet resistance than H_2/N_2 plasma treated NW. This is more visible for more transparent films: for a 79 % transmittance film, the sheet resistance passes from 60 Ω/□ to 50 Ω/□ and for a 93% transmittance film, NW exhibit a sheet resistance of 980 Ω/□ while a plasma treatment drops this value to 90 Ω/□. The plasma treatment is clearly necessary in order to improve the electrical performances of thin films.

5.2.3 NW chemical treatment

In the previous section, I have shown that a plasma treatment is the most effective way of removing both oxide and organic layer while a post H_2/N_2 anneal step creates a passivated CuNW surface. However, I have also shown that this treatment results in the formation of polycrystalline NW with a "damaged" surface. In this section, I investigate the use of a mild lactic acid treatment that has been first developed by Won *et al.* [165] to replace the plasma treatment. Lactic acid is chosen because it is a liquid that does not leave any residues unlike ascorbic acid for instance. It has a high viscosity which helps cleaning the surface of the NW without damaging them.

5.2.3.1 *Lactic acid/OLA interaction*

To understand the effect of lactic acid on OLA, the interaction between the two chemicals is studied using FTIR. Spectra of lactic acid, OLA and a 1:1 OLA: lactic acid mixture are shown in Figure 40 . It is observed that the addition of lactic acid to OLA leads to the disappearance of the OLA peaks such as the N-H peak at 800 cm^{-1} and are replaced with lactic acid peaks such as the C-H bend at 820 cm^{-1}, the C-O stretch at 1220 cm^{-1}, the C=O stretch at 1680 cm^{-1}. From this observation, it can be deduced that when lactic acid is added in excess to OLA-wrapped CuNW, it dissolves completely OLA while the remaining molecules are chemisorbed to the now pure CuNW.

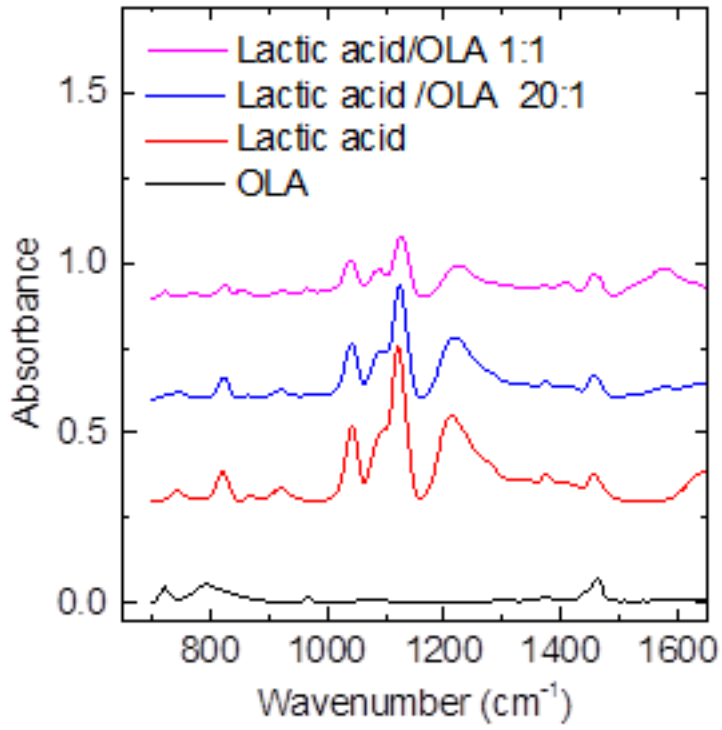

Figure 40. FTIR of lactic acid, OLA and lactic acid/OLA mixtures for both 1:1 and 20:1 ratio.

5.2.3.2 *Lactic acid effect on CuNW*

Figure 41 shows the HRTEM of an OLA-wrapped single CuNW after a 30s-lactic acid treatment. The NW is cleared from most of the organic layer and all the oxide. The morphology of the NW remains the same and the lattice at the edge of the wire corresponds to pure Cu, thus confirming that the copper oxide has been removed by the lactic acid treatment.

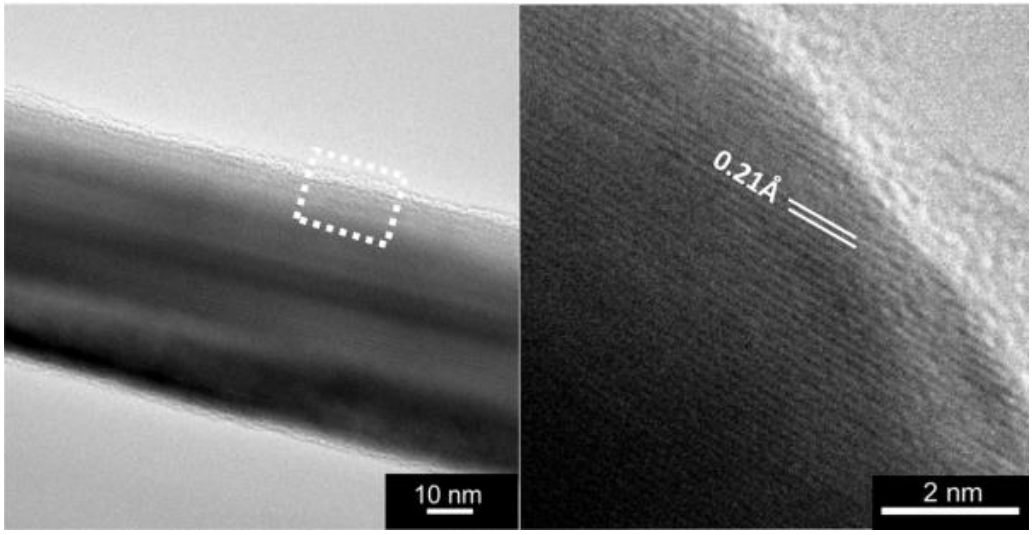

Figure 41. HRTEM images of a) a NW after a 30s-lactic acid treatment, b) a zoom on the NW showing that the edge is formed only of pure copper.

Figure 42 shows the FTIR spectra of CuNW before and after a lactic acid treatment. Before the treatment, few characteristic peaks of OLA and ODE are visible such as the ODE 910 cm^{-1} C=C stretch and the OLA 800 cm^{-1} N-H stretch peaks. After the treatment, the peaks are not seen any more suggesting that a large proportion of the organic layer is gone.

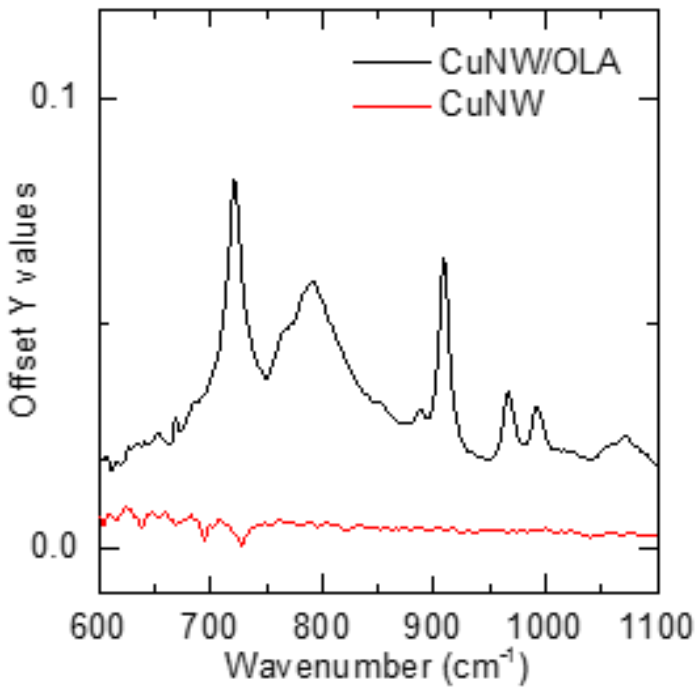

Figure 42. Plot of the FTIR spectra of NW before and after lactic acid treatment.

After a 2h H_2/N_2 annealing, NW are still made of pure Cu. The roughness increases slightly with the formation of small drop-like spheres on the surface as shown in Figure 43. It is interesting to observe that an annealing performed on the surface of a lactic acid-treated NW does not increase the NW roughness as much as for a H_2/N_2 annealing on a plasma-treated NW as shown in Figure 37)b) in paragraph 5.2.2.2. Therefore, I can confirm that NW roughness increase is due to the plasma treatment. Lactic acid treatment is a milder treatment for removing both organic traces and oxides while plasma reacts strongly with either the oxide or organic layer which modifies significantly CuNW surface morphology.

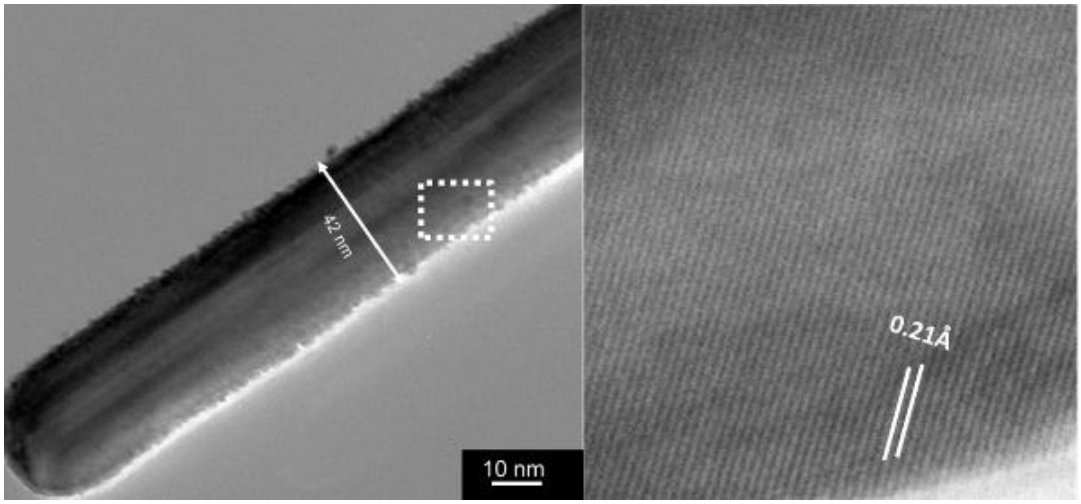

Figure 43. HRTEM of an acid-treated NW after 2h annealing (left), zoom on the edge (right).

5.3 Optoelectronic properties of CuNW films

5.3.1 Study on the effect of different treatments on CuNW thin films

5.3.1.1 *Optical and electrical studies*

This section investigates the evolution of the optoelectronic properties for both lactic acid-treated Cu NW and lactic acid/H_2/N_2 annealed Cu NW.

5.3.1.2 *Surface study*

NW film thickness is an important parameter as it controls both the conductivity and the transparency of the films. The film thickness is measured using a dektak following a methodology described in paragraph 3.3.9. Figure 44 plots the surface profile of different NW thicknesses according to the volume of NW filtered.

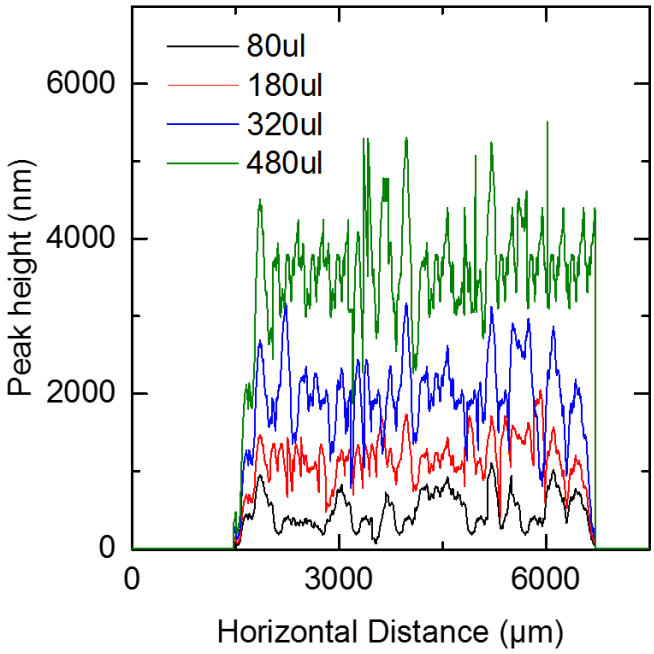

Figure 44. Surface profile of CuNW according to the volume of NW filtered.

Figure 45)a) plots the NW volume required for obtaining a given CuNW film thickness while Figure 45)b) plots the relationship between the transmittance of the film and their corresponding thickness where it can be seen that the thinner the thin film, the more transparent it is.

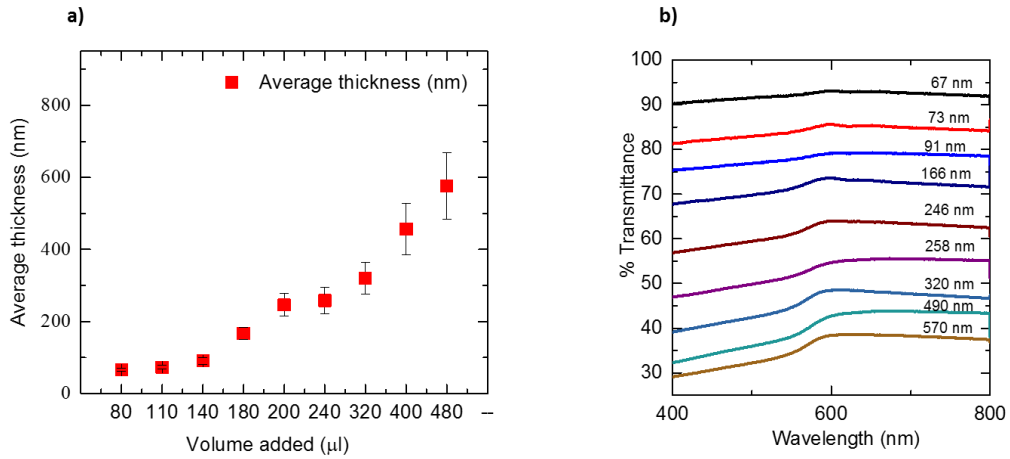

Figure 45. a) Plot of the evolution of NW thin film thickness according to the volume of NW dropped using a pipette, b) Plot of the evolution of NW transmittance in the 400nm-800nm region for different film thicknesses.

MicroXam images for different NW film thicknesses are shown in Figure 46. For thicker films, the number of NW per area is higher than for thinner films. The overlapping of NW increases as well with the thickness which increases the total roughness of the film.

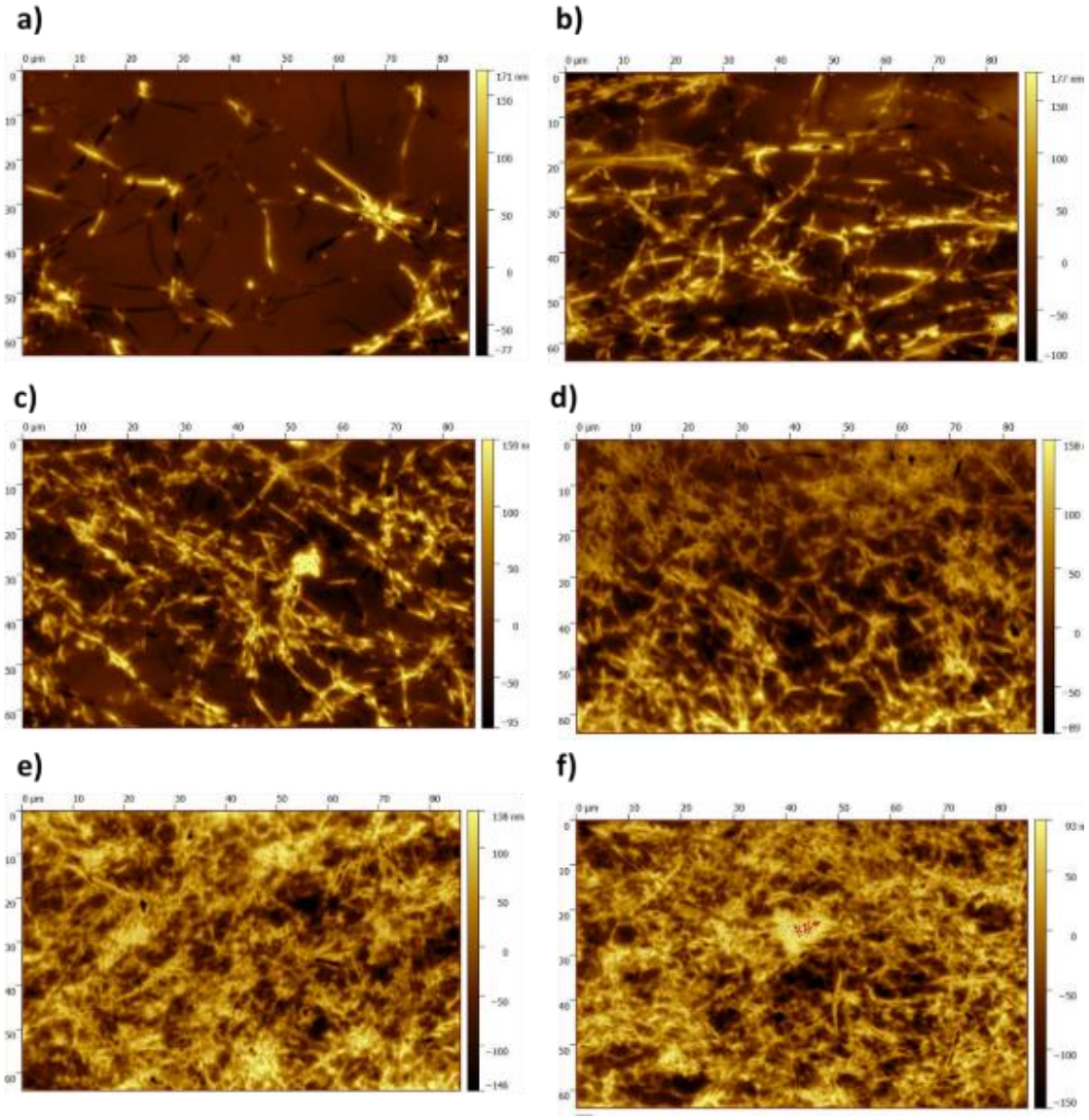

Figure 46. MicroXam images for a) 70 nm, b) 90nm c) 166 nm, d) 246 nm, e) 320 nm, f) 490 nm- CuNW thin films.

5.3.2 Anneal treatment effect

The resistivity of a lactic acid-treated thin film before and after a 2h-anneal treatment is measured for different transmittances, and plotted in Figure 47. Thin films possess excellent properties exhibiting a sheet resistance of 51 Ω/□ before annealing and 43 Ω/□ after annealing for a 93% transmittance. For a 60% transmittance, the sheet resistance passes from 22 Ω/□ before annealing to 6 Ω/□ after annealing. Therefore, 2h of annealing helps to reduce the contact resistance in the junction between two NW by fusing them. For thicker films, the NW network reaches the conductivity limit of Cu and therefore fewer differences are observed between non-annealed and annealed films.

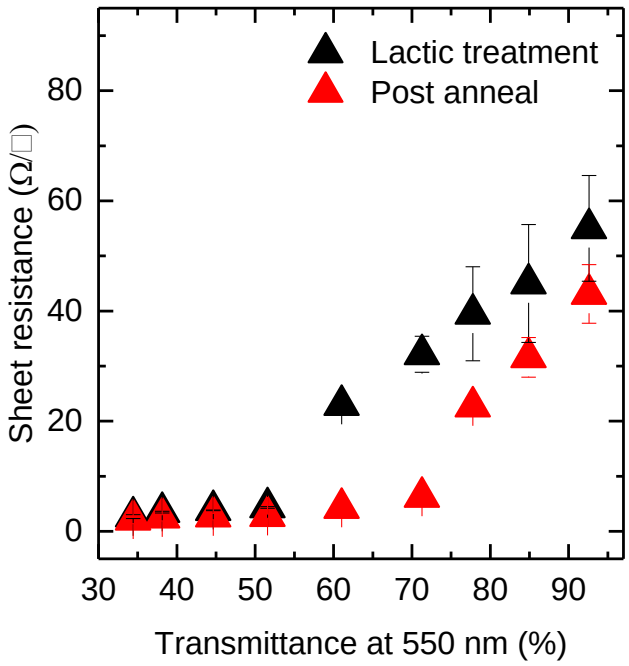

Figure 47. Sheet resistance vs transmittance before and after a 2h anneal treatment for lactic acid treated NW thin films.

Pictures of post-annealed NW films of different thicknesses are represented in Figure 48 with the corresponding transmittance and sheet resistance measured. A summary of the thickness, transmittance and sheet resistance measured before and after annealing for lactic acid-treated NW is shown in Table 11.

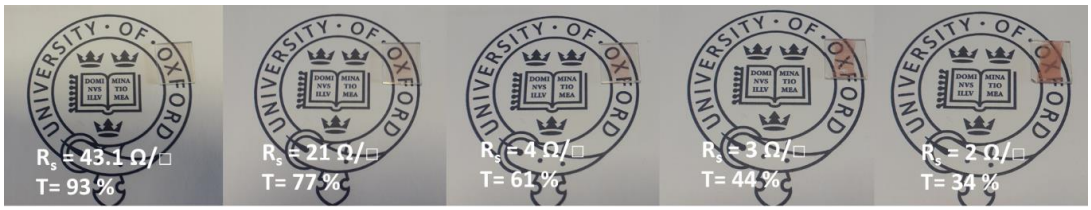

Figure 48. Photographs of CuNW thin films for different thicknesses showing that the thicker the film, the more conductive but less transparent it is.

Transmittance at 550 nm (%)	Thickness (nm)	R_s (Ω/□) before annealing	R_s (Ω/□) after annealing
93	67	55	43.1
85	73	45	31
77	91	39.5	23
71	166	32	6.2
61	246	23	4.2
51	258	4.3	2.7
44	320	3.8	2.6
38	490	3.5	2.5
34	570	2.6	2

Table 11. Summary of thin films thickness and R_s before and after annealing for different transmittances.

5.4 Oxidation of the NW

5.4.1 Effect on the electrical properties of the film

NW thin films oxidise very quickly, forming an outer copper oxide layer that will increase through O_2 diffusion across the NW. The formation of this oxide can be considered as an insulating layer that decreases the R_s. Figure 49 plots the R_s vs the transmittance over time. For a 60% transmittance, R_s passes from 35 Ω/□ to 38 Ω/□ after 3h to 43 Ω/□ after 16 h in air. For 93% transmittance, R_s passes from 43 Ω/□ to 78 Ω/□ after 3h to 95 Ω/□ after 16h. For thin films, since fewer NW are overlapping, the oxidation process is more likely to have more effect on the increase of the sheet resistance. After 70 days stored in air, thin films below 100 nm are not conductive anymore while thicker films (above 250 nm) are conductive up to 250 days. The oxidation of the films can be seen by a change of colour of the layers passing from salmon, to dark grey (Cu_2O) and to yellow green (formation of CuO).

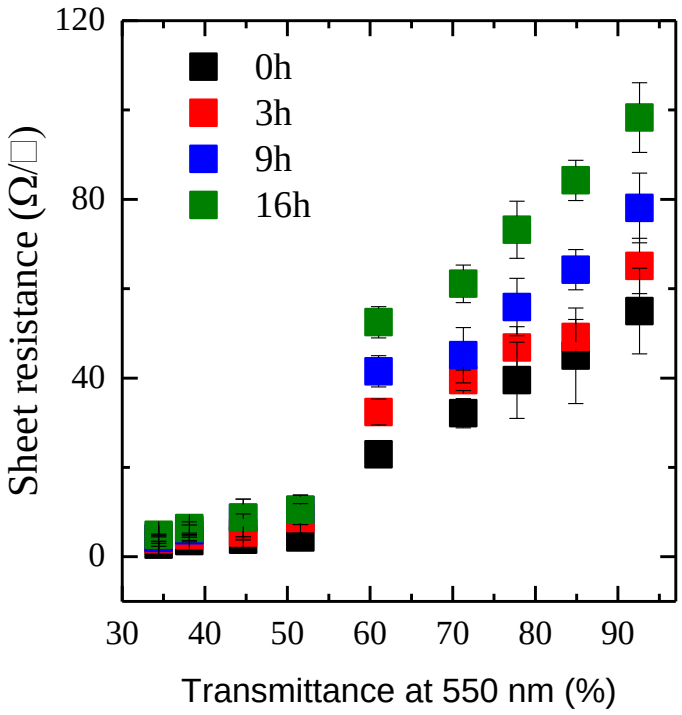

Figure 49. Plot of the sheet resistance vs transmittance for CuNW thin films after 0h, 3h, 9h and 16h left in air.

The oxidation of NW is intrinsic to copper properties. The oxidation rate is even amplified for nanostructures such as NW. In order to prevent the oxidation, the addition of a coating layer on top of NW is studied. Spin coating can produce very smooth and homogeneous thin films and therefore will be the chosen method for the fabrication of CuNW/ top layer composites as described in 3.2.4.

5.4.2 NW/top layer fabrication

ZnO, Polystyrene, PVP, ethylcellulose, PEDOT: PSS are investigated as top layers. PVP is widely used as a polymer in AgNW and CuNW synthesis [31,96,183] and has good affinity with p-type metals. Ethylcellulose and surface-modified ethylcellulose are known as film maker producing very smooth films [184,185].

PEDOT:PSS [186,187] and ZnO [188,189] are both used in the fabrication of Quantum Dots solar cells as p-type and n-type respectively. They are also good smoothing layer that contribute to reduce the roughness of the film. Polystyrene is a hydrophobic film maker commonly used in packaging [190,191].

5.4.2.1 *Top layer characterisation*

The roughness of the thin films made without NW after drying is shown in Figure 50. Ethylcellulose, ZnO and PVP MicroXam pictures show the formation of voids on the surface. PEDOT: PSS has few voids, but the thin film is very smooth compared to the three other materials. Ethylcellulose is smoother compared to ZnO and PVP. Voids are due to the presence of trapped air in the solution. The rotation movement of the spin coating lifts the trapped air on the surface forming "holes". Ethylcellulose dissolves in toluene, while ZnO and PVP are dissolved in chloroform and water respectively, two polar solvents. It is well known that polar solvents can solubilise more oxygen than non-polar solvents such as toluene [192], therefore they are more likely to form voids. For polystyrene, cracks are seen on the surface. Polystyrene is a "glassy" plastic that undergoes some fractures initiated by flaws. These fractures are clearly shown in Figure 50)d).

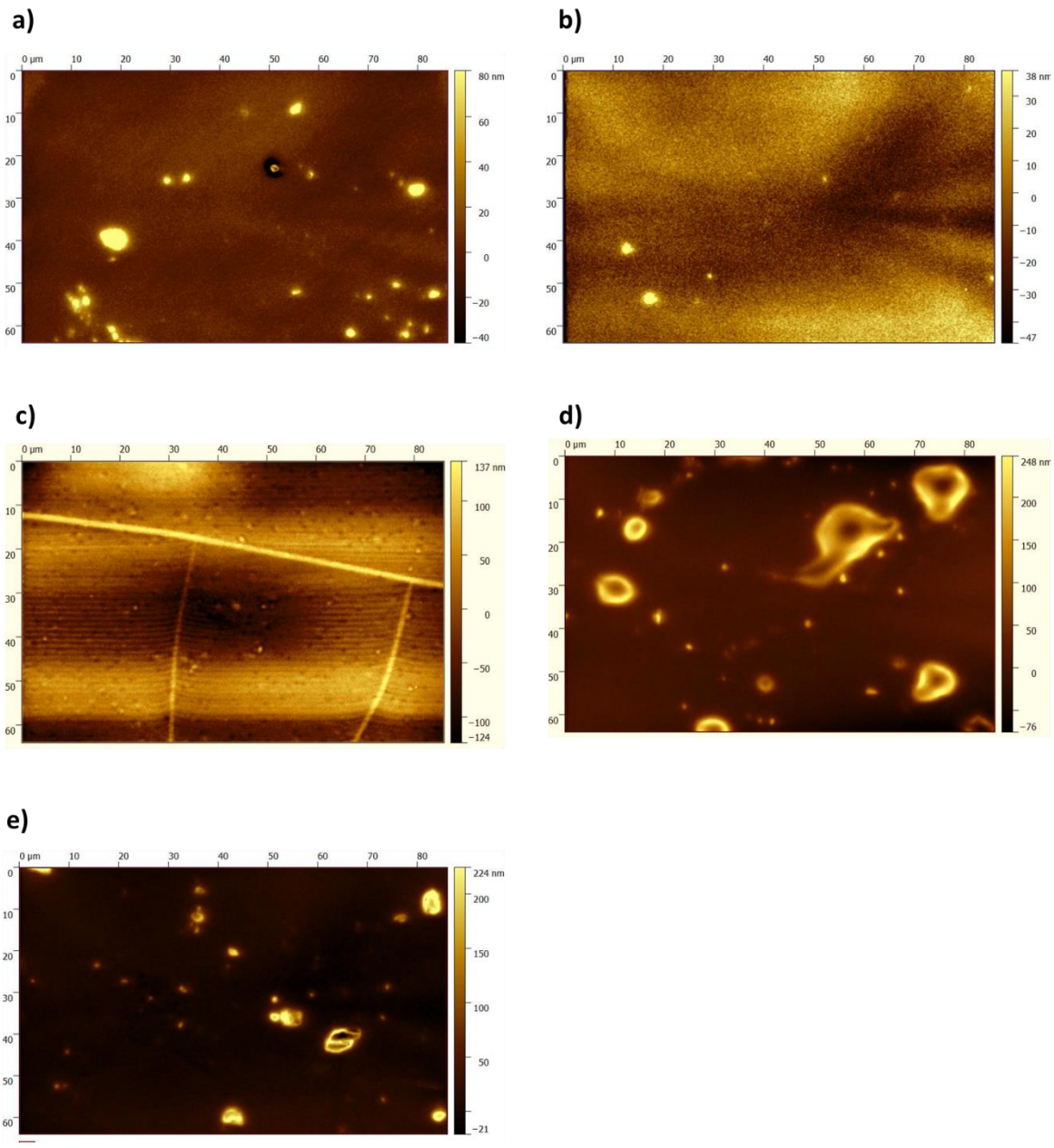

Figure 50. MicroXam confocal images of a) ethylcellulose, b) PEDOT: PSS, c) PVP, d) Polystyrene and e) ZnO spun coat thin films.

The graph in Figure 51 plots the surface roughness measured using MicroXam of the different smoothing layers. The values confirm what has been observed in Figure 50: PEDOT: PSS has the lowest averaged roughness surface (8 nm) while polystyrene has the highest roughness value of 32 nm. ZnO and ethlycellulose possess a roughness values of 17 nm and 14 nm respectively.

Therefore, from the observation, PEDOT: PSS possesses the best properties as a top layer followed by ethylcellulose and ZnO while polystyrene and PVP are less suitable for such applications.

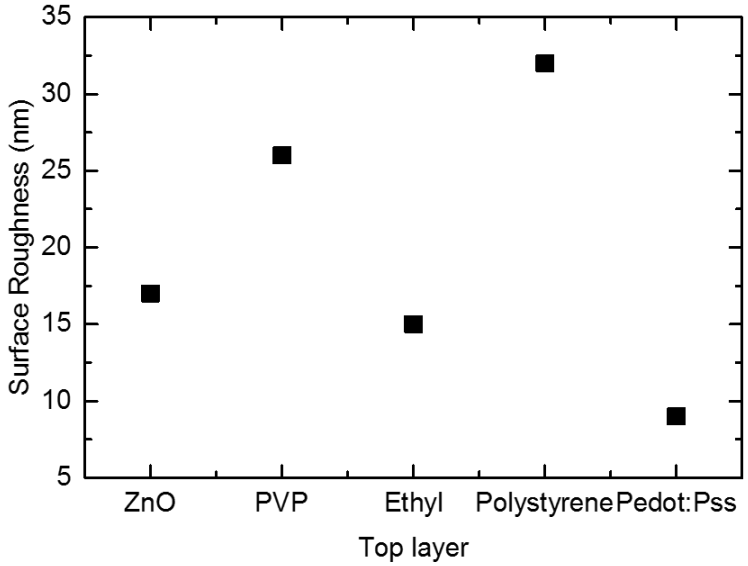

Figure 51. Surface roughness values for ZnO, PVP, Ethylcellulose, Polystyrene and PEDOT: PSS films.

5.4.2.2 *CuNW/ top layer films characterisation*

Confocal images of 90 nm thick NW film composites prepared using the polymers mentioned previously are shown on the left of Figure 52. Ethylcellulose and ZnO cover NW quite well while polystyrene and PVP cover them partially. NW are not visible anymore when covered by PEDOT: PSS. The difference of coverage between ethylcellulose, ZnO on one hand and Polystyrene and PVP can be explained by a difference of power of adhesion between the polymers and ZnO and CuNW. In fact, ethylcellulose has O-H bonds that can form Van der Waals interaction with CuNW while ZnO is highly polar and can form such bonds as well. Polystyrene is a hydrophobic polymer

and therefore the interaction with CuNW is poor. PVP has a good affinity with Cu but the roughness of CuNW/PVP film is the highest. It might be due to the fact that the spin coating of an aqueous PVP solution creates a rough surface that is enhanced on top of a CuNW mesh.

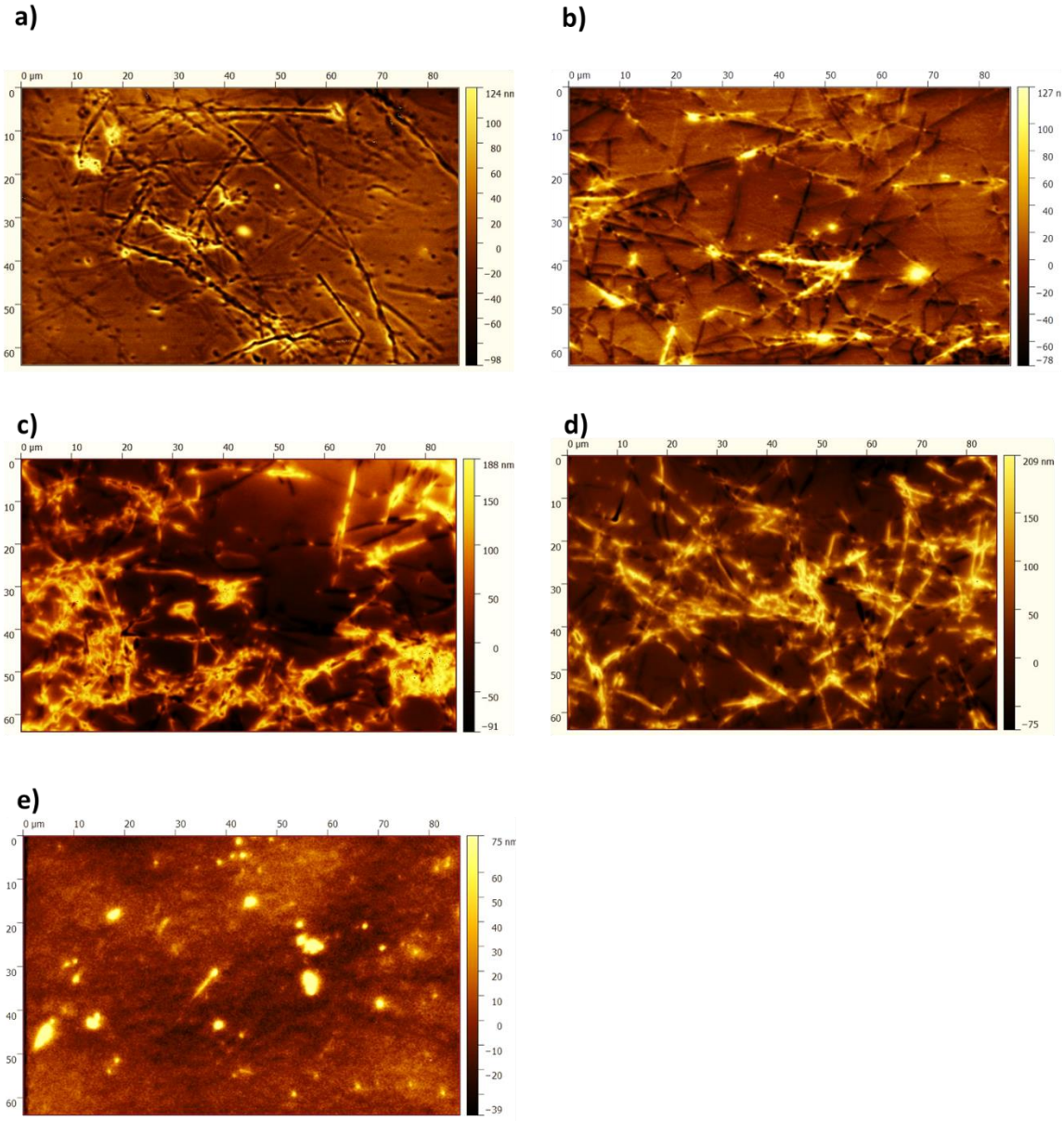

Figure 52. MicroXam confocal images of CuNW films with a) ethylcellulose, b) ZnO, c) PVP, d) polystyrene and e) PEDOT: PSS as a top layer.

The transmittance and reflectance are shown in Figure 53 for the different samples with and without CuNW. Without NW, the transmittance of the films is very high, reaching almost 100% for ZnO which is followed by ethylcellulose and PVP both reaching 93% and 89% at 580 nm respectively. On top of a 90 nm CuNW thin film, the transmittance of the film decreases. For instance, the transmittance of a CuNW/ZnO film is at 79% which is similar to the transmittance of CuNW film standing on their own and the transmittance of CuNW/ethylcellulose decreases up to 76%. For CuNW/polystyrene and CuNW/PVP films, it is observed that the transmittance decreases significantly (62% and 67% respectively at 580nm) and CuNW/PEDOT: PSS transmittance spectrum appears to be unusually low. Therefore, in terms of transmittance, ZnO and ethylcellulose are excellent candidates as top layers for CuNW TC: ZnO as a top layer does not modify the optical properties of CuNW films while the addition of an ethylcellulose coating layer decreases the transmittance to only 5% of its original value.

The reflectance of the different films is also measured. The reflectance of the different polymers and ZnO is relatively low (below 12% in the 500nm -700 nm region) as seen in Figure 53)b). When they are on top of a CuNW thin film (Figure 53)e)), the reflectance increases for all the polymers except for PEDOT: PSS: it slightly increases reaching 12% for ZnO films at 580 nm while it increases for PVP and ethylcellulose films. The reflectance of the CuNW/top layer is however relatively low suggesting that all the top layers are compatible with TC applications. The MicroXam images in Figure 52)e have shown that almost no NW were visible upon addition of a PEDOT: PSS layer. This suggests that PEDOT: PSS has reacted with the NW: the reflectance of

CuNW/ PEDOT: PSS film does not show any more a SPR peak between 550 nm to 580 nm suggesting that no more NW are present. PEDOT: PSS has an acidic nature that can decompose the NW which is what might be observed here.

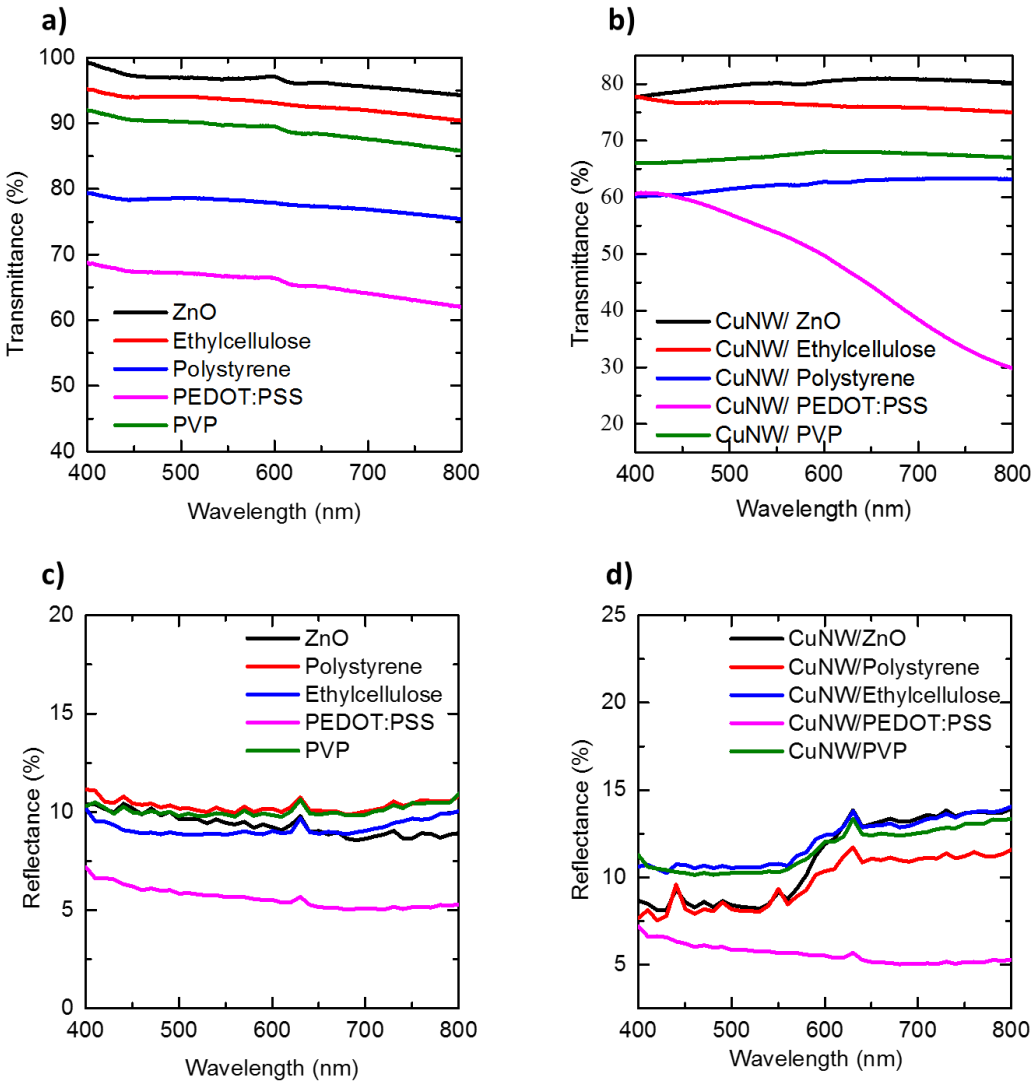

Figure 53. Transmittance (a and b), and reflectance (c and d) of ZnO, Ethylcellulose, Polystyrene, PEDOT: PSS and PVP on their own (a and c) and on top of a Cu NW thin film (b and d).

Measurement of the sheet resistance depending on the top layer nature is shown in Figure 54a) and the averaged surface roughness of the films is displayed in Figure 54)b). The CuNW/PEDOT: PSS film is not shown because

the conductivity could not be measured, further confirming that PEDOT: PSS has reacted with CuNW and eventually broke the network.

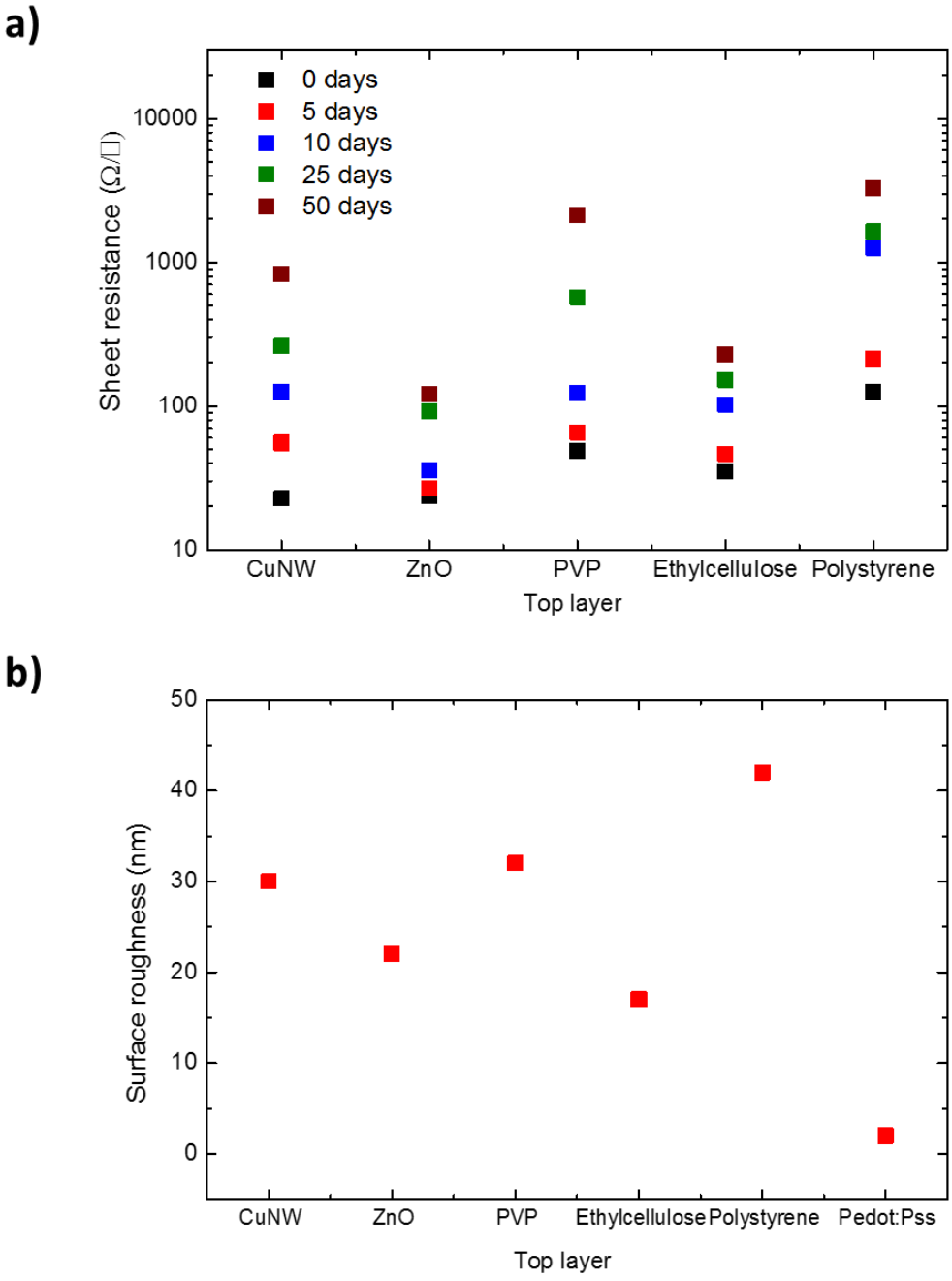

Figure 54. a) Sheet resistance measured after 0, 5, 10, 25 and 50 days, b) surface roughness of CuNW/Top layer films.

Figure 54)a) shows that adding ZnO or ethylcellulose on top of CuNW gives the best results in terms of NW stability and surface roughness. CuNW film have an initial sheet resistance of 22.6 Ω/□. From day 0 to day 50, R_s of a CuNW/ZnO passes from 23.8 Ω/□ to 121 Ω/□, while R_s passes from 35.2 Ω/□ to 121.3 Ω/ for CuNW/ethylcellulose films. For polystyrene/ CuNW films, R_s jumps from 125.3 Ω/□ to 3263 Ω/□ and for CuNW/PVP films, it passes from 48 Ω/□ to 2180 Ω/□. Therefore, the addition of a coating on top of CuNW creates a great disparity in NW stability depending on its nature. R_s increases up to 100 Ω/□ for polystyrene while adding layer of ZnO increases the sheet resistance of only 1 Ω/□. The roughness of the films is shown in Figure 54)b. The addition of ethylcellulose and ZnO decreases significantly the roughness of NW films passing from 30 nm to 17 nm and 22 nm respectively while PVP and polystyrene layers increase it to 32 nm and 42 nm respectively. A summary of the roughness and R_s for Day 0 and Day 50 is given in Table 12

Film	Surface Roughness (nm)	R_s (Ω/□) Day 0	R_s (Ω/□) Day 50
CuNW	32	22.65	832
CuNW/ZnO	22	23	121
CuNW/PVP	32	49	2136
CuNW/Ethylcellulose	17	35	229
CuNW/Polystyrene	45	125.2	3263.2
CuNW/PEDOT:PSS	2	x	x

Table 12. Summary of the roughness and the evolution of the R_s from day 0 to day 50 for the different coatings studied in Figure 54.

Therefore, I can conclude that a good NW coverage prevents NW from oxidising. Polystyrene and PVP do not prevent NW oxidation and they seem to encourage this oxidation by diffusing more oxygen into the CuNW film. ZnO appears to be the best candidate as it protects NW from oxidation for many days while keeping the same optical properties of the film. However, the roughness of the CuNW/ZnO films remain high (superior to 20 nm). Therefore, in the next section, I will investigate the effect of addition of between 1 to 5 layers of ZnO on the optoelectronic performances and morphology of the films.

5.4.2.3 *CuNW/ ZnO layer(s) TC films study*

Like in the previous section, 90 nm CuNW thin films are considered. Between 1 to 5 layers of ZnO are added on top of the NW network by spin coating. The transmittance of the thin film in Figure 55)a) shows that it decreases slightly with further addition of ZnO layers passing from 79% for 1 ZnO layer added to 71% for 5 layers of ZnO (measurements taken at 580 nm). Therefore, ZnO is very good to retain the transmittance of the NW films even with the addition of 5 layers. The reflectance increases with the layers of ZnO added but remains below 15%. Therefore, in terms of optical performances, the CuNW/ZnO layer(s) films exhibit excellent properties.

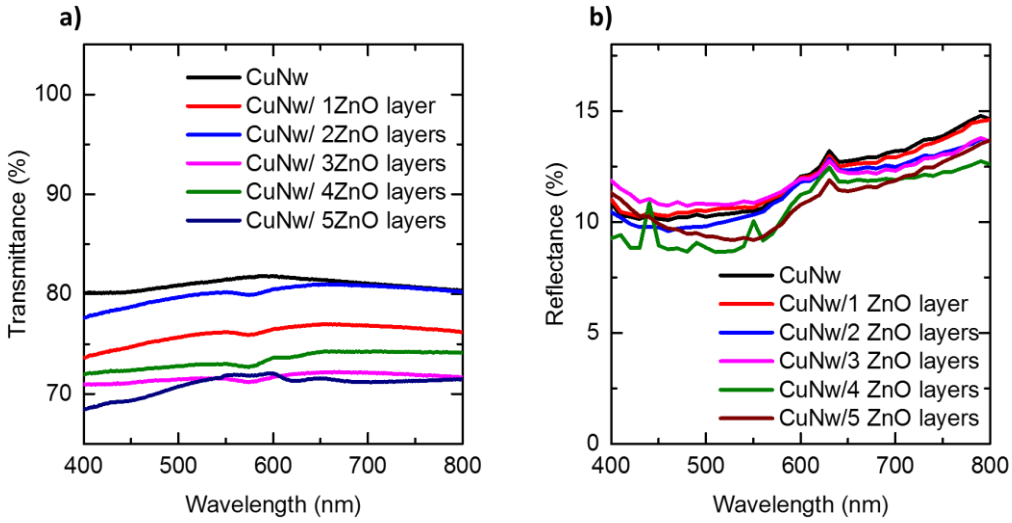

Figure 55. a) Transmittance and b) reflectance of CuNW films with 0 to 5 ZnO top layer(s).

The electrical conductivity of the different films is plotted in Figure 56)a) and a CuNW thin film is used as a reference. R_s of the films increases with the amount of ZnO layers added passing from 22 Ω/□ for a single CuNW film, 26 Ω/□ for a CuNW/ 2ZnO layers film and 34 Ω/□ for CuNW/5ZnO thin film. Because each layer increases the thickness of the film, fewer NW will stick up on top of the film which explains the increase in the resistance of the film. The roughness measurement in Figure 56)b) shows that more layers of ZnO makes the film smoother: 5 layers of ZnO reduces the surface roughness from 32 nm to 12 nm while the addition of 1 or 2 layers of ZnO reduced the surface roughness by only 10 to 12 nm.

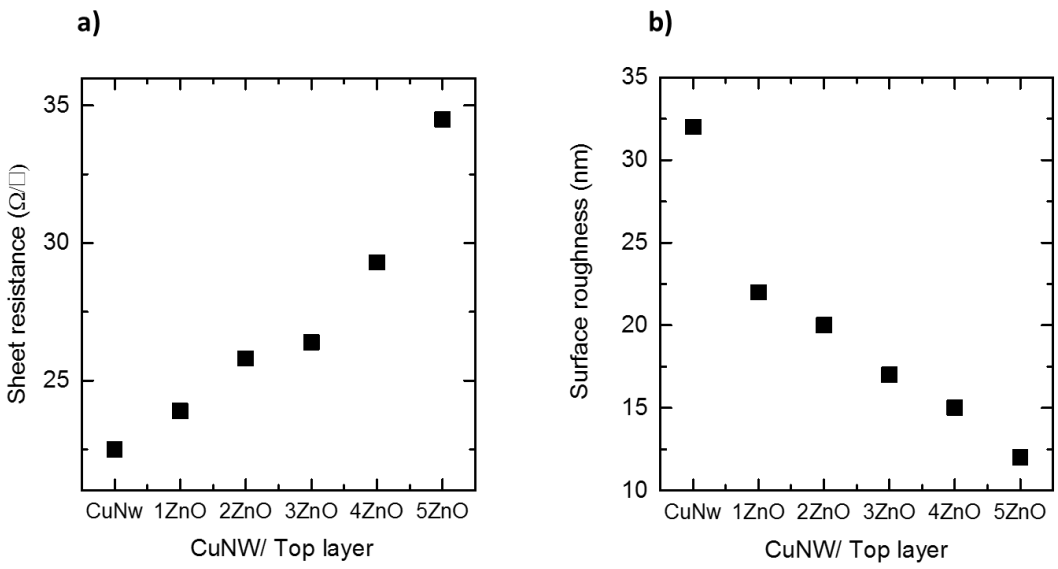

Figure 56. a) Sheet resistance and b) surface roughness of CuNW films with 0 to 5 ZnO top layer(s).

The plot in Figure 57 shows the evolution of R_s for CuNW/ZnO films with 0 to 5 layers of ZnO after 0, 5 ,10 ,25 and 50 days left in air.

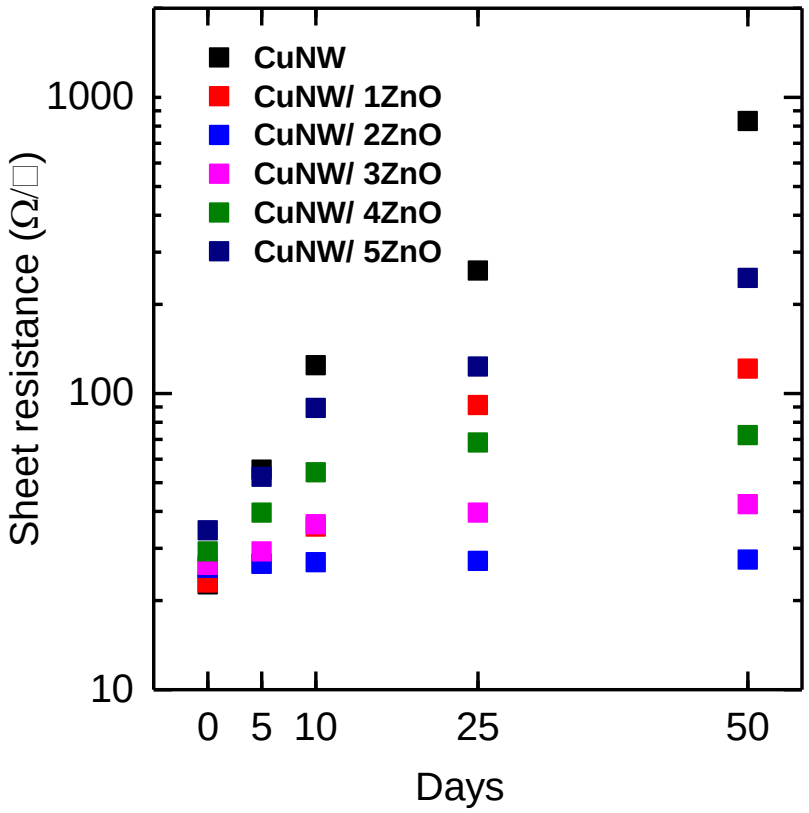

Figure 57. Sheet resistance of a CuNW film coated with 0 to 5 ZnO top layer(s) for 0, 5, 10, 25, and 50 days.

The results show that CuNW film coated with 5 layers of ZnO oxidises at a higher speed rate than other ZnO films while 2 layers of ZnO on top of a CuNW film are the most stable. After 50 days in air, the addition of 1 layer of ZnO increases the sheet resistance of up to 90 Ω/□ while with 3 layers, the sheet resistance passes from 26 Ω/□ to 42 Ω/□ and with the addition of 4 ZnO layers, the sheet resistance increases significantly passing from 29 Ω/□ to 72 Ω/□. On the other hand, the addition of 2 layers of ZnO increases the sheet resistance of only 1.7 Ω/□ after 50 days making therefore the CuNW/2 ZnO thin film a good candidate for a low-cost TC. A summary of the effect of the addition of 1

to 5 ZnO layer(s) on the roughness and sheet resistance for Day 0 and Day 50 is given in Table 13.

Film	Surface Roughness (nm)	R_s (Ω/□) Day 0	R_s (Ω/□) Day 50
CuNW	32	22.65	832
CuNW/ZnO	22	23	121
CuNW/PVP	32	49	2136
CuNW/Ethylcellulose	17	35	229
CuNW/Polystyrene	45	125.2	3263.2
CuNW/PEDOT:PSS	2	x	x

Table 13. Summary of the roughness and the evolution of R_s for day 0 and day 50 for CuNW/ZnO films with 0 to 5 ZnO layer(s).

5.4.3 Conclusion of this section

I have shown that the fabrication of CuNW TC is rendered difficult due to the intrinsic oxidation of copper. The addition of a suitable top layer helps to improve the overall surface roughness of the film and helps to prevent the oxidation of the thin film. ZnO is found to be the most suitable top layer for CuNW by keeping the same optical properties of NW films. The addition of only 2 layers of ZnO on top of CuNW films reduces significantly the oxidation rate of the films while retaining their transmittance and reducing their roughness. Therefore, the addition of a coating such as ZnO is a suitable technique in order to keep the optoelectronic performances of the film stable over time although it does not prevent the CuNW oxidation entirely.

5.5 Conclusion of the chapter

I have shown that a better understanding of both anneal and plasma treatments effects on CuNW can contribute to achieve highly performant CuNW TC thin films. This involves an optimisation of the pre- and post-treatments of these films. Therefore, a lactic acid solution ligand exchange performed on CuNW followed by a 2h-H_2/N_2 anneal give the best optoelectronic performances with films displaying a sheet resistance of 43 Ω/□ for 93% transmittance for a 90 nm CuNW film. This chapter has also pointed out the importance of controlling the surface roughness of the wires which is necessary for future application such as low-cost solar cells. I have also demonstrated that the choice of a top-layer is important and that the nature of the NW influences this choice. ZnO is a good candidate for top layers for TC owing their capacity to prevent the oxidation of the NW and to reduce the overall roughness of the wire. The addition of only 2 layers of ZnO prevents the oxidation of NW film where only an increase of 1.8 Ω/□ of the sheet resistance is observed after 50 days. However, no coating ensures a total protection against oxidation and in long term the films resistance increases. Hence the necessity to explore new materials that are more robust against oxidation. Therefore, in the next chapter, I will focus on the synthesis of bimetallic CuNi NW.

6 Synthesis of bimetallic Cu based NW

6.1 Introduction

In the previous chapter, I showed that applying CuNW as a TC is rendered difficult due to the rapid formation of an oxide layer on NW surface that diffuses through the wires and eventually breaks them. Therefore, during this oxidation process, the sheet resistance R_s of CuNW films increases over time until a point where they are not conductive anymore. This effect is even more dramatic for thinner films i.e. less NW overlap, hence more chances for the film network to break more quickly than for a thicker film. During the final stage of NW oxidation, films are formed of decomposed wires into small particles. Thinner NW films do not conduct anymore after 100 days of storage in air. I showed that the addition of a coating on top of the NW thin films can reduce the oxidation kinetic significantly but does not prevent it because films still oxidise over time. In this chapter, I will investigate a new method to chemically modify CuNW in order to make them more resistant to oxidation. To do so, I will create bimetallic NW by exploiting further the catalytic properties of Ni^{2+} in the synthesis. The aim is to produce thin films which remain stable for months. The synthesis principle remains the same as the previous chapters but with modifications. Table 14 summarises the reagents and quantities used throughout this chapter.

Reagents	Quantity (mmol)	Volume (ml)
$CuCl_2$	2.4	
$Ni(acac_2)$	1	
OLA		20
ODE		5
Zn^{2+} precursor: $Zn(acac)_2$, $ZnCl_2$	Varies throughout this chapter	

Table 14. Summary of the main reagents quantities or volumes used in this chapter.

I will investigate the synthesis of bimetallic CuNi NW in a co-reduction approach using Zinc precursor ($Zn(acac)_2$ or $ZnCl_2$) as a catalyst. I hypothesise that the final nature of Cu based NW is influenced by the Zn precursor concentration and counterion: I will show that the nature of the NW can be tuned by simply modifying Zn^{2+} counterion. Therefore, this chapter will be broken down into four studies:

1. Study of Zn^{2+} concentration effect on the NW size and nature;
2. Zn^{2+} counterion influence on NW atomic ordering and morphology;
3. TEM, STEM and XRD studies of bimetallic CuNi NW;
4. Electrocatalytic application of CuNi core-shell and alloyed NW.

6.2 Synthesis of CuNi NW

6.2.1 The role of the catalyst in CuNW synthesis

In section 3.1.1, I mentioned that NW were synthesised in presence of OLA using $Ni(acac)_2$ as a catalyst. Guo *et al.* [6] stated that the synthesis occurs in three steps as explained in the literature review in section 2.2.3.2.2 where $Ni(acac)_2$ is first reduced into zero valent Ni^0 and Cu^{2+} is reduced by Ni^0 via galvanic replacement. The galvanic replacement is driven by the favourable difference in reduction potential between both metals. The change in Gibbs free energy ΔE is given by:

$$\Delta E = -nFE \quad (12)$$

Where n is the number of moles of electron transferred, F is the Faraday's constant and E the potential difference between the two chemical half reactions.

The potential E is given by the Nernst equation:

$$E = E^0 + \frac{RT}{nF} ln(Q) \quad (13)$$

Where E^0 is the standard potential difference, T is the temperature, R is the ideal gas constant and Q is the activity constant which is dependent on the concentration of the precursors.

In order to confirm that the catalytic role is driven by the difference of potential between two metallic precursors, $Ni(acac)_2$ is replaced by $Zn(acac)_2$, an element with a lower reduction potential. The reduction potential of Cu^{2+}, Ni^{2+}, and Zn^{2+}, are displayed in Table 15.

Reduction reaction	E^0 (V Vs SHE)
$Cu^{2+} + 2\ e^-$	+ 0.34
$Ni^{2+} + 2\ e^-$	- 0.25
$Zn^{2+} + 2\ e^-$	- 0.76

Table 15. Reduction reaction and corresponding reduction standard potential for Cu^{2+}, Ni^{2+} and Zn^{2+}.

The ratio between the precursors were kept identical. The SEM in Figure 58)a) shows that pure CuNW were successfully synthesised (Figure 58)a) inset) in presence of $Zn(acac)_2$ as a catalyst. Some minor traces of Ni and Zn (Figure 58)b) and Figure 58)c)) were found which are believed to be due to the formation of CuNi NPs.

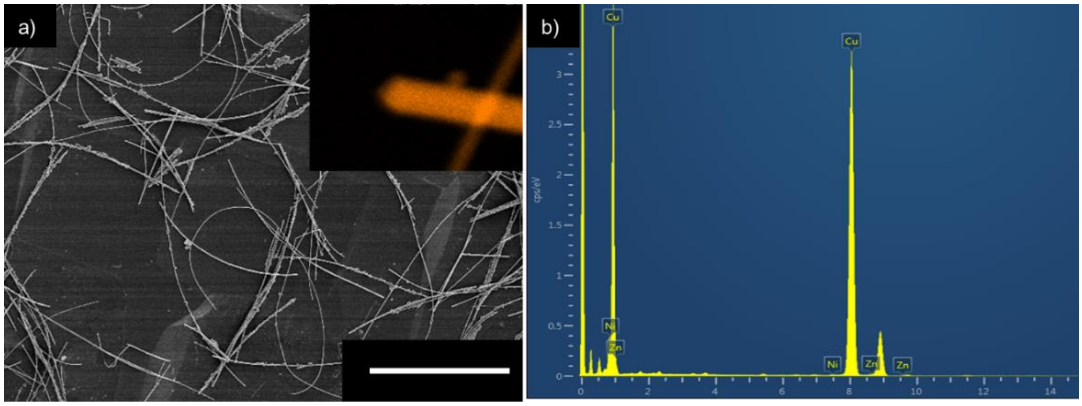

c)

Element	At%
Cu	99.7
Ni	0.2
Zn	0.1

Figure 58. a) SEM picture of CuNW synthesised using $Zn(acac)_2$ as a catalyst, the scale bar is at 20 µm, inset: EDX mapping of Cu, b) STEM-EDX elemental analysis graph of CuNW, c) atomic percentage of Cu, Ni and Zn elements.

The choice of the copper precursor, the precursor degree of oxidation (Cu^{+} or Cu^{2+}) and the ratio between metallic precursors are important parameters to take into account for CuNW synthesis. In presence of $CuCl_2$, the addition of a catalyst is necessary to promote CuNW growth [6] while Yang *et al.*[164] have successfully synthesised CuNW by replacing $CuCl_2$ with CuCl in OLA after 36h. In another work, Guo *et al.* [106] have reported the synthesis of CuNi core-shell NW by increasing Ni concentration and therefore modifying the ratio between Cu and Ni precursors: CuNi core-shell NW were obtained with a 3:5 ratio of Cu:Ni . The counterion linked to the precursor influences the choice of the ligand as well: Zhang *et al.* [43] synthesised CuNW using $Cu(acac)_2$ but OLA was replaced by two ligands: HDA and CTAB.

Table 16 summarises CuNW, CuNi NW and NPs synthesised using different solvothermal methods.

	Precursors initial ratio	Outcome	Ref
$Cu(acac)_2$, HDA, CTAB	X	CuNW	43
$CuCl_2$, $Ni(acac)_2$, OLA	2:1 Cu:Ni	CuNW	6
$CuCl_2$, $Zn(acac)_2$, OLA	2:1 Cu:Zn	CuNW	Present thesis
$CuCl_2$, $Ni(acac)_2$, OLA, ODE	3 :5 Cu:Ni	CuNi NW	106
$CuCl_2$, OLA	X	No NW	6
CuCl, OLA	X	CuNW	164

Table 16. Different NW and NPs synthesised using methods relevant to this chapter.

Therefore, this chapter will investigate the idea of using Zn precursor as a catalyst for the formation of CuNi NW using a co-reduction approach. Zn precursor concentration as well as counterion effects on NW size and nature will be investigated.

6.2.2 CuNi NW synthesis using Zn precursor.

In this section, I am interested in the Zn precursor concentration effect on the NW. Between 0.15 to 1.23 molar ratio of zinc acetylacetonate ($Zn(acac)_2$) with respect to $CuCl_2$, is added to the synthesis. I hypothesise that the addition of

Zn precursor modifies the nature of the wire by promoting the formation of bimetallic CuNi NW which leads to a change in the wire size.

6.2.2.1 *Morphology and size of the NW*

Both SEM images and diameter and length size distributions (depicted on the left of the SEM images) are shown in Figure 59. Each size distributions have been measured using 20 SEM images. A great disparity in both length and diameter according to $Zn(acac)_2$ concentration is observed. The addition of only 0.15 Zn/Cu initial molar ratio makes the NW shorter and thicker while increasing up to 0.61 of Zn/Cu ratio provides longer and thinner NW. Above a 0.61 molar ratio, the aspect ratio of the NW decreases again due to an increase of the diameter. The size distribution of the NW shows a great polydispersity in both diameter and length due mainly to the presence of NPs and small nanorods. For a 0.61 initial molar ratio, the size distribution is however narrower suggesting that this ratio provides a better stability of the system which increases the anisotropy of the wires.

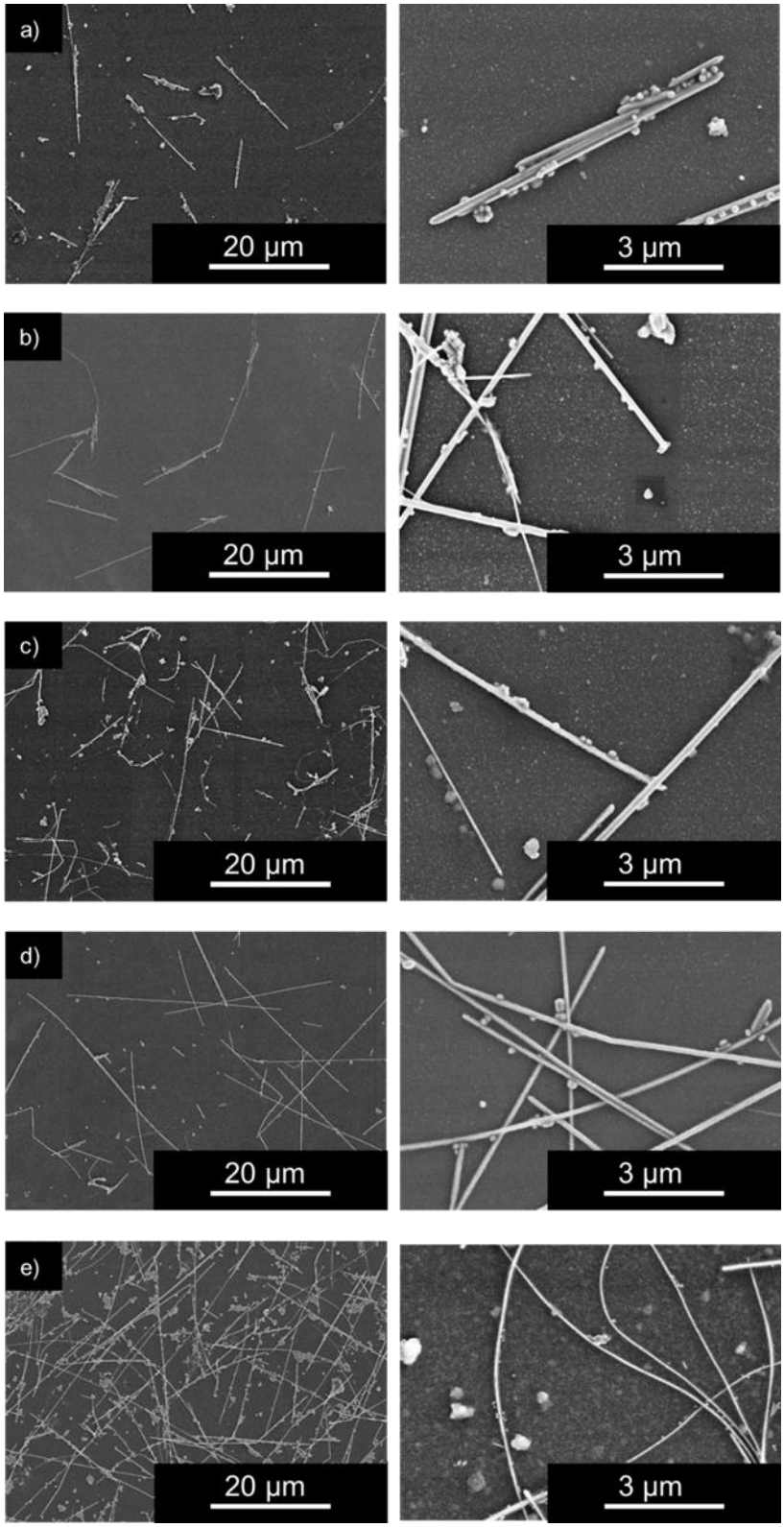

Figure 59. SEM pictures of CuNW synthesised with a) 0.15, b)0.36, c) 0.61, d) 0.84, and e) 1.23 Zn/Cu initial molar ratio.

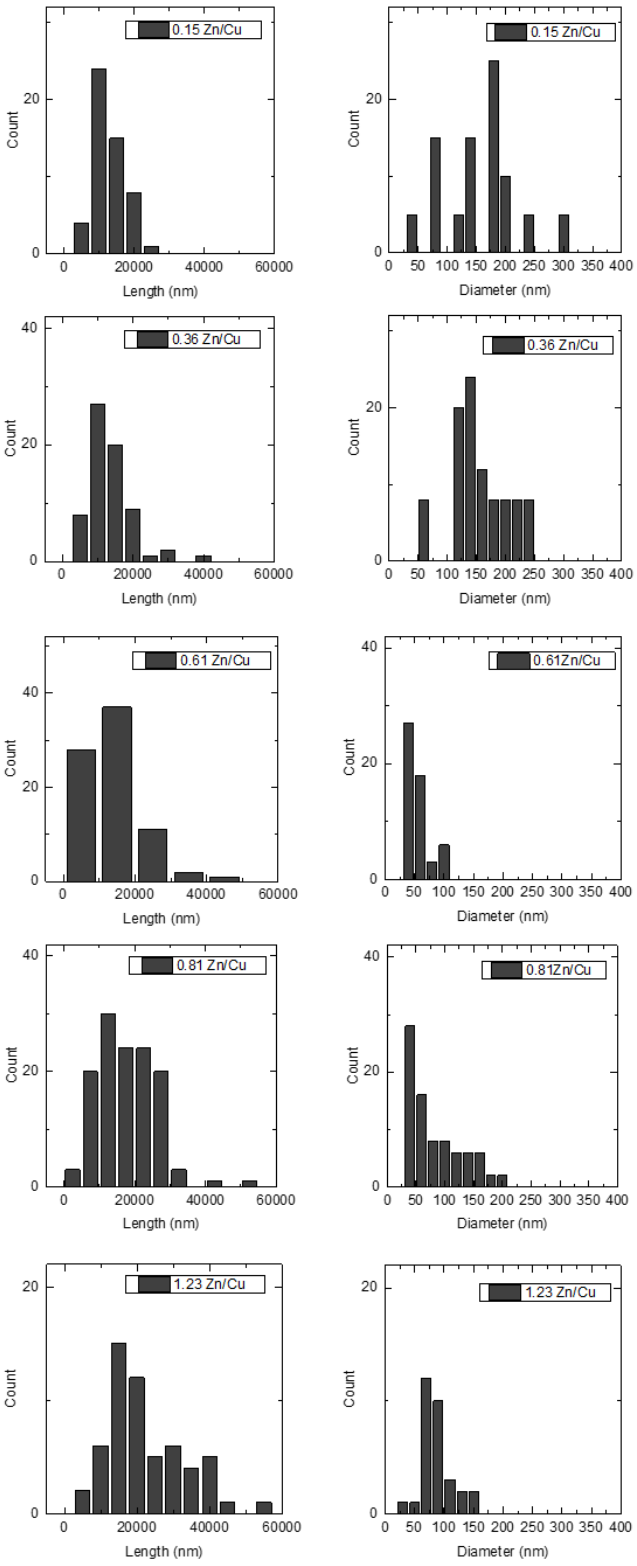

Figure 60. size distribution of both length and diameter for a) 0.15, b)0.36, c) 0.61, d) 0.84, and e) 1.23 Zn/Cu initial molar ratio.

The average length, diameter and corresponding aspect ratio are plotted in Figure 61.The Figure 61)a) shows that the length varies from 10 µm to 20 µm from 0.15 to 1.23 initial molar ratio of Zn/Cu while the diameter decreases from 140 nm to 41 nm from 0.15 to 0.61 then increases up to 83 nm for 1.23 initial molar ratio of Zn/Cu. Therefore, the highest aspect ratio is obtained with an initial Zn/Cu molar ratio of 0.61 as shown in Figure 61)b. These observations hint that the increase in Zn^{2+} content leads to an increase of the NW length suggesting that Zn^{2+} promotes the reduction of both Cu and Ni atoms that will be added up on the NW during the crystal growth. However, a diameter increase is observed above 0.61 Zn/Cu initial molar ratio which is responsible for the decrease of this aspect ratio. I hypothesise that the sudden drop in diameter, which is observed for an initial molar ratio of 0.61 marks the point where Ni is added on top on the CuNW forming a Cu core and Ni shell NW and the increase in diameter is due to an increase of the Ni content and therefore the Ni shell surrounding each CuNW.

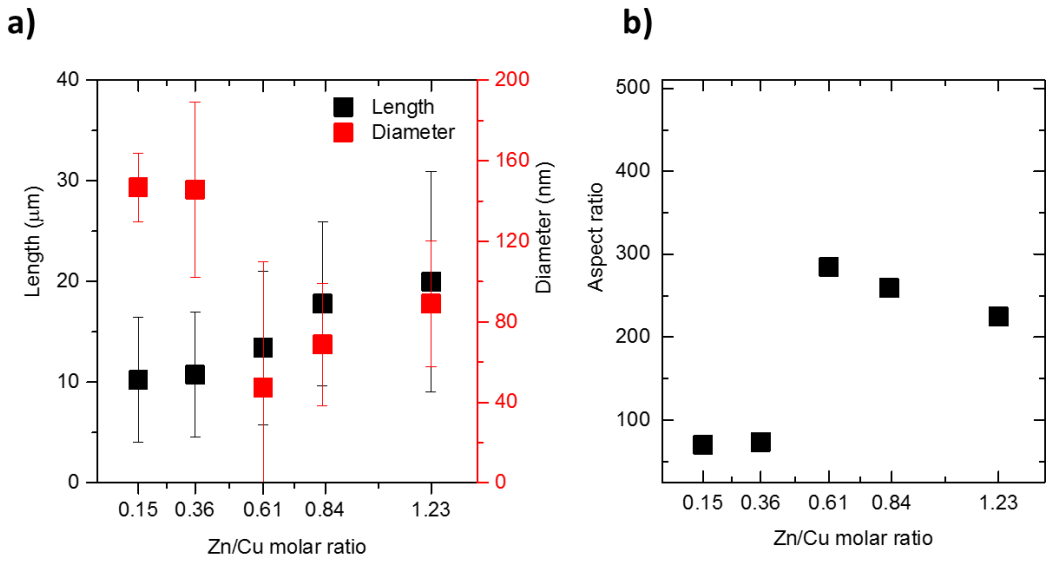

Figure 61.a) Length and diameter and corresponding b) aspect ratio of Cu based NW synthesised in presence of $Zn(acac)_2$.

6.2.2.2 *Nature of the NW*

In this section, I will investigate the effect of Zn^{2+} concentration on the reduction of Ni precursor and demonstrate that different concentrations of Zn^{2+} lead to CuNi NW with tuneable Ni contents using STEM-EDX analysis. EDX spectra of 0.15, 0.36, 0.84 and 1.23 initial molar ratio of Zn/Cu are depicted from Figure 62)a to Figure 62)e. I observe that initial Zn/Cu molar ratio of 0.15 and 0.36 do not modify the chemical nature of NW, forming only pure CuNW while Ni is present at contents of 25%, 20%, and 18 % for 0.61, 0.84 and 1.23 Zn/Cu initial molar ratio respectively. Carbon is present mainly in the film holder and small amounts are found in the outer layer of the NW. The EDX analysis reveals that the oxygen is present as well, in the outer surface of the wire and its content increases with Zn^{2+} initial content in the system. For the highest Zn/Cu ratio, Zn is also present most probably in the form of ZnO. The

count based on the spectra obtained from each element for all initial Zn/Cu molar ratio are plotted in Figure *63*.

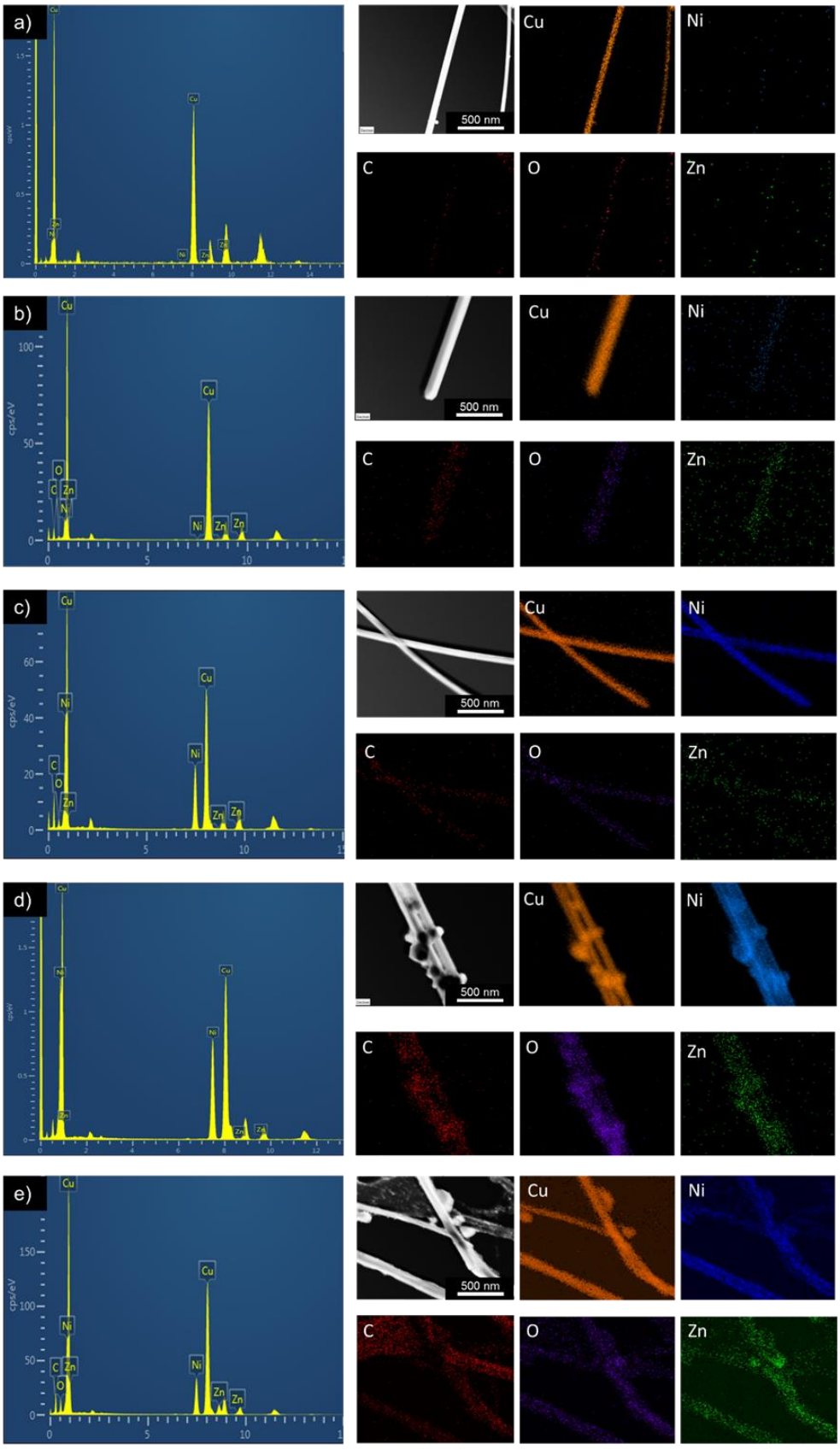

Figure 62. STEM-EDX elemental analysis graph and EDX maps of different elements: Cu, Ni, Zn, C, and O for NW synthesised with an initial molar ratio of Zn/Cu of a) 0.15, b)0.36, e)0.61, d)0.85 and e)1.23.

The plot shows that bimetallic CuNi NW are formed for Zn/Cu initial molar ratio equal or superior to 0.61. Below this ratio, the NW are made of Cu only therefore confirming that the reduction of Ni^{2+} occurs when Zn^{2+} reaches a certain concentration. The STEM-EDX data confirm therefore that for initial Zn/Cu molar ratios of 0.61 or higher, the NW are made of both Cu and Ni elements.

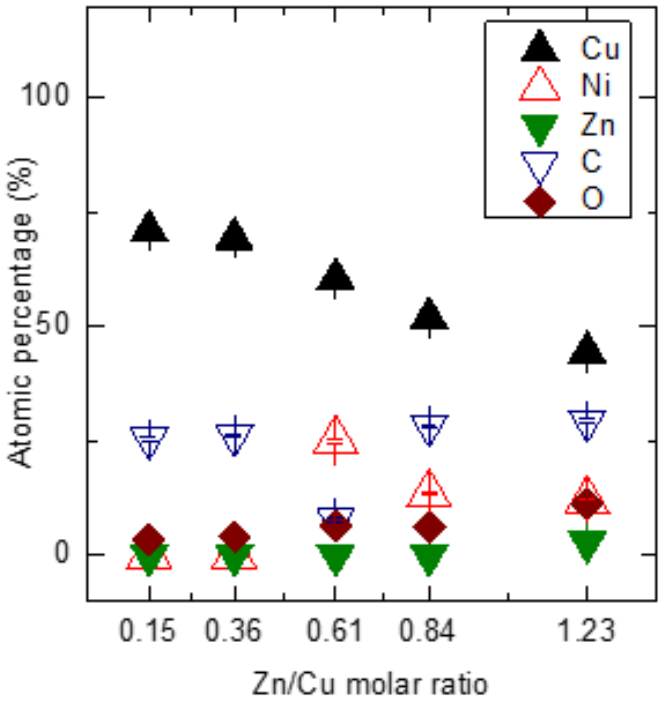

Figure 63. Plot of the different element counts measured by STEM-EDX according to the Zn/Cu molar ratio in the synthesis.

6.2.2.3 *Mechanism of formation of CuNi NW*

Two main conclusions can be drawn from the previous experiments:

1. At low Zn^{2+} concentration (below 0.61 Zn/Cu molar ratio), a Zn precursor concentration dependency over the total aspect ratio of the NW has been

identified: the increase in Zn^{2+} content induces an increase in the NW length suggesting that Zn^{2+} promotes the reduction of more atoms that can be used as building blocks for the NW growth. The increase in the aspect ratio of the NW shows that the addition of Zn^{2+} promotes the NW anisotropy.

2. Above a concentration threshold, Zn^{2+} is responsible for the reduction of Ni^{2+} into Ni atoms that participate into the reaction forming bimetallic CuNi NW. Therefore, the presence of Zn induces a change in the reaction kinetic of the system. It is known that elements of low reduction potential such as Ni^{2+} reduce in a lower rate than those with higher reduction potential such as Cu^{2+}. Since Ni^{2+}/Ni and Cu^{2+}/Cu couples exhibit reduction potentials far from each other, a CuNi core-shell formation is the most plausible structure formed where Cu^{2+} ions are reduced first and followed by Ni^{2+} ions. I hypothesise therefore, that when Zn/Cu initial ratio reaches a critical point, the presence of Zn^{2+} promotes the formation of CuNi core-shell NW by the following mechanism of growth: $CuCl_2$, $Ni(acac)_2$ and $Zn(acac)_2$ react with OLA forming complexes. When Zn/Cu ratio reaches 0.61, Zn^{2+} replaces Ni^{2+} role as a catalyst. A sufficient amount of Zn^{2+} is reduced into zero valent Zn^0. Cu^{2+} being more noble than Zn, Zn promotes the reduction of Cu precursors into Cu metallic atoms via galvanic replacement which progressively form CuNW. The remaining Zn atoms helps to reduce Ni^{2+} into metallic Ni^0 which are added up on top of CuNW.

6.2.2.4 *TEM study of the CuNi NW synthesised using $Zn(acac)_2$ as a catalyst*

In this section, CuNi NW synthesised with $Zn(acac)_2$ with a higher Ni content i.e. synthesised using a 1.23 Zn/Cu initial molar ratio will be investigated: the nature of the NW will be determined using HRTEM and STEM-EDX analyses.

An HRTEM picture of a NW synthesised using $Zn(acac)_2$ precursor is shown in Figure 64)a). From the picture, two regions can be distinguished: a low contrast region on the edges of the wire more likely made of the Ni shell and a high contrast region in the middle which is attributed to the Cu. The difference in the contrast observed is due to a difference in the thickness between the Cu core and the thinner Ni shell wrapping it. A closer look on the edge of the wire is represented in Figure 64)b) which shows the evolution of the crystalline structure along the section of the wire. The FFT is taken in three different areas a, b and c. The FFT of the zone a suggests a cubic symmetry with a lattice spacing, d_{111} = 0.24 nm which corresponds to NiO. In the zone b, the FFT shows that both NiO and Ni phases are present with Ni lattice spacing, d_{111} = 0.21 nm. The FFT of zone c reveals the presence of a highly ordered cubic phase composed only of Cu with a lattice spacing, d_{111} = 0.20 nm. In case of core-shell CuNi NCs, it has been shown [193] that a very thin layer attributed to NiO for Ni contents above 40% is formed on the surface of the bimetallic NPs of CuNi. Therefore, I hypothesise that the core-shell NW outer layer is made of an Ni oxide that diffuses through the Ni shell. This observation hints that the wire might progressively become a NiO/Cu core shell and therefore one can

argue the efficiency of the shell to protect the wire against oxidation through time.

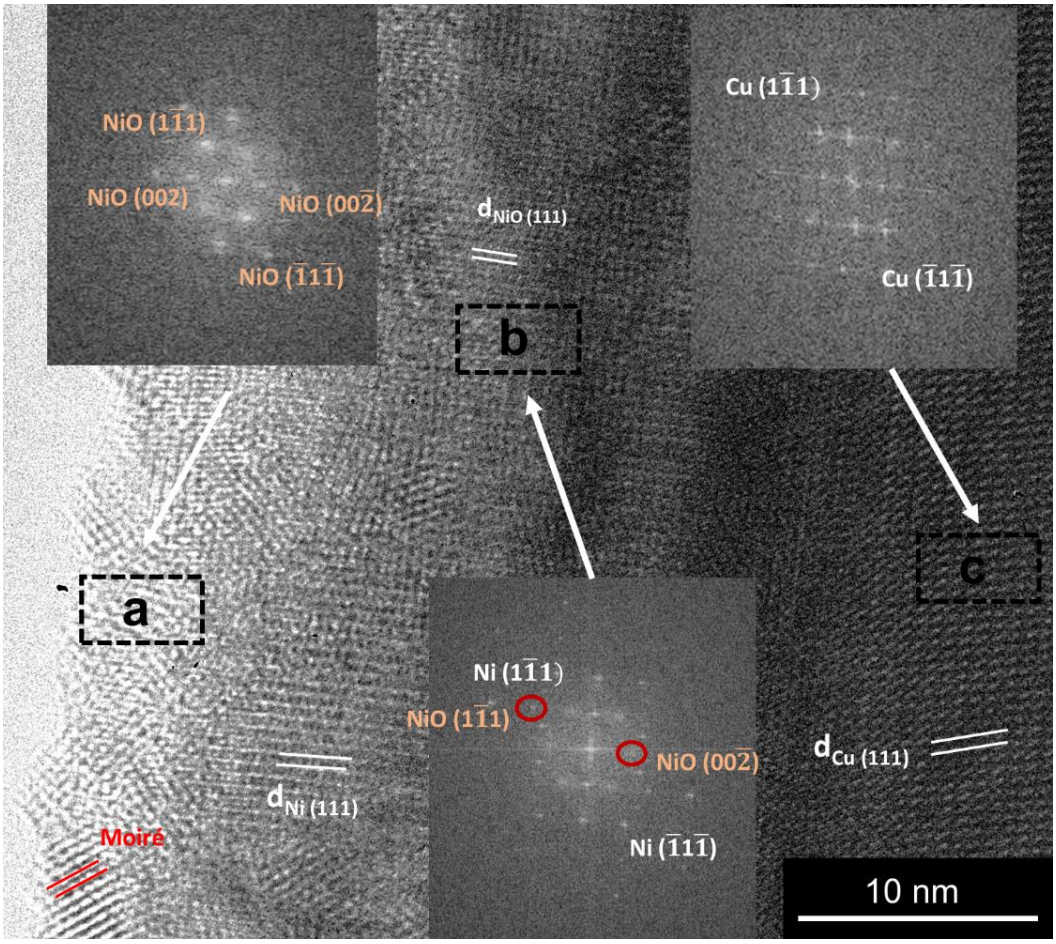

Figure 64. HRTEM of CuNi core-shell NW. Zoom on the a) NiO edge, b) Ni/NiO region and c) Cu core.

To investigate the oxide formation, a zoom on the extreme edge of the low contrast region is shown in Figure 65)b). The crystal structure of this extremity is not very clear as seen in Figure 65)c. The Figure 65)d) shows the presence of a very organised crystalline structure on the most extreme part of the wire where the formation of different crystals with different directions can be observed. Therefore, I hypothesise that the low contrast region is the result

of the addition of crystals of different directions that are piling up on top of each other resulting in the formation of a dense region as shown in Figure 65)d). Thus, the presence of triangular shaped crystals in the outer layer of the wire are due to the fact that this part is composed of a thinner crust whereas the inner part denser results in the addition of many crystals. Therefore, I conclude that the presence of a gradient of contrast level of the wire is due to the formation of a core-shell NW where Ni nanoparticles are adding up on top of Cu forming domain boundaries.

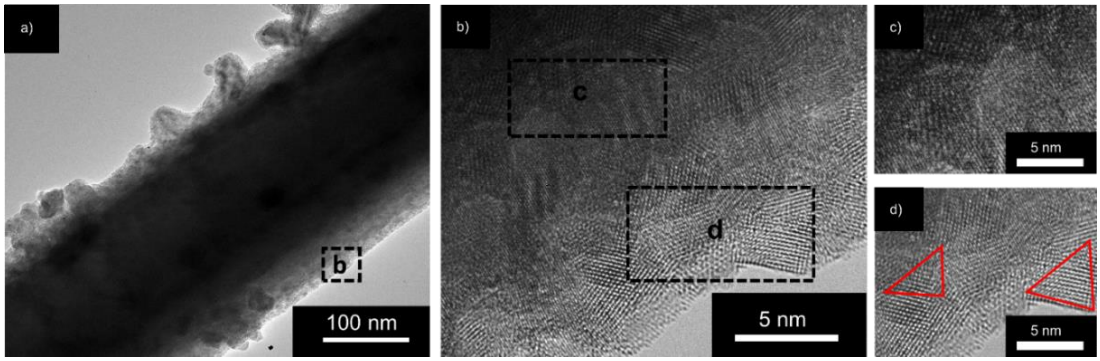

Figure 65. a) HRTEM of a CuNI core-shell NW, zoom on b) the edge of the wire, the c) upper and d) lower part of the edge.

Figure 66 shows an EDX image of CuNi NW synthesised using $Zn(acac)_2$. Cu and Ni maps in Figure 66)b and Figure 66)c respectively show the presence of two distinctive regions where Cu is concentrated in the middle of the wire and Ni in the outer layers which confirms further the presence of two distinctive regions; hinting the formation of a Cu core-Ni shell type NW. The maps show also that Ni diffuses through the Cu core creating an alloy in the centre which was already observed by Rathmell *et al.* [86]: Ni and Cu are miscible in all

proportions which explains the interdiffusion between these two elements. Ni count is observed to be constant through all the NW because the shell wraps the entire wire.

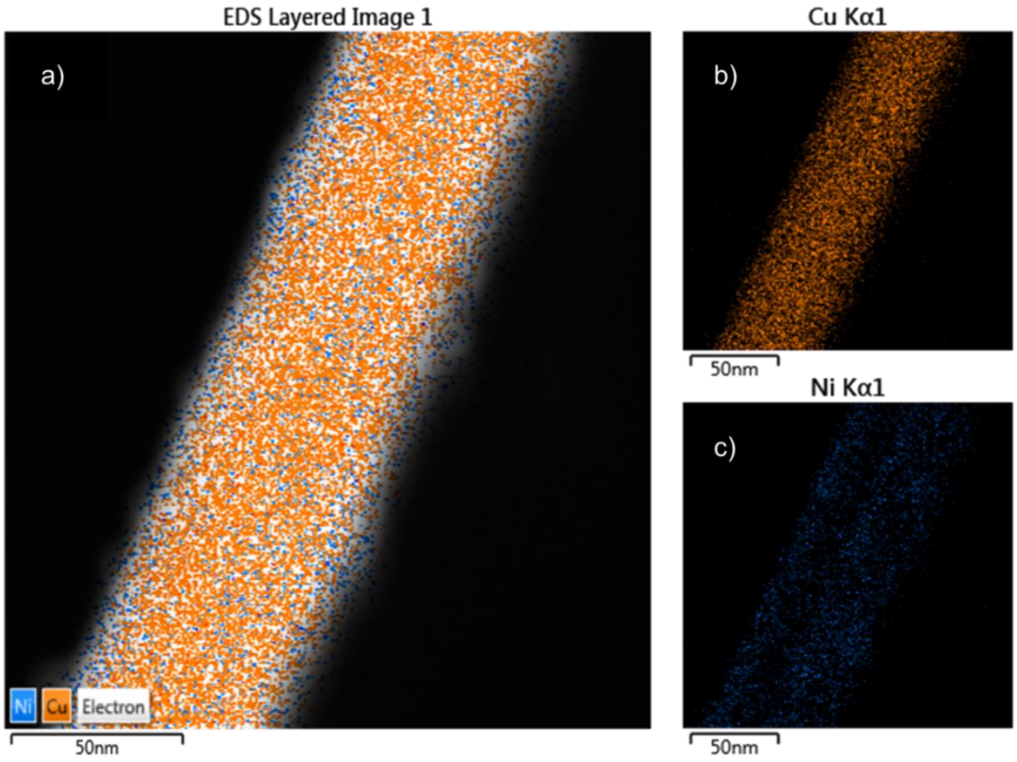

Figure 66. Energy X Ray Spectroscopy of CuNi NW synthesised using $Zn(acac)_2$ as a precursor.

The presence of a core-shell is further attested by the EDX elemental analysis graph and corresponding count of Cu and Ni in Figure 67)a) and in Figure 67)b) where it is suggested that Cu is three times more present than Ni.

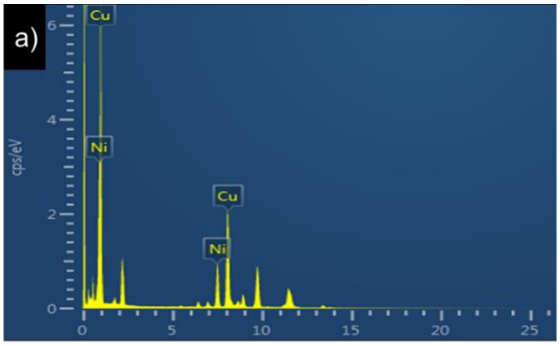

b)

Element	At%
Cu	71
Ni	29

Figure 67.a) EDX elemental analysis graph and b) corresponding count of Cu and Ni for NW synthesised using $Zn(acac)_2$ as a precursor.

Figure 68 measures the composition of Cu and Ni along and perpendicular to the wire axis. Cu composition is higher in the centre while Ni is present in lower quantities and does not vary much along the diameter of the NW which suggests that the amount of Ni is approximately the same across the wire.

The mechanism of formation of the core-shell can be explained as follows:

First Cu is formed and a reduction of Cu^{2+} ions occurs that leads to the growth to CuNW, then Ni^{2+} are reduced into Ni^0. Once the concentration of Ni^0 is superior to the critical concentration, the Ni atoms begin to accumulate on the surface of the wire. Guo *et al.* [106] have reported the synthesis of core-shell CuNi NW with either rough or smooth surface by changing the stirring speed. In the present case, this does not affect the morphology of the wire. The roughness of the wire is another hint that Ni is adding up on top of Cu.

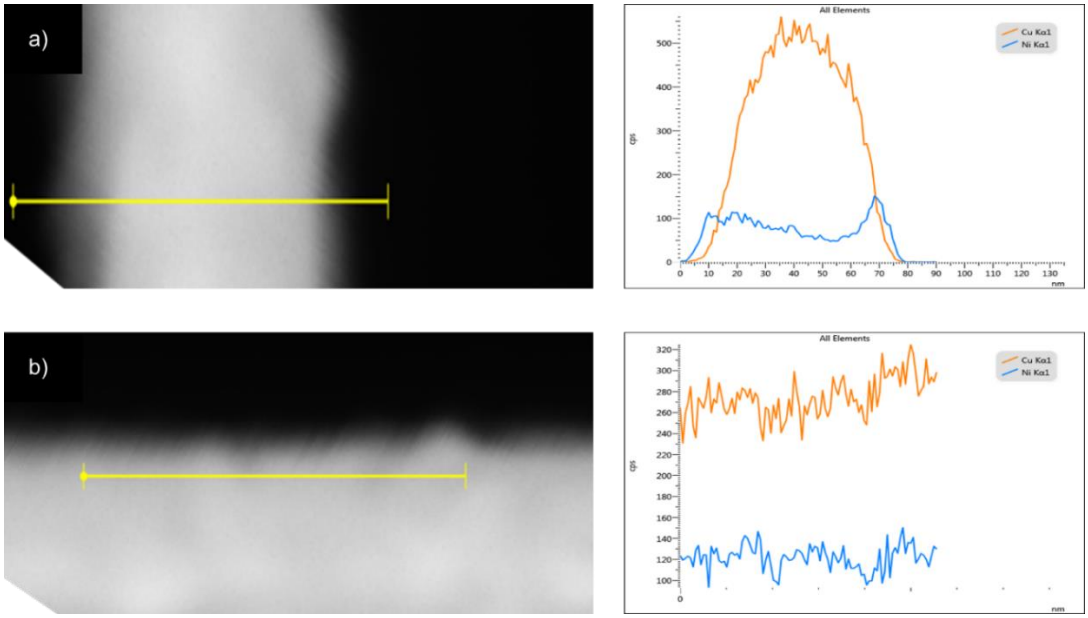

Figure 68. Line scan a) perpendicular to and b) along the wire axis of CuNi NW synthesised using $Zn(acac)_2$.

In conclusion, from the TEM observations, the EDX mapping in Figure 66, the Cu and Ni elemental analysis graph in Figure 67)a) and the line scans shown in Figure 68, I can confirm that NW synthesised using $Zn(acac)_2$ as a precursor possess a $Cu_{core}Ni_{shell}$ structure. These core-shell NW show the presence of an oxide that diffuses through the shell layer. The next section will study the counterion effect on the nature of the NW by replacing $Zn(acac)_2$ with $ZnCl_2$.

6.2.3 CuNi NW synthesis using $ZnCl_2$

6.2.3.1 *Experiments*

In this section , I will investigate the counterion effect by replacing $Zn(acac)_2$ with $ZnCl_2$. Similarly to what was observed before, Ni is present in the NW for Zn/Cu ratios equal or superior to 0.61 as shown in the STEM-EDX spectra in

Figure *69*. A plot of the Ni/Cu atomic percentage ratio based on the EDX elemental analysis map for both $Zn(acac)_2$ and $ZnCl_2$ at different Zn/Cu ratios are displayed in Figure *70*)a). From this plot, I can conclude that with the presence of $ZnCl_2$, Ni count is higher than with $Zn(acac)_2$ for ratio equal or superior to 0.61. For a 1.23 Zn/Cu initial molar ratio, Ni count passes from 0.5 with $Zn(acac)_2$ to 1 with the addition of $ZnCl_2$. Therefore, I can conclude that the presence of $ZnCl_2$ improves the reduction rate of $Ni(acac)_2$ into Ni^0 atoms.

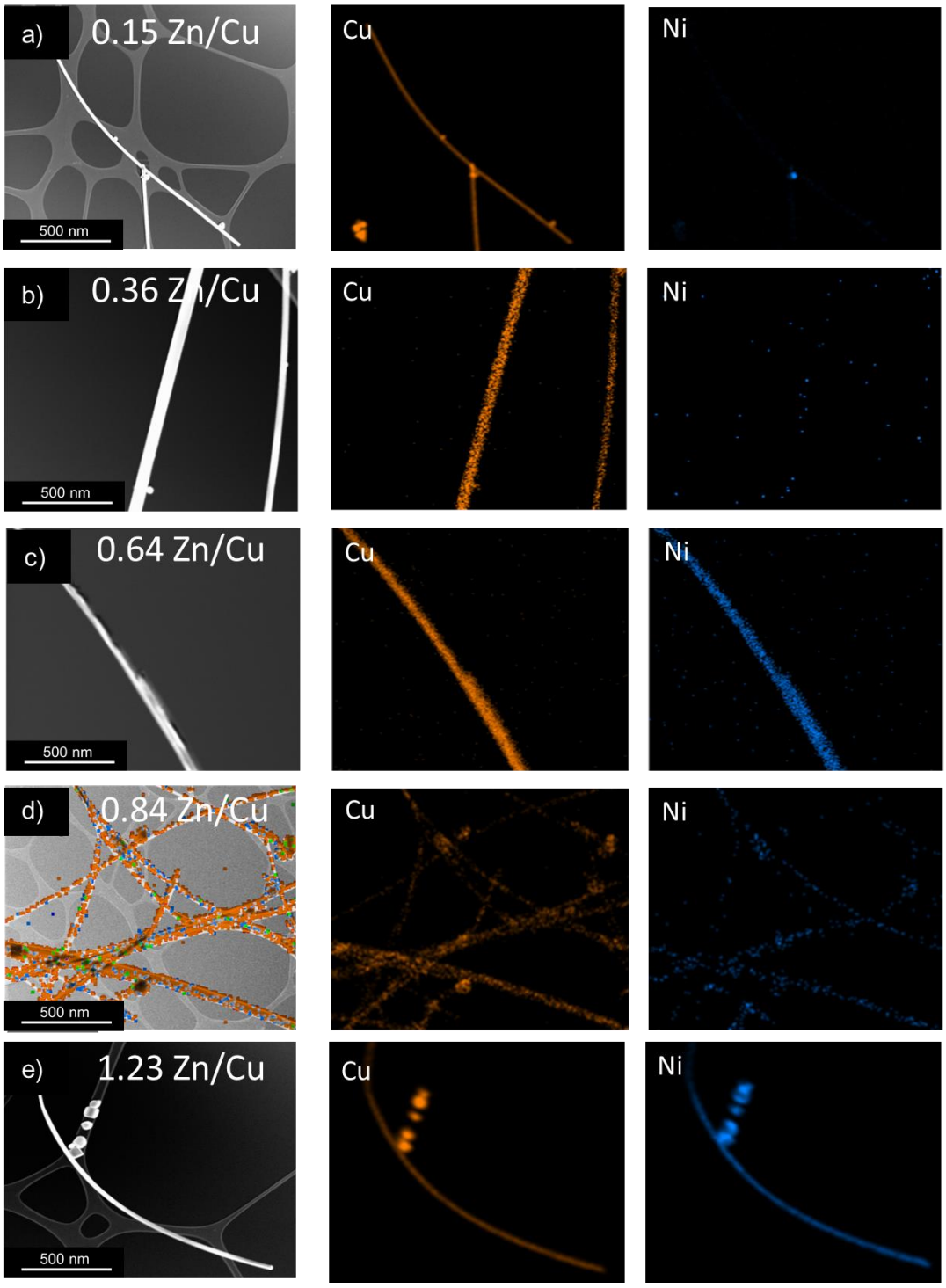

Figure 69. STEM-EDX images of Cu and Ni for a)0.15, b)0.36, c)0.61, d)0.84 and 1.23 Cu/Zn initial molar ratio of CuNi NW synthesised using $ZnCl_2$ as a precursor.

Regarding the aspect ratio of the CuNi NW shown in Figure 70)b), it passes from 10 to 210 with the highest for 0.61 Zn/Cu initial molar ratio. The aspect

ratio for NW synthesised using $ZnCl_2$ is quite close to the one obtained in presence of $Zn(acac)_2$. Therefore, I can conclude that the counterion does not affect the size of NW in this study.

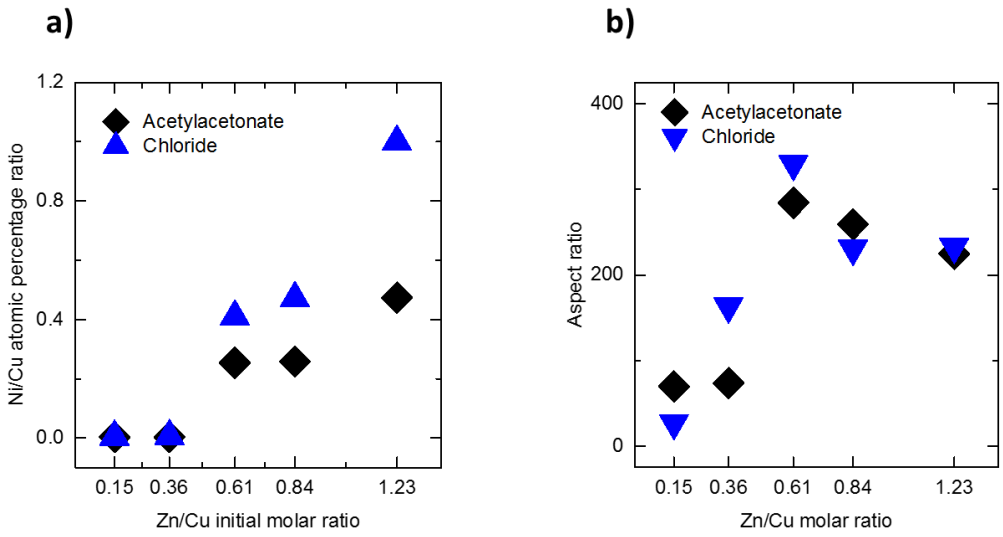

Figure 70. Ni/Cu atomic percentage extracted from the EDX elemental analysis graphs and aspect ratio of NW taken from 20 images for both $Zn(acac)_2$ and $ZnCl_2$ for different Zn/Cu initial molar ratios.

6.2.3.2 *TEM study of CuNi NW synthesised using $ZnCl_2$*

The HRTEM in Figure 71)a) shows a single NW formed using $ZnCl_2$ as a precursor. The main figure shows that the whole body of the wire is formed by mismatched stacking of atomic planes which are the result of the presence of some defects on the surface of the wire, in particular along the crystal growth: a bone-like structure that spans along the length of the whole wire is observed. These structures have been reported by smith *et al.* [194] in tungsten oxide nanowires and suggest the origin of these defects as a result of an oxygen deficiency driven growth. Here I suggest that the formation of the defects is

the result of a deficiency in either Cu or Ni in the middle of the wire. The zoom on the middle of the wire shows the presence of twin defects. The FFT shows a cubic symmetry which corresponds to a CuNi alloy of equimolar composition with a lattice spacing, d_{111} = 0.205 nm. Therefore, the NW corresponds only to one single crystal.

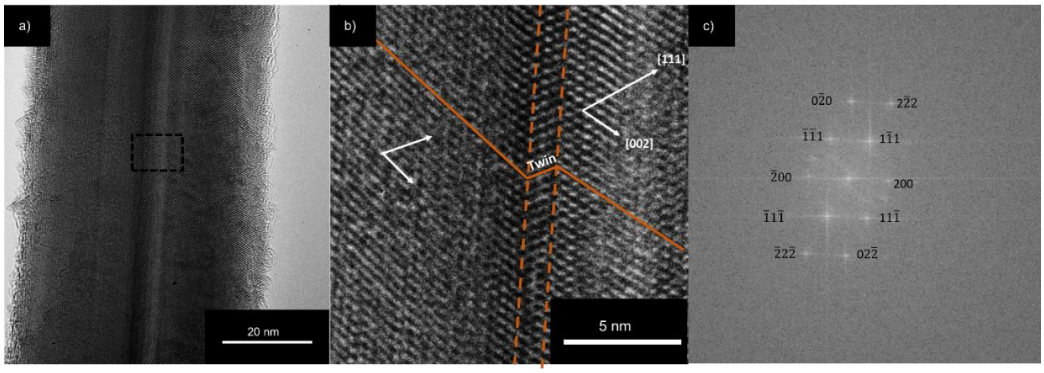

Figure 71.a) HRTEM of CuNi NW synthesised using $ZnCl_2$ as a catalyst b) Zoom in the middle of the wire showing a twin defect, c) FFT of the NW.

Wang *et al.*[195] have reported a stacking fault in Au NCs partially due to dislocations driven growth. These dislocations induce some plastic deformation which explains the difference in crystal structure. I therefore believe that defects on the NW induce some plastic deformations highlighted by the zoom in Figure 71)b). The chemical composition of the NW remains however constant along the NW axis. Therefore, I hypothesise that in presence of $ZnCl_2$ precursor, the NW that are formed are alloys.

In order to confirm my hypothesis, I investigate both Cu and Ni distributions using EDX analysis. The EDX map in Figure 72)a) and the STEM-EDX maps of Cu and Ni in Figure 72)b and in Figure 72)c show that the NW is formed of both elements that are evenly distributed. This is further confirmed by the EDX elemental analysis graph and the corresponding calculated count for Cu and Ni in Figure 73. Therefore, all the evidence points toward the fact that the NW is an alloy.

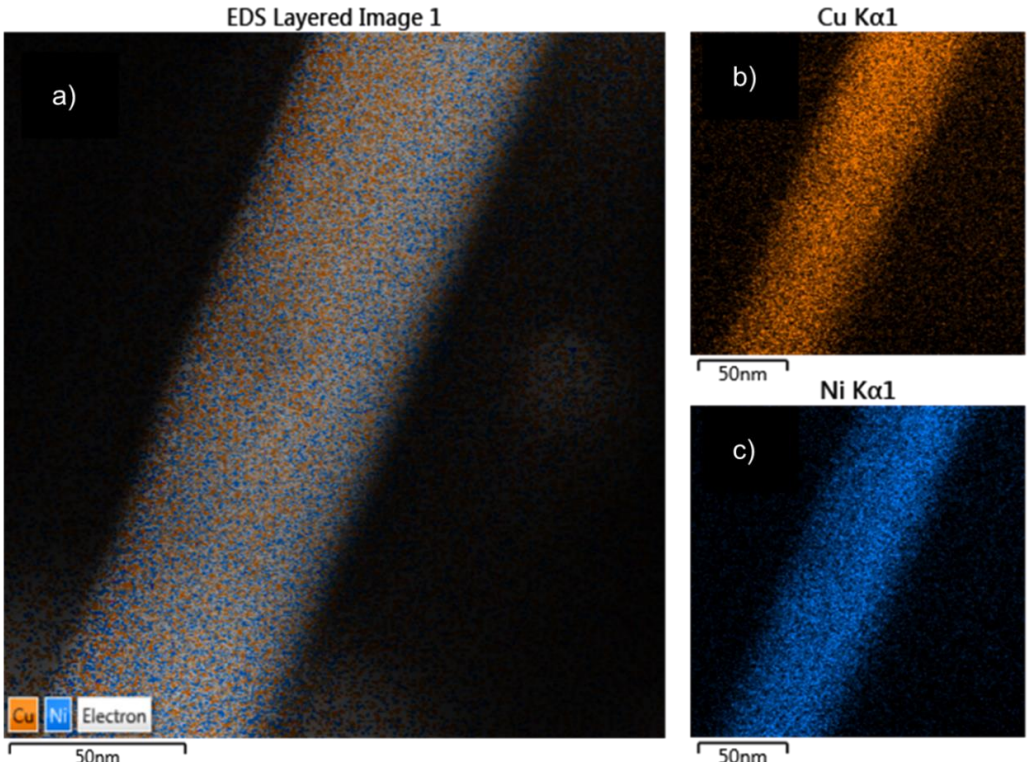

Figure 72. EDX map of Cu, Ni for a CuNi NW synthesised using $ZnCl_2$ precursor.

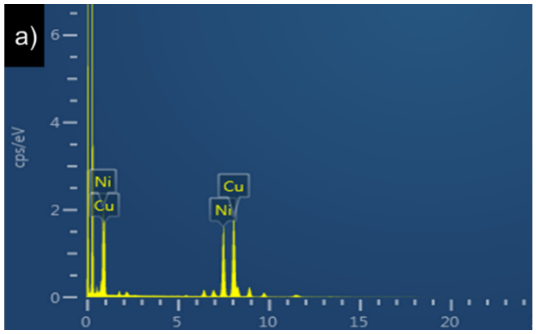

b)

Element	At%
Cu	55
Ni	45

Figure 73. a) EDX elemental analysis graph and b) corresponding count of Cu and Ni for NW synthesised using $ZnCl_2$.

Line scans are performed along the axis and perpendicular to the axis of the NW. The line scans shown in Figure 74 confirm that these NW are alloys. An interesting observation is that in the line scans shown, Cu and Ni peaks points are not located at the same position where Cu peak point is before Ni one. This suggests that there is the presence of a Cu defect in the middle of the wire, confirming the origin of the defects shown in the TEM above.

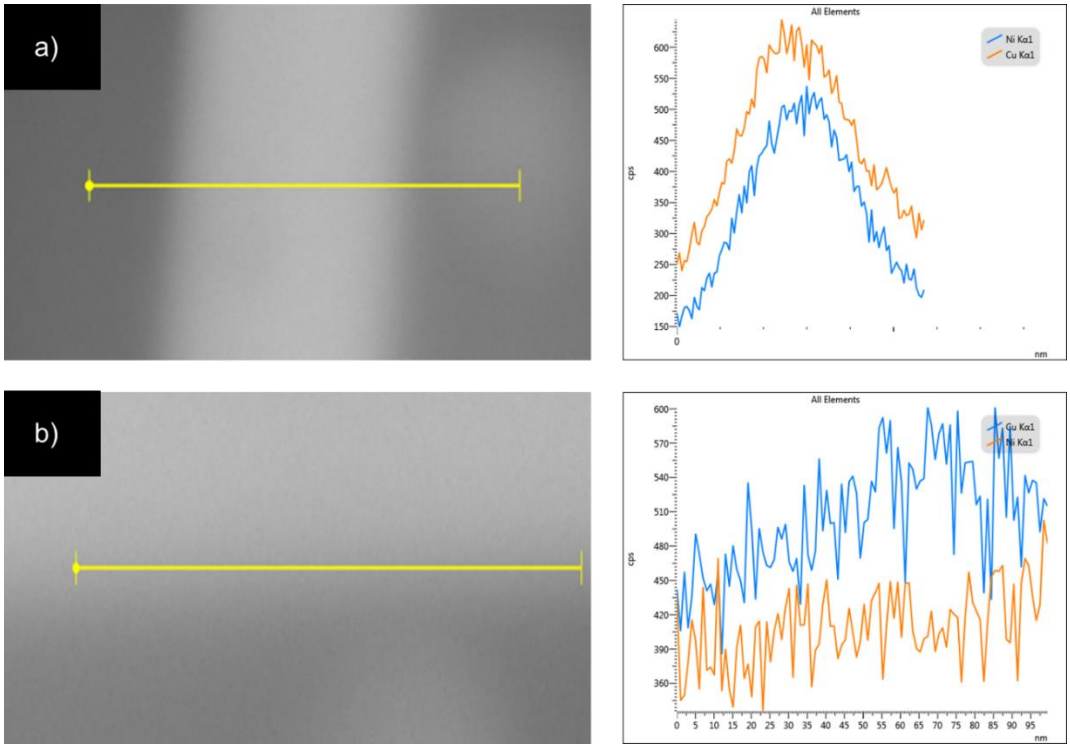

Figure 74. Line scan a) perpendicular to and b) along the NW axis of the CuNi NW synthesised using $ZnCl_2$ as a precursor.

The STEM pictures show that the composition in Ni and Cu is uniform in both axial and perpendicular directions. Cu count is slightly higher than Ni suggesting that the NW is deficient in Ni. In conclusion, from all the data analysis produced, I can confirm that CuNi bimetallic NW synthesised using $ZnCl_2$ as a precursor are an alloy.

The HRTEM analysis helps also to uncover very specific traits of these wires. Figure 75 presents a zoom of a CuNi alloy edge where some stacking faults of different directions are visible in the lower part of the image. On the top part of the wire, a very high contrast zone is observed. In this zone, the lattices are very organised. I hypothesise the presence of an oxide on the edge of wire.

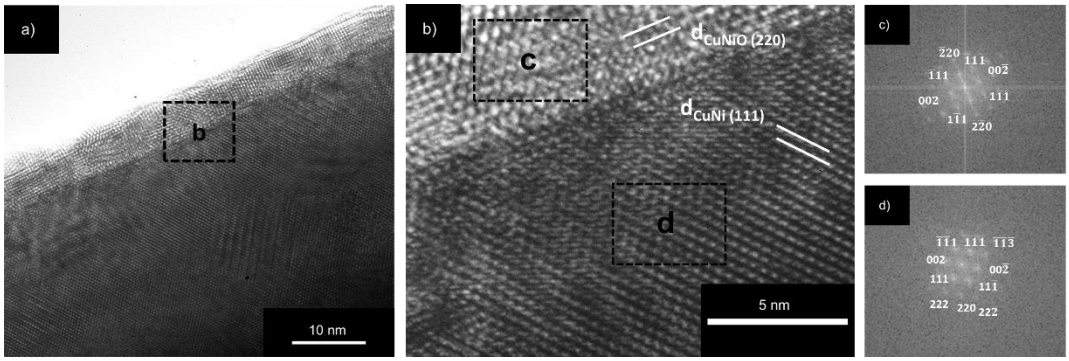

Figure 75. a) Section of a CuNi NW alloy, b) zoom on the edge of the NW, FFT of c) the upper part attributed to CuNiO and d) the lower part of the wire corresponding to CuNi.

A closer zoom of the edge between the two zones of the wire is shown in Figure 75)b). The FFTs of the NW edge displayed in Figure 75)c) and in Figure 75)d) show that both areas have two distinct ordered crystalline structures with a cubic symmetry. I hypothesise that the upper part of the wire is made of a copper nickel oxide with a lattice spacing, d = 0.356 nm. After many days left in air, the oxide layer remains constant (same thickness). The oxide formation for copper nickel alloy has been studied previously and it has been concluded that the oxide is of a protective nature: Pilling *et al.* [196] observed that in case of bulk Cu-Ni alloys with a between 40-60% Ni content, the oxidation rate is slower than of pure metals and lower Ni contents alloys. In my work, I observe the same trend where leaving the NW for many days does not impact the total thickness of the top layer. It is implied that the thinner the oxide is, the more protective as a barrier it is. The previous work on copper nickel oxide showed a temperature and nickel content dependency of the oxide formation rate where 40-60% Ni content resist more strongly to oxidation than pure Ni. Therefore, I conclude that the oxide layer is formed instantly and protects the

copper nickel alloy instead of diffusing through the layer which is commonly the case for CuNW as shown previously in chapter 5.

6.2.3.3 *Discussion*

6.2.3.3.1 Difference between alloyed and core-shell CuNi NW

The XRD plot in Figure 76 compares simulated diffractograms using *Crystaldiffract* software of Cu, Ni, 1:1 Cu:Ni alloy and 0.85:0.15 Cu:Ni core-shell with experimentally synthesised CuNi NW using 1.23 Zn/Cu initial ratio with either $ZnCl_2$ or $Zn(acac)_2$. Two set of peaks attributed to Cu are the {111} peak at 43,3° and the {200} peak at 50.4° and attributed to Ni: {111} at 44,3° and {200} at 51.7°. The peaks appear to both simulated core-shell and CuNi NW synthesised using $Zn(acac)_2$ diffractograms. Interestingly, the alloy presents a new set of peaks attributed to CuNi {111} and CuNi {200} at 43.9° and 51.2°. Therefore, $Zn(acac)_2$ XRD plot is similar to a core-shell plot while $ZnCl_2$ plot is closer to an alloy one.

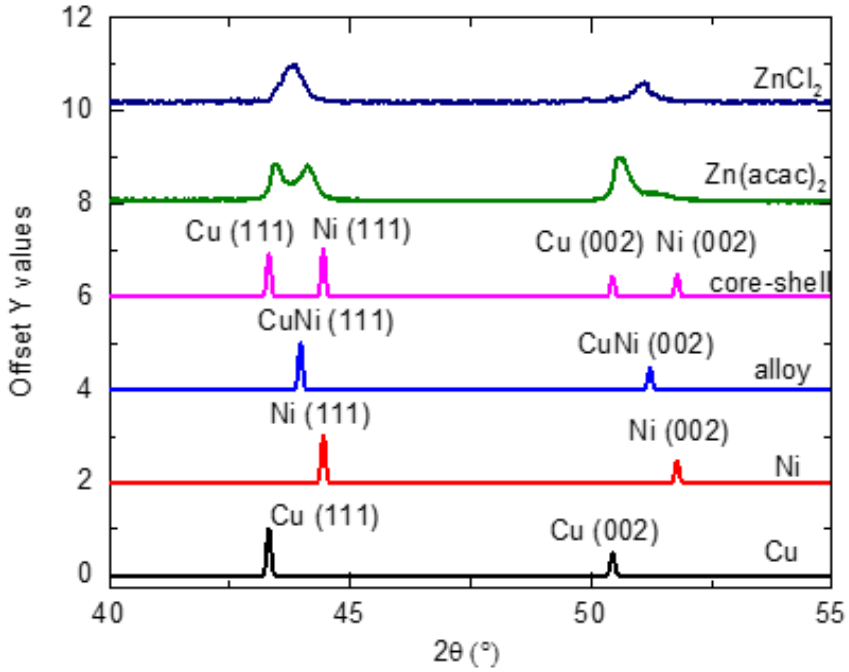

Figure 76. Comparison of CuNi alloy and core-shell simulated data and CuNi NW synthesised using $ZnCl_2$ and $Zn(acac)_2$.

6.2.3.3.2 Why is the presence of Zn precursor so important?

XRD analysis confirms what was observed with the HRTEM and STEM-EDX analyses: for the same concentration of Zn precursors, the addition of $Zn(acac)_2$ results in the formation of Cu_{core}/Ni_{shell} NW while $ZnCl_2$ presence forms single crystalline CuNi NW alloys. This study shows the importance of the counterion on the synthesis as it can influence the atomic ordering of the wire. The alloy and core-shell present also physical differences: CuNi alloys are single crystalline exhibiting a very well-defined crystal lattice while CuNi core-shell NW possess a very rough surface due to the piling up of Ni atoms. Both NW possess an oxide layer on the NW surface, but its nature differs: the oxide present on the core-shell is a diffusive one while the alloy presents a protective oxide layer.

To understand the role of Zn precursor, control experiments were performed replacing $ZnCl_2$ with NaCl for each Zn/Cu ratio studied (the NaCl concentration has been doubled by 2 to match Cl^- ions concentration), the resulting NW were made of pure CuNW. Table 17 summarises the nature of NW obtained according to the precursor added.

	NW nature	Synthesis method
$Zn(acac)_2$	Core-shell CuNi NW	Sequential reduction of Cu^{2+} and Ni^{2+}
$ZnCl_2$	Alloy CuNi NW	Co-reduction of Cu^{2+} and Ni^{2+} precursors
NaCl	Pure CuNW	No Ni reduction

Table 17. Nature of NW obtained by using Zn precursors ($ZnCl_2$ or $Zn(acac)_2$) or NaCl in the synthesis and proposed mechanism of reduction.

6.2.3.3.3 Mechanism of formation of CuNi alloys.

I have shown that regardless of the counterion, Zn^{2+} acts as a catalyst and by increasing its concentration, the reduction of $Ni(acac)_2$ precursor is promoted. The counterion plays however, an important role in defining the final nature of NW. The formation of an alloy occurs when M and N species are reduced simultaneously as explained in 2.4.3.1 .The mechanism of formation of alloy is not yet understood. The standard redox potential of Ni and Cu being far from each other, it is normally impossible for these elements to be reduced at the

same time in normal conditions. Researchers have hinted the possibility that the formation of nanoalloys was due to a modification of the standard reduction potential of the elements due to the reduction of their size [132]. Gilroy *et al.* [129] have suggested that the standard reduction potential of an element is modified in presence of different counterion such as halides for instance. Therefore, I believe that the presence of $ZnCl_2$ instead of $Zn(acac)_2$ modifies the standard reduction potential of Zn^{2+} and increasing its concentration compensate the slower reduction of $Ni(acac)_2$. This dual action allows a co-reduction of both Ni^{2+} and Cu^{2+}.

6.2.3.3.4 TC fabrication.

Bimetallic CuNi alloyed NW have a great potential as a TC owing their resistance upon oxidation. The more neutral grey colour of these NW makes them more suitable for application such as displays compared to CuNW. Therefore, CuNi NW TC were dispersed in isopropanol and TC fabrication was attempted following the same procedure described in 3.2. However, the vacuum filtration of the NW following the method described in 3.2.2 failed at the second step: the transfer to glass substrate of the filtered NW was impossible. Different hydrophilic and hydrophobic membranes were tested. The glass substrate was also replaced with polymers such as polyethylene naphthalate (PEN), PET and polydimethylsiloxane (PDMS) with moderate success. Other deposition techniques such as spin coating, Meyer road and dip coating were also tested but during the drying process, NW were agglomerating instead of forming a homogeneous mesh. CuNi alloyed NW has

a very unique surface energy which requires to explore other methods to fabricate NW film.

6.2.3.3.4.1 Conclusion of the section

In conclusion, the alloy formation occurs in two steps: for Zn/Cu initial molar ratio superior or equal to 0.61, Zn^{2+} replaces Ni^{2+} as catalyst and a small amount are reduced by OLA , then Ni^{2+} and Cu^{2+} are reduced at the same time forming an alloy. CuNi NW TC were not tested because the transfer from both hydrophobic and hydrophilic membranes to substrates was not successful. Overcoming this issue will be necessary in the future in order to explore the potential of these NW as TC. The next section will investigate the application of the different type of NW synthesised in this thesis as potential electrocatalyst.

6.2.4 CuNi NW as electrocatalyst for the Hydrogen Evolution Reaction

The previous sections have highlighted that the transition from monometallic to bimetallic nanowires requires a higher degree of control and understanding of the synthesis parameters. The bimetallic NW synthesised in this chapter provide the advantage to be structure dependent based on the counterion, and composition dependent according to the ratio of Zn/Cu. This section will test the functionality of these bimetallic nanowires and will investigate whether composition and chemical structure-activity dependencies can be identified. Pure CuNW, 1:1 and 2:1 alloyed NW, core shell NW and NiNW are tested as

potential electrocatalyst for HER using a method described in 3.3.11. The ratio between Cu and Ni is measured according to the EDX spectra of each samples.

The polarization curves are shown in the plot in Figure 77. The overpotential η of the materials defined in 3.3.11 ranges from 0.64V for CuNW to 0.39V for the 1:1 CuNi NW alloys. Materials with lower overpotential are favoured as it means less energy is required to generate the same amount of hydrogen.

It is interesting to observe that the current density as a function of the potential is very similar for both core-shell NW and Ni NW. I have mentioned in 2.4.3.2 that core-shell whose shell is superior to 6 atomic layers exhibit physical properties dominated by the shell. The same type of conclusion can be given in the present case. I observe also a composition-activity dependency where the overpotential increases by 0.23V when passing from a 1:1 to a 2:1 alloy suggesting that alloying Cu with Ni enhances the electrocatalytic properties of these NW for HER. The volcano curve of the exchange current density as a function of the calculated free Gibbs energy shown in Figure 78 suggests that Ni and Cu have opposite properties [197] in terms of catalytic activity: Ni is known to have a low electrocatalytic activity due to a poor adsorption of hydrogen on Ni surface. On the other hand, the electrocatalytic activity of Cu is too high: Cu has a too strong bonding strength and therefore fails to release the adsorbed hydrogen. Therefore, combining Cu and Ni allows to compensate the issues observed with their monometallic counterparts. The influence of the atomic ordering is not evidenced here as the core-shell and the alloy do not present the same ratio of Cu and Ni even though they have been synthesised using the same concentration of precursors.

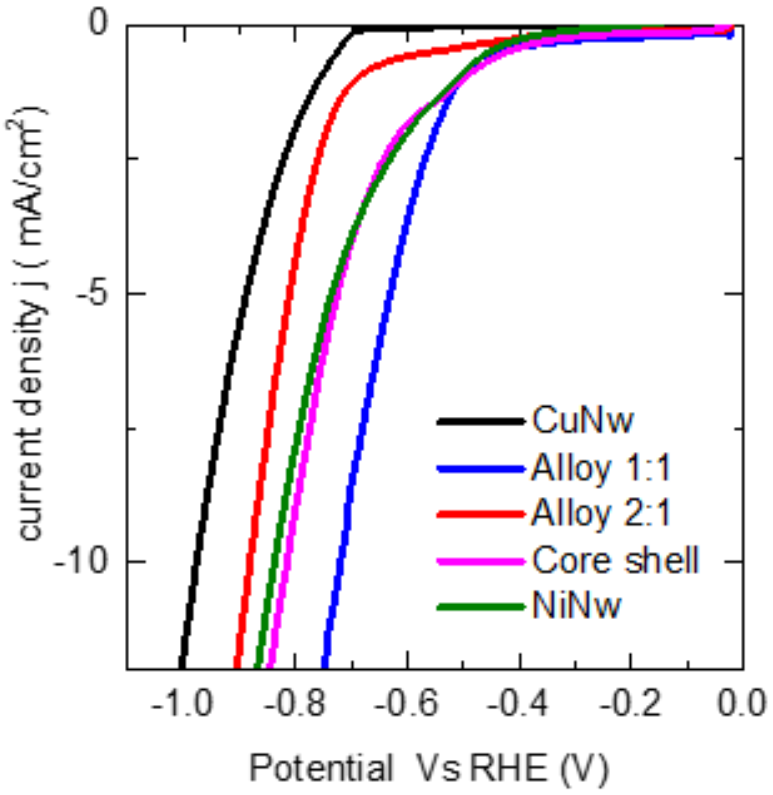

Figure 77. Polarization curve for CuNW, 1:1 and 2:1 CuNi alloyed NW, CuNi core shell NW and NiNW.

The Tafel plots extracted from the polarization curves and current densities are shown in Table 18: CuNW, 1:1 Alloys, 2:1 CuNi Alloys, CuNi core-shell and NiNW yield Tafel slopes of 60, 21, 43, 44 and 39 mV/decade respectively. The Tafel slopes values indicate the mechanism by which the H_2 is adsorbed and desorbed by the metal M and is described as follows [198,199]:

$$H_3O^+ + e^- + M \rightarrow M\text{-}H_{ads} + H_2O \quad (14)$$

then

$$M\text{-}H_{ads} + H_3O^+ + e^- \rightarrow H_2(g) + H_2O + M \quad (15)$$

Or

$$2\,M\text{-}H_{ads} \rightarrow 2M + H_2\,(g) \quad (16)$$

When the values of the Tafel slope are superior to -29 mV, the desorption of the hydrogen intermediate occurs by bounding release as shown in equation 2 M-Hads → 2M + H2 (g) (16). This step called the Tafel step is therefore the most probable mechanism of desorption of hydrogen from the core-shell and alloyed NW which means that the addition of Ni to the NW is efficient in lowering down the binding strength energy between Cu and the hydrogen bond.

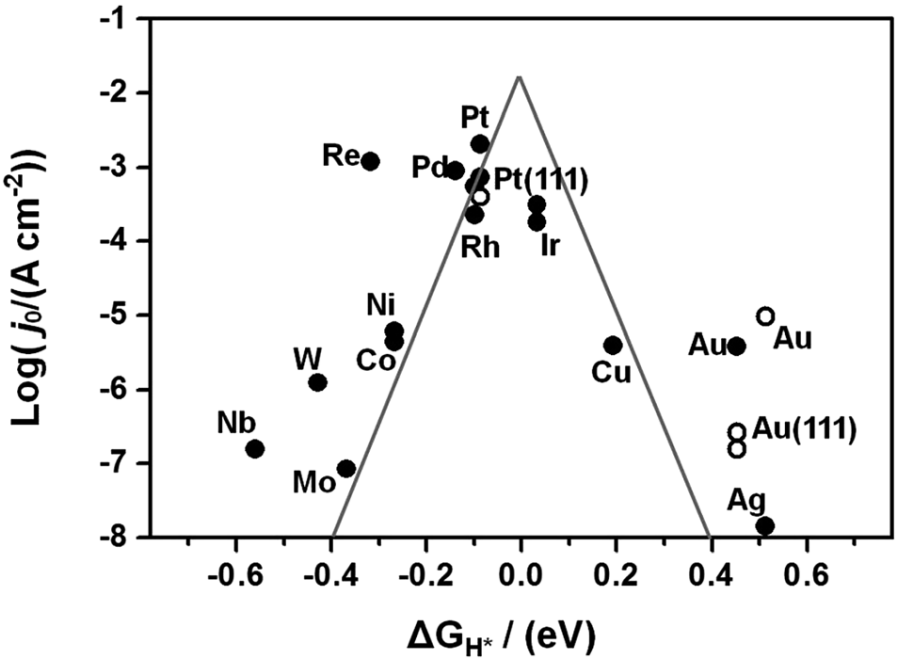

Figure 78. Volcano plot of the exchange current density j_0 according to the theoretical Gibbs free energy of hydrogen adsorption on pure metals [197,200].

The exchange current density shown in Table 18 measures the rate of reaction at the equilibrium potential. Good catalysts have usually a low overpotential but larger exchange current densities [197,201,202]. The alloys and the core-shell structures present higher values showing that they have better catalytic

performances making CuNi bimetallic NW promising candidates for HER applications.

	Tafel slope (mV/decade)	Current density (mA/cm^2)
CuNW	60	0.25
Alloy 1:1	21	0.36
Alloy 2:1	44	0.31
Core-shell	43	0.29
NiNW	39	0.3
Pt [203,204]	20-30	0.1-0.65

Table 18. Tafel slope and current density summary for each sample studied.

In conclusion, I have demonstrated that the bimetallic NW synthesised in this chapter have a potential application for HER. 1:1 CuNi alloy NW have shown the best catalytic performances owing a small Tafel slope and a high exchange current density. The mechanism of hydrogen desorption showed that alloying or adding a shell to CuNW manages to reduce the binding energy between Cu and hydrogen and therefore enhance the electrocatalytic properties of the material. A dependency in composition has been evidenced by the experiment: an increase in Ni content enhances the performances. The importance of the structure of the material is not highlighted by these results because too many parameters such as the roughness, the chemical composition or the presence of defects and/or oxides on the surface of the NW enter into account. However,

the fact that NiNW and the core-shell CuNi NW possess similar electrocatalytic performances suggest that the core-shell is overpowered by the properties of the thick shell. Therefore, 1:1 CuNi NW alloys can be considered as the extremely promising material for the HER application.

6.3 Conclusion of the chapter.

I have demonstrated that in a seed mediated growth the addition of a metallic precursor with a lower reduction potential can turn a synthesis designed to produce monometallic NW to the synthesis of bimetallic NW. By changing the chemical identity of the counterion attached to this precursor, a whole new set of materials can be designed. Therefore, I have been successful in making CuNi alloys of different compositions by replacing $Zn(acac)_2$ with $ZnCl_2$. This is the first report on the synthesis of single crystalline CuNi alloyed NW. Their potential is huge as they have been successfully tested as catalyst for HER applications: CuNi alloys present a high electrocatalytic activity with a Tafel slope comparable to Pt which is currently the best material in the market. Therefore, CuNi alloy NW stand as a promising alternative for low-cost HER materials.

7 Conclusion and future work

7.1 Conclusion

CuNW have a great potential in replacing the well-established ITO as a low-cost alternative TC. The work presented in this thesis demonstrates that by using the principles of chemistry, the main drawback of CuNW i.e. their rapid oxidation, can be turned into their advantage. The main contributions of this thesis are:

- The addition of non-coordinating solvents can tune the monomer reactivity while the nature and concentration of non-coordinating solvents can impact the final NW size. Therefore, a C18 chain 1-Octadecene produces NW with aspect ratio up to 1100 while middle chain C12 alkane and alkene (dodecane and 1-dodecene) show the best control of the NW anisotropy with diameters as low as 36 nm and 30 nm respectively.
- The surface chemistry of NW is a key parameter that influences the overall performances of the thin films. A lactic acid solution treatment followed by a H_2/N_2 plasma treatment is shown to give the best thin film efficiency owing a sheet resistance of 43 Ω/□ for a 93% transmittance.
- The oxidation of NW can be prevented by adding a top coating. Experimental measurements show that ZnO provides an excellent

coating for CuNW: the addition of only 2 layers of ZnO on top of CuNW films increases the sheet resistance by only 1.7 Ω/□ after 50 days.

- The seed-mediated NW synthesis can be turned into a co-reduction synthesis via galvanic replacement, with the addition of a Zn precursor. The concentration of Zn^{2+} salts needs to reach a threshold in order to effectively reduce Ni^{2+} salts and form bimetallic NW. The counterion plays an important role as well. Not only it influences the final shape of the NCs, but it also determines the nature of the NW. Two types of bimetallic NW have been identified: alloys can be generated using chloride ions while acetylacetonate ions form core-shell NW. This work led to the first ever synthesised CuNi alloyed NW.
- The HER electrocatalytic activity of the NW shows both chemical, composition and nature dependency. CuNi core-shell and Cu_2Ni alloyed NW have a similar activity to the one of NiNW while Cu_1Ni_1 alloyed NW are characterised by a higher activity compared to pure NiNW and CuNW, owing a Tafel slope as low as 21 mV/decade. A Cu:Ni 1:1 alloy possesses therefore an activity similar to Pt, the benchmark for HER reduction. Therefore, CuNi NW alloys have a promising future as low-cost alternatives for HER applications.

The main drawback of CuNW has been turned into an advantage by exploiting the defective nature of Cu: stable bimetallic alloyed CuNi NW were successfully synthesised and have potential applications in many fields such as electrochemistry, photonics and photovoltaics.

7.2 Future work

- Additional work can be done in order to improve the aspect ratio of NW that could increase their optoelectronic performances. Different approaches to reduce the diameter of NW should be explored by investigating the effects of coordinating solvents such as phosphines and alcohols. The carbon chain effect on the size of the NW can also be further explored by adding non-coordinating solvent with uneven number of carbons and longer chains with C>18 can be investigated as well. The effect of saturated bonds on the synthesis of CuNW has been clearly demonstrated in this thesis. Therefore, this work should be extended to other saturated chains such as the alkynes. The position of the bond in the non-coordinating solvent can be also easily investigated by replacing 1-octadecene with 9-octadecene for instance.
- In the pursuit of making CuNW synthesis eco-friendlier, replacing the coordinating solvent OLA with less toxic coordinating solvents such as DNA and RNA should be investigated.
- This thesis has shown the importance of using different characterisation techniques to unveil the properties of the NW. Other techniques need to be explored such as Atomic Force Microscopy (AFM) to study further NW aspect ratio and surface morphology, in-situ UV-vis to uncover the different NW growth steps, in-situ heating HRTEM to understand the microstructural evolution of Cu and CuNI NW in different annealing temperatures.

- CuNW TC film performances can be improved by forming a CuNW/ reduced Graphene oxide core-shell structure that could potentially prevent NW from oxidation while increasing the conductivity of the films.
- Vacuum filtration method has proven to be a very easy, quick and efficient technique to fabricate CuNW. However, its main drawback is that it requires the use of costly membranes (between £0.60 to £1 for each membrane). In addition to that, the aspect ratio of the NW depends on the filter pore size. Therefore, potentially cheaper techniques need to be explored such as stamp printing and slot-die coating.

- CuNi NW alloy TC need to be studied. Surface modification could involve the fabrication of an ink with a polymer that could be later burned off. The new properties of CuNi NW needs to be further explored, for instance exploiting the magnetic properties of this material could be the first step.
- A rough price estimation of CuNW and CuNI NW compared to AgNW is given in
- . This price was calculated according to the price of the raw materials necessary for the synthesis of each NW, and the yield of reaction. CuNW and CuNi NW are about 4 times cheaper than AgNW showing their potential as low-cost TC. These prices can be further decreased by increasing the yield of reaction for instance.

Material	AgNW	CuNW	CuNi NW
Price (£/g)	210	50	60

Table 19. Price of AgNW, CuNW and CuNi NW based on the price of raw materials and yield of reaction.

In order to make CuNW the future standard for low-cost TC, research needs to move towards the synthesis of multimetallic Cu based NW. There is in fact an unlimited combination of metallic NW that can be created and that can enhance the properties of the material. Each type of NW synthesised will require a deeper understanding of the fundamental chemistry it lies upon and of how each element affects the overall performances. Regarding their application as TC, two questions need to be addressed:

- How to increase the number of elements without reducing the NW aspect ratio?
- How to make sure that these new elements will not reduce the optoelectronic performances of the thin films?

Alloyed NW have distinct chemical and physical properties compared to monometallic NW and have a great potential in many applications such as electrochemical reactions and low-cost photovoltaics. It was highlighted in this thesis that, CuNi alloyed NW are resistant to oxidation which renders them superior to CuNW for application as TC.

Bibliography

1 Wagner, F. E. *et al.* Before striking gold in gold-ruby glass. *Nature* **407**, 691-692 (2000).

2 Cobb, H. L. Cadmium whiskers. *Monthly Rev. Am. Electroplaters Soc* **33**, 28-30 (1946).

3 Peach, M. O. Mechanism of Growth of Whiskers on Cadmium. *Journal of Applied Physics* **23**, 1401-1403 (1952).

4 Eshelby, J. D. A Tentative Theory of Metallic Whisker Growth. *Physical Review* **91**, 755-756 (1953).

5 Yin, Z. *et al.* Organic Photovoltaic Devices Using Highly Flexible Reduced Graphene Oxide Films as Transparent Electrodes. *ACS Nano* **4**, 5263-5268, doi:10.1021/nn1015874 (2010).

6 Guo, H. *et al.* Copper Nanowires as Fully Transparent Conductive Electrodes. *Sci. Rep.* **3**, doi:10.1038/srep02323

http://www.nature.com/srep/2013/130731/srep02323/abs/srep02323.html#supplementary-information (2013).

7 Yuhas, B. D. & Yang, P. Nanowire-Based All-Oxide Solar Cells. *Journal of the American Chemical Society* **131**, 3756-3761, doi:10.1021/ja8095575 (2009).

8 Lampert, C. M. Electrochromic materials and devices for energy efficient windows. *Solar Energy Materials* **11**, 1-27 (1984).

9 Svensson, J. & Granqvist, C. G. 30-37 (International Society for Optics and Photonics).

10 Ellmer, K. Past achievements and future challenges in the development of optically transparent electrodes. *Nature Photonics* **6**, 809-817 (2012).

11 Hecht, D. S., Hu, L. & Irvin, G. Emerging transparent electrodes based on thin films of carbon nanotubes, graphene, and metallic nanostructures. *Advanced Materials* **23**, 1482-1513 (2011).

12 De, S. & Coleman, J. N. The effects of percolation in nanostructured transparent conductors. *MRS Bulletin* **36**, 774-781 (2011).

13 O'Connor, B., Haughn, C., An, K.-H., Pipe, K. P. & Shtein, M. Transparent and conductive electrodes based on unpatterned, thin metal films. *Applied Physics Letters* **93**, 223304, doi:doi:http://dx.doi.org/10.1063/1.3028046 (2008).

14 Bid, A., Bora, A. & Raychaudhuri, A. K. Temperature dependence of the resistance of metallic nanowires of diameter $\ensuremath{\geqslant}15\phantom{\rule{0.3em}{0ex}}\mathrm{nm}$: Applicability of Bloch-Gr\"uneisen theorem. *Physical Review B* **74**, 035426 (2006).

15 Dressel, M. & Grüner, G. *Electrodynamics of Solids: Optical Properties of Electrons in Matter*. (Cambridge University Press, 2002).

16 De, S. *et al.* Silver nanowire networks as flexible, transparent, conducting films: extremely high DC to optical conductivity ratios. *ACS Nano* **3**, 1767-1774 (2009).

17 De, S., King, P. J., Lyons, P. E., Khan, U. & Coleman, J. N. Size effects and the problem with percolation in nanostructured transparent conductors. *ACS Nano* **4**, 7064-7072 (2010).

18 Kim, T. *et al.* Highly Transparent Au-Coated Ag Nanowire Transparent Electrode with Reduction in Haze. *ACS Applied Materials & Interfaces* **6**, 13527-13534, doi:10.1021/am502632t (2014).

19 Preston, C., Xu, Y., Han, X., Munday, J. N. & Hu, L. Optical haze of transparent and conductive silver nanowire films. *Nano Research* **6**, 461-468, doi:10.1007/s12274-013-0323-9 (2013).
20 Khanarian, G. *et al.* The optical and electrical properties of silver nanowire mesh films. *Journal of Applied Physics* **114**, 024302, doi:doi:http://dx.doi.org/10.1063/1.4812390 (2013).
21 Preston, C. *et al.* Silver nanowire transparent conducting paper-based electrode with high optical haze. *Journal of Materials Chemistry C* **2**, 1248-1254, doi:10.1039/c3tc31726a (2014).
22 Cui, F. *et al.* Synthesis of Ultrathin Copper Nanowires Using Tris(trimethylsilyl)silane for High-Performance and Low-Haze Transparent Conductors. *Nano Letters* **15**, 7610-7615, doi:10.1021/acs.nanolett.5b03422 (2015).
23 Araki, T. *et al.* Low haze transparent electrodes and highly conducting air dried films with ultra-long silver nanowires synthesized by one-step polyol method. *Nano Research* **7**, 236-245, doi:10.1007/s12274-013-0391-x (2014).
24 Lee, J.-Y., Connor, S. T., Cui, Y. & Peumans, P. Solution-Processed Metal Nanowire Mesh Transparent Electrodes. *Nano Letters* **8**, 689-692, doi:10.1021/nl073296g (2008).
25 Wu, H. *et al.* Electrospun Metal Nanofiber Webs as High-Performance Transparent Electrode. *Nano Letters* **10**, 4242-4248, doi:10.1021/nl102725k (2010).
26 Rathmell, A. R., Bergin, S. M., Hua, Y. L., Li, Z. Y. & Wiley, B. J. The Growth Mechanism of Copper Nanowires and Their Properties in Flexible, Transparent Conducting Films. *Adv Mater* **22**, 3558-3563 (2010).
27 Rathmell, A. R. & Wiley, B. J. The synthesis and coating of long, thin copper nanowires to make flexible, transparent conducting films on plastic substrates. *Advanced materials* **23**, 4798-4803, doi:10.1002/adma.201102284 (2011).
28 Kim, F., Sohn, K., Wu, J. & Huang, J. Chemical Synthesis of Gold Nanowires in Acidic Solutions. *Journal of the American Chemical Society* **130**, 14442-14443, doi:10.1021/ja806759v (2008).
29 Feng, H. *et al.* Simple and rapid synthesis of ultrathin gold nanowires, their self-assembly and application in surface-enhanced Raman scattering. *Chemical Communications*, 1984-1986, doi:10.1039/b822507a (2009).
30 Sun, Y., Yin, Y., Mayers, B. T., Herricks, T. & Xia, Y. Uniform Silver Nanowires Synthesis by Reducing AgNO3 with Ethylene Glycol in the Presence of Seeds and Poly(Vinyl Pyrrolidone). *Chemistry of Materials* **14**, 4736-4745, doi:10.1021/cm020587b (2002).
31 Sun, Y., Gates, B., Mayers, B. & Xia, Y. Crystalline silver nanowires by soft solution processing. *Nano Letters* **2**, 165-168 (2002).
32 Li, B., Ye, S., Stewart, I. E., Alvarez, S. & Wiley, B. J. Synthesis and Purification of Silver Nanowires To Make Conducting Films with a Transmittance of 99%. *Nano Letters* **15**, 6722-6726, doi:10.1021/acs.nanolett.5b02582 (2015).
33 Lin, W.-S. *et al.* Synthesis and Characterization of Iron Nanowires. *Journal of the Chinese Chemical Society* **60**, 85-91, doi:10.1002/jccs.201200263 (2013).
34 Jia, F. L., Zhang, L. Z., Shang, X. Y. & Yang, Y. Non-Aqueous Sol–Gel Approach towards the Controllable Synthesis of Nickel Nanospheres, Nanowires, and Nanoflowers. *Advanced Materials* **20**, 1050-1054, doi:10.1002/adma.200702159 (2008).

35 Huo, Z., Tsung, C.-k., Huang, W., Zhang, X. & Yang, P. Sub-Two Nanometer Single Crystal Au Nanowires. *Nano Letters* **8**, 2041-2044, doi:10.1021/nl8013549 (2008).
36 Maurer, J. H. M., González-García, L., Reiser, B., Kanelidis, I. & Kraus, T. Sintering of Ultrathin Gold Nanowires for Transparent Electronics. *ACS Applied Materials & Interfaces* **7**, 7838-7842, doi:10.1021/acsami.5b02088 (2015).
37 Wang, Z., Liu, J., Chen, X., Wan, J. & Qian, Y. A Simple Hydrothermal Route to Large-Scale Synthesis of Uniform Silver Nanowires. *Chemistry – A European Journal* **11**, 160-163, doi:10.1002/chem.200400705 (2005).
38 Siwei, Z. *et al.* Transferable self-welding silver nanowire network as high performance transparent flexible electrode. *Nanotechnology* **24**, 335202 (2013).
39 Elechiguerra, J. L. *et al.* Corrosion at the Nanoscale: The Case of Silver Nanowires and Nanoparticles. *Chemistry of Materials* **17**, 6042-6052, doi:10.1021/cm051532n (2005).
40 Bea, H. *et al.* Combining half-metals and multiferroics into epitaxial heterostructures for spintronics. *Applied Physics Letters* **88**, 062502-062503 (2006).
41 Das, C. T. a. R. Transparent conductive films (TCF) 2012-1022: Forecasts, technologies, players. (2012). <http://www.idtechex.com/research/reports/transparent-conductive-films-tcf-2012-2022-forecasts-technologies-players-000307.asp>.
42 Survey, U. G. Mineral Commodity Summaries 2012- Copper and Silver. 48 and 146.
43 Zhang, D. *et al.* Synthesis of Ultralong Copper Nanowires for High-Performance Transparent Electrodes. *Journal of the American Chemical Society* **134**, 14283-14286, doi:10.1021/ja3050184 (2012).
44 Han, S. *et al.* Fast Plasmonic Laser Nanowelding for a Cu-Nanowire Percolation Network for Flexible Transparent Conductors and Stretchable Electronics. *Advanced Materials* **26**, 5808-5814, doi:10.1002/adma.201400474 (2014).
45 Lee, J. *et al.* Very long Ag nanowire synthesis and its application in a highly transparent, conductive and flexible metal electrode touch panel. *Nanoscale* **4**, 6408-6414 (2012).
46 Athanassiou, E. K., Grossmann, P., Grass, R. N. & Stark, W. J. Template free, large scale synthesis of cobalt nanowires using magnetic fields for alignment. *Nanotechnology* **18**, 165606 (2007).
47 Pileni, M.-P. The role of soft colloidal templates in controlling the size and shape of inorganic nanocrystals. *Nat Mater* **2**, 145-150 (2003).
48 Zhao, Y., Zhang, Y., Li, Y. & Yan, Z. Soft synthesis of single-crystal copper nanowires of various scales. *New Journal of Chemistry* **36**, 130-138, doi:10.1039/c1nj20800d (2012).
49 Sun, L., Chien, C. L. & Searson, P. C. Fabrication of nanoporous single crystal mica templates for electrochemical deposition of nanowire arrays. *Journal of Materials Science* **35**, 1097-1103, doi:10.1023/a:1004703529210 (2000).
50 Markov, I. V. *Crystal growth for beginners: fundamentals of nucleation, crystal growth and epitaxy*. (World Scientific Singapore, 2003).
51 Volmer, M. *Kinetik der phasenbildung*. (T. Steinkopff, 1939).
52 LaMer, V. K. & Dinegar, R. H. Theory, Production and Mechanism of Formation of Monodispersed Hydrosols. *Journal of the American Chemical Society* **72**, 4847-4854, doi:10.1021/ja01167a001 (1950).
53 Mer, V. K. L. Nucleation in Phase Transitions. *Industrial & Engineering Chemistry* **44**, 1270-1277, doi:10.1021/ie50510a027 (1952).

54 Becker, R. & Döring, W. Kinetische behandlung der keimbildung in übersättigten dämpfen. *Annalen der Physik* **416**, 719-752 (1935).
55 (2013).
56 Manna, L., Scher, E. C. & Alivisatos, A. P. Shape Control of Colloidal Semiconductor Nanocrystals. *Journal of Cluster Science* **13**, 521-532, doi:10.1023/a:1021175612112 (2002).
57 Qi, B. *et al.* Influence of Ligand–Precursor Molar Ratio on the Size Evolution of Modifiable Iron Oxide Nanoparticles. *The Journal of Physical Chemistry C* **117**, 5429-5435, doi:10.1021/jp311509v (2013).
58 Wang, C. *et al.* One-Pot Synthesis of Oleylamine Coated AuAg Alloy NPs and Their Catalysis for CO Oxidation. *Chemistry of Materials* **21**, 433-435, doi:10.1021/cm802753j (2009).
59 Meng, F. & Jin, S. The solution growth of copper nanowires and nanotubes is driven by screw dislocations. *Nano letters* **12**, 234-239, doi:10.1021/nl203385u (2012).
60 Xia, Y., Xiong, Y., Lim, B. & Skrabalak, S. E. Shape-Controlled Synthesis of Metal Nanocrystals: Simple Chemistry Meets Complex Physics? *Angewandte Chemie International Edition* **48**, 60-103 (2009).
61 Xia, L., Wei, Z. & Wan, M. Conducting polymer nanostructures and their application in biosensors. *Journal of Colloid and Interface Science* **341**, 1-11, doi:http://dx.doi.org/10.1016/j.jcis.2009.09.029 (2010).
62 Song, Y. *et al.* Synthesis of Platinum Nanowire Networks Using a Soft Template. *Nano Letters* **7**, 3650-3655, doi:10.1021/nl0719123 (2007).
63 Zhong, W., Deng, J., Yang, Y. & Yang, W. Synthesis of Large-Area Three-Dimensional Polyaniline Nanowire Networks Using a “Soft Template”. *Macromolecular Rapid Communications* **26**, 395-400, doi:10.1002/marc.200400463 (2005).
64 Lv, R. *et al.* Growth and characterization of single-crystal ZnSe nanorods via surfactant soft-template method. *Solid State Communications* **130**, 241-245 (2004).
65 Wang, C., Chen, M., Zhu, G. & Lin, Z. A novel soft-template technique to synthesize metal Ag nanowire. *Journal of Colloid and Interface Science* **243**, 362-364 (2001).
66 Quake, S. R. & Scherer, A. From micro-to nanofabrication with soft materials. *Science* **290**, 1536-1540 (2000).
67 Gu, Q. *et al.* DNA nanowire fabrication. *Nanotechnology* **17**, R14 (2006).
68 Yen, M.-Y. *et al.* Convergent Electron Beam Induced Growth of Copper Nanostructures: Evidence of the Importance of a Soft Template. *Langmuir* **20**, 279-281, doi:10.1021/la035470w (2003).
69 Yen, M. Y. *et al.* Synthesis of Cable-Like Copper Nanowires. *Advanced Materials* **15**, 235-237, doi:10.1002/adma.200390054 (2003).
70 Chang, Y., Lye, M. L. & Zeng, H. C. Large-Scale Synthesis of High-Quality Ultralong Copper Nanowires. *Langmuir* **21**, 3746-3748, doi:10.1021/la050220w (2005).
71 Gale, N. H. Metals and metallurgy in the Chalcolithic period. *Bulletin of the American Schools of Oriental Research*, 37-61 (1991).
72 Holman, B. W. Copper in Antiquity. *Nature* **122**, 998 (1928).
73 Y.Chang , M. L. L. a. H. C. Z. Large scale synthesis of high quality ultralong copper nanowires. *Langmuir* **21**, 3746-3746 (2005).

74 Meng, F. & Jin, S. The Solution Growth of Copper Nanowires and Nanotubes is Driven by Screw Dislocations. *Nano Letters* **12**, 234-239, doi:10.1021/nl203385u (2011).
75 Filankembo, A. & Pileni, M. P. Is the Template of Self-Colloidal Assemblies the Only Factor That Controls Nanocrystal Shapes? *The Journal of Physical Chemistry B* **104**, 5865-5868, doi:10.1021/jp000268c (2000).
76 Mohl, M. *et al.* Low-Temperature Large-Scale Synthesis and Electrical Testing of Ultralong Copper Nanowires†. *Langmuir* **26**, 16496-16502, doi:10.1021/la101385e (2010).
77 Biçer, M. & Şişman, İ. Controlled synthesis of copper nano/microstructures using ascorbic acid in aqueous CTAB solution. *Powder Technology* **198**, 279-284, doi:http://dx.doi.org/10.1016/j.powtec.2009.11.022 (2010).
78 Yu, S., Hong, L., Liquan, C. & Xuejie, H. Obtaining ultra-long copper nanowires via a hydrothermal process. *Science and Technology of Advanced Materials* **6**, 761 (2005).
79 Bergin, S. M. *et al.* The effect of nanowire length and diameter on the properties of transparent, conducting nanowire films. *Nanoscale* **4**, 1996-2004 (2012).
80 Sachse, C. *et al.* Transparent, dip-coated silver nanowire electrodes for small molecule organic solar cells. *Organic Electronics* **14**, 143-148, doi:http://dx.doi.org/10.1016/j.orgel.2012.09.032 (2013).
81 Huang, J., Fan, R., Connor, S. & Yang, P. One-Step Patterning of Aligned Nanowire Arrays by Programmed Dip Coating. *Angewandte Chemie* **119**, 2466-2469 (2007).
82 Liu, N. *et al.* In situ growing and patterning of aligned organic nanowire arrays via dip coating. *Langmuir* **25**, 665-671 (2008).
83 Gan, X., Li, X., Gao, X., Zhuge, F. & Yu, W. ZnO nanowire/TiO< sub> 2</sub> nanoparticle photoanodes prepared by the ultrasonic irradiation assisted dip-coating method. *Thin Solid Films* **518**, 4809-4812 (2010).
84 Hu, L., Kim, H. S., Lee, J.-Y., Peumans, P. & Cui, Y. Scalable Coating and Properties of Transparent, Flexible, Silver Nanowire Electrodes. *ACS Nano* **4**, 2955-2963, doi:10.1021/nn1005232 (2010).
85 Rathmell, A. R., Bergin, S. M., Hua, Y. L., Li, Z. Y. & Wiley, B. J. The growth mechanism of copper nanowires and their properties in flexible, transparent conducting films. *Advanced materials* **22**, 3558-3563, doi:10.1002/adma.201000775 (2010).
86 Rathmell, A. R., Nguyen, M., Chi, M. & Wiley, B. J. Synthesis of Oxidation-Resistant Cupronickel Nanowires for Transparent Conducting Nanowire Networks. *Nano letters* **12**, 3193-3199, doi:10.1021/nl301168r (2012).
87 Mai, L. *et al.* Orientated Langmuir− Blodgett Assembly of VO2 Nanowires. *Nano Letters* **9**, 826-830 (2009).
88 Acharya, S., Panda, A. B., Belman, N., Efrima, S. & Golan, Y. A Semiconductor-Nanowire Assembly of Ultrahigh Junction Density by the Langmuir–Blodgett Technique. *Advanced Materials* **18**, 210-213 (2006).
89 Wang, D., Chang, Y.-L., Liu, Z. & Dai, H. Oxidation resistant germanium nanowires: Bulk synthesis, long chain alkanethiol functionalization, and Langmuir-Blodgett assembly. *Journal of the American Chemical Society* **127**, 11871-11875 (2005).
90 Tao, A. *et al.* Langmuir-Blodgett silver nanowire monolayers for molecular sensing using surface-enhanced Raman spectroscopy. *Nano Letters* **3**, 1229-1233 (2003).

91 Kim, D.-H., Park, M.-R. & Lee, G.-H. Preparation of high quality ITO films on a plastic substrate using RF magnetron sputtering. *Surface and Coatings Technology* **201**, 927-931, doi:http://dx.doi.org/10.1016/j.surfcoat.2006.01.004 (2006).
92 Liu, C.-H. & Yu, X. Silver nanowire-based transparent, flexible, and conductive thin film. *Nanoscale Research Letters* **6**, 75 (2011).
93 Zeng, X.-Y., Zhang, Q.-K., Yu, R.-M. & Lu, C.-Z. A New Transparent Conductor: Silver Nanowire Film Buried at the Surface of a Transparent Polymer. *Advanced materials* **22**, 4484-4488, doi:10.1002/adma.201001811 (2010).
94 Yu, Z. *et al.* Highly Flexible Silver Nanowire Electrodes for Shape-Memory Polymer Light-Emitting Diodes. *Advanced Materials* **23**, 664-668, doi:10.1002/adma.201003398 (2011).
95 Garnett, E. C. *et al.* Self-limited plasmonic welding of silver nanowire junctions. *Nat Mater* **11**, 241-249, doi:http://www.nature.com/nmat/journal/v11/n3/abs/nmat3238.html#supplementary-information (2012).
96 Tokuno, T. *et al.* Fabrication of silver nanowire transparent electrodes at room temperature. *Nano Research* **4**, 1215-1222, doi:10.1007/s12274-011-0172-3 (2011).
97 Lin, B., Gelves, G. A., Haber, J. A. & Sundararaj, U. Electrical, rheological, and mechanical properties of polystyrene/copper nanowire nanocomposites. *Industrial & engineering chemistry research* **46**, 2481-2487 (2007).
98 Hjerrild, N. E. *et al.* Transfer Printed Silver Nanowire Transparent Conductors for PbS–ZnO Heterojunction Quantum Dot Solar Cells. *ACS Applied Materials & Interfaces* **7**, 6417-6421, doi:10.1021/am505646d (2015).
99 Gaynor, W., Burkhard, G. F., McGehee, M. D. & Peumans, P. Smooth Nanowire/Polymer Composite Transparent Electrodes. *Advanced Materials* **23**, 2905-2910, doi:10.1002/adma.201100566 (2011).
100 Im, H.-G. *et al.* Flexible Transparent Conducting Hybrid Film Using a Surface-Embedded Copper Nanowire Network: A Highly Oxidation-Resistant Copper Nanowire Electrode for Flexible Optoelectronics. *ACS Nano* **8**, 10973-10979, doi:10.1021/nn504883m (2014).
101 Zhu, Z. *et al.* Hybrid transparent conductive electrodes with copper nanowires embedded in a zinc oxide matrix and protected by reduced graphene oxide platelets. *Journal of Applied Physics* **119**, 085303, doi:doi:http://dx.doi.org/10.1063/1.4942213 (2016).
102 Dou, L. *et al.* Solution-Processed Copper/Reduced-Graphene-Oxide Core/Shell Nanowire Transparent Conductors. *ACS Nano* **10**, 2600-2606, doi:10.1021/acsnano.5b07651 (2016).
103 Zhang, W. *et al.* Bridging Oriented Copper Nanowire–Graphene Composites for Solution-Processable, Annealing-Free, and Air-Stable Flexible Electrodes. *ACS Applied Materials & Interfaces* **8**, 1733-1741, doi:10.1021/acsami.5b09337 (2016).
104 Hsu, P.-C. *et al.* Passivation Coating on Electrospun Copper Nanofibers for Stable Transparent Electrodes. *ACS Nano* **6**, 5150-5156, doi:10.1021/nn300844g (2012).
105 Wang, C. *et al.* Multimetallic Au/FePt3 Nanoparticles as Highly Durable Electrocatalyst. *Nano Letters* **11**, 919-926, doi:10.1021/nl102369k (2010).
106 Guo, H. *et al.* Controllable synthesis of Cu-Ni core-shell nanoparticles and nanowires with tunable magnetic properties. *Chemical Communications* **52**, 6918-6921, doi:10.1039/c6cc02868c (2016).

107 Zhang, L. *et al.* Cu2+-Assisted Synthesis of Hexoctahedral Au–Pd Alloy Nanocrystals with High-Index Facets. *Journal of the American Chemical Society* **133**, 17114-17117, doi:10.1021/ja2063617 (2011).
108 Zeng, H. C. Synthesis and self-assembly of complex hollow materials. *Journal of Materials Chemistry* **21**, 7511-7526, doi:10.1039/c1jm10499c (2011).
109 Aranishi, K., Jiang, H.-L., Akita, T., Haruta, M. & Xu, Q. One-step synthesis of magnetically recyclable Au/Co/Fe triple-layered core-shell nanoparticles as highly efficient catalysts for the hydrolytic dehydrogenation of ammonia borane. *Nano Research* **4**, 1233-1241, doi:10.1007/s12274-011-0174-1 (2011).
110 Duan, X. & Lieber, C. M. Laser-Assisted Catalytic Growth of Single Crystal GaN Nanowires. *Journal of the American Chemical Society* **122**, 188-189, doi:10.1021/ja993713u (1999).
111 Jiang, H.-L., Akita, T., Ishida, T., Haruta, M. & Xu, Q. Synergistic Catalysis of Au@Ag Core−Shell Nanoparticles Stabilized on Metal−Organic Framework. *Journal of the American Chemical Society* **133**, 1304-1306, doi:10.1021/ja1099006 (2011).
112 Alayoglu, S., Nilekar, A. U., Mavrikakis, M. & Eichhorn, B. Ru-Pt core-shell nanoparticles for preferential oxidation of carbon monoxide in hydrogen. *Nat Mater* **7**, 333-338, doi:http://www.nature.com/nmat/journal/v7/n4/suppinfo/nmat2156_S1.html (2008).
113 Wei, Y.-C., Liu, C.-W. & Wang, K.-W. Improvement of oxygen reduction reaction and methanol tolerance characteristics for PdCo electrocatalysts by Au alloying and CO treatment. *Chemical Communications* **47**, 11927-11929, doi:10.1039/c1cc15110j (2011).
114 Tian, B. *et al.* Coaxial silicon nanowires as solar cells and nanoelectronic power sources. *Nature* **449**, 885-889, doi:http://www.nature.com/nature/journal/v449/n7164/suppinfo/nature06181_S1.html (2007).
115 Xu, Y. *et al.* Facile one-step room-temperature synthesis of Pt3Ni nanoparticle networks with improved electro-catalytic properties. *Chemical Communications* **48**, 2665-2667, doi:10.1039/c2cc16798k (2012).
116 Yoo, W.-J., Miyamura, H. & Kobayashi, S. Polymer-Incarcerated Gold− Palladium Nanoclusters with Boron on Carbon: A Mild and Efficient Catalyst for the Sequential Aerobic Oxidation− Michael Addition of 1, 3-Dicarbonyl Compounds to Allylic Alcohols. *Journal of the American Chemical Society* **133**, 3095-3103 (2011).
117 Gu, X., Lu, Z.-H., Jiang, H.-L., Akita, T. & Xu, Q. Synergistic Catalysis of Metal–Organic Framework-Immobilized Au–Pd Nanoparticles in Dehydrogenation of Formic Acid for Chemical Hydrogen Storage. *Journal of the American Chemical Society* **133**, 11822-11825, doi:10.1021/ja200122f (2011).
118 Cheng, K. & Sun, S. Recent advances in syntheses and therapeutic applications of multifunctional porous hollow nanoparticles. *Nano Today* **5**, 183-196, doi:http://dx.doi.org/10.1016/j.nantod.2010.04.002 (2010).
119 Zhang, Q., Wang, W., Goebl, J. & Yin, Y. Self-templated synthesis of hollow nanostructures. *Nano Today* **4**, 494-507, doi:http://dx.doi.org/10.1016/j.nantod.2009.10.008 (2009).
120 An, K. & Hyeon, T. Synthesis and biomedical applications of hollow nanostructures. *Nano Today* **4**, 359-373, doi:http://dx.doi.org/10.1016/j.nantod.2009.06.013 (2009).

121 Lehoux, A. *et al.* Tuning the Porosity of Bimetallic Nanostructures by a Soft Templating Approach. *Advanced Functional Materials* **22**, 4900-4908, doi:10.1002/adfm.201200666 (2012).
122 Zhang, S. & Zeng, H. C. Solution-Based Epitaxial Growth of Magnetically Responsive Cu@Ni Nanowires. *Chemistry of Materials* **22**, 1282-1284, doi:10.1021/cm903105f (2010).
123 Hwang, Y. J., Boukai, A. & Yang, P. High Density n-Si/n-TiO2 Core/Shell Nanowire Arrays with Enhanced Photoactivity. *Nano Letters* **9**, 410-415, doi:10.1021/nl8032763 (2008).
124 Liu, Z., Elbert, D., Chien, C.-L. & Searson, P. C. FIB/TEM Characterization of the Composition and Structure of Core/Shell Cu−Ni Nanowires. *Nano Letters* **8**, 2166-2170, doi:10.1021/nl080492u (2008).
125 Ghosh Chaudhuri, R. & Paria, S. Core/Shell Nanoparticles: Classes, Properties, Synthesis Mechanisms, Characterization, and Applications. *Chemical reviews* **112**, 2373-2433, doi:10.1021/cr100449n (2012).
126 Yan, J.-M., Zhang, X.-B., Akita, T., Haruta, M. & Xu, Q. One-Step Seeding Growth of Magnetically Recyclable Au@Co Core−Shell Nanoparticles: Highly Efficient Catalyst for Hydrolytic Dehydrogenation of Ammonia Borane. *Journal of the American Chemical Society* **132**, 5326-5327, doi:10.1021/ja910513h (2010).
127 Peng, Z. & Yang, H. Designer platinum nanoparticles: Control of shape, composition in alloy, nanostructure and electrocatalytic property. *Nano Today* **4**, 143-164, doi:http://dx.doi.org/10.1016/j.nantod.2008.10.010 (2009).
128 Xia, Y., Xia, X. & Peng, H.-C. Shape-Controlled Synthesis of Colloidal Metal Nanocrystals: Thermodynamic versus Kinetic Products. *Journal of the American Chemical Society* **137**, 7947-7966, doi:10.1021/jacs.5b04641 (2015).
129 Gilroy, K. D., Ruditskiy, A., Peng, H.-C., Qin, D. & Xia, Y. Bimetallic Nanocrystals: Syntheses, Properties, and Applications. *Chemical reviews*, doi:10.1021/acs.chemrev.6b00211 (2016).
130 Gibilaro, M., Massot, L., Chamelot, P. & Taxil, P. Co-reduction of aluminium and lanthanide ions in molten fluorides: Application to cerium and samarium extraction from nuclear wastes. *Electrochimica Acta* **54**, 5300-5306, doi:http://dx.doi.org/10.1016/j.electacta.2009.01.074 (2009).
131 Sun, Y. & Xia, Y. Increased Sensitivity of Surface Plasmon Resonance of Gold Nanoshells Compared to That of Gold Solid Colloids in Response to Environmental Changes. *Analytical Chemistry* **74**, 5297-5305, doi:10.1021/ac0258352 (2002).
132 Kim, K., Kim, K. L. & Shin, K. S. Coreduced Pt/Ag Alloy Nanoparticles: Surface-Enhanced Raman Scattering and Electrocatalytic Activity. *The Journal of Physical Chemistry C* **115**, 23374-23380, doi:10.1021/jp2063707 (2011).
133 Marcus, R. A. Electron transfer reactions in chemistry. Theory and experiment. *Reviews of Modern Physics* **65**, 599-610 (1993).
134 Kim, D., Resasco, J., Yu, Y., Asiri, A. M. & Yang, P. Synergistic geometric and electronic effects for electrochemical reduction of carbon dioxide using gold–copper bimetallic nanoparticles. *Nature communications* **5** (2014).
135 Liu, Y. *et al.* Composition-Controlled Synthesis of Bimetallic PdPt Nanoparticles and Their Electro-oxidation of Methanol. *Chemistry of Materials* **23**, 4199-4203, doi:10.1021/cm2014785 (2011).
136 Hong, X. *et al.* Ultrathin Au-Ag bimetallic nanowires with Coulomb blockade effects. *Chemical Communications* **47**, 5160-5162, doi:10.1039/c1cc10903k (2011).

137 Krichevski, O., Tirosh, E. & Markovich, G. Formation of Gold−Silver Nanowires in Thin Surfactant Solution Films. *Langmuir* **22**, 867-870, doi:10.1021/la051618v (2006).
138 Peng, Z., You, H. & Yang, H. Composition-Dependent Formation of Platinum Silver Nanowires. *ACS Nano* **4**, 1501-1510, doi:10.1021/nn9016795 (2010).
139 Habas, S. E., Lee, H., Radmilovic, V., Somorjai, G. A. & Yang, P. Shaping binary metal nanocrystals through epitaxial seeded growth. *Nat Mater* **6**, 692-697, doi:http://www.nature.com/nmat/journal/v6/n9/suppinfo/nmat1957_S1.html (2007).
140 Gao , C. *et al.* Highly Stable Silver Nanoplates for Surface Plasmon Resonance Biosensing. *Angewandte Chemie International Edition* **51**, 5629-5633, doi:10.1002/anie.201108971 (2012).
141 Li, C., Sun, L., Sun, Y. & Teranishi, T. One-Pot Controllable Synthesis of Au@Ag Heterogeneous Nanorods with Highly Tunable Plasmonic Absorption. *Chemistry of Materials* **25**, 2580-2590, doi:10.1021/cm400392e (2013).
142 Chen, Z., Ye, S., Stewart, I. E. & Wiley, B. J. Copper Nanowire Networks with Transparent Oxide Shells That Prevent Oxidation without Reducing Transmittance. *ACS Nano* **8**, 9673-9679, doi:10.1021/nn504308n (2014).
143 Song, J., Li, J., Xu, J. & Zeng, H. Superstable Transparent Conductive Cu@Cu4Ni Nanowire Elastomer Composites against Oxidation, Bending, Stretching, and Twisting for Flexible and Stretchable Optoelectronics. *Nano Letters* **14**, 6298-6305, doi:10.1021/nl502647k (2014).
144 Mehta, R., Chugh, S. & Chen, Z. Enhanced Electrical and Thermal Conduction in Graphene-Encapsulated Copper Nanowires. *Nano Letters* **15**, 2024-2030, doi:10.1021/nl504889t (2015).
145 Marcus, R. A. Exchange reactions and electron transfer reactions including isotopic exchange. Theory of oxidation-reduction reactions involving electron transfer. Part 4.-A statistical-mechanical basis for treating contributions from solvent, ligands, and inert salt. *Discussions of the Faraday Society* **29**, 21-31, doi:10.1039/df9602900021 (1960).
146 Xu, D., Bliznakov, S., Liu, Z., Fang, J. & Dimitrov, N. Composition-Dependent Electrocatalytic Activity of Pt-Cu Nanocube Catalysts for Formic Acid Oxidation. *Angewandte Chemie International Edition* **49**, 1282-1285, doi:10.1002/anie.200905248 (2010).
147 Tao, A., Sinsermsuksakul, P. & Yang, P. Polyhedral Silver Nanocrystals with Distinct Scattering Signatures. *Angewandte Chemie International Edition* **45**, 4597-4601, doi:10.1002/anie.200601277 (2006).
148 Harris, P. J. F. Sulphur-induced faceting of platinum catalyst particles. *Nature* **323**, 792-794 (1986).
149 Lévy, R. *et al.* Rational and Combinatorial Design of Peptide Capping Ligands for Gold Nanoparticles. *Journal of the American Chemical Society* **126**, 10076-10084, doi:10.1021/ja0487269 (2004).
150 Raveendran, P., Fu, J. & Wallen, S. L. Completely “Green” Synthesis and Stabilization of Metal Nanoparticles. *Journal of the American Chemical Society* **125**, 13940-13941, doi:10.1021/ja029267j (2003).
151 Yin, A.-X., Min, X.-Q., Zhang, Y.-W. & Yan, C.-H. Shape-Selective Synthesis and Facet-Dependent Enhanced Electrocatalytic Activity and Durability of Monodisperse Sub-10 nm Pt−Pd Tetrahedrons and Cubes. *Journal of the American Chemical Society* **133**, 3816-3819, doi:10.1021/ja200329p (2011).

152 Hong, W., Wang, J. & Wang, E. Facile synthesis of PtCu nanowires with enhanced electrocatalytic activity. *Nano Research* **8**, 2308-2316, doi:10.1007/s12274-015-0741-y (2015).
153 Becknell, N. *et al.* Atomic Structure of Pt3Ni Nanoframe Electrocatalysts by in Situ X-ray Absorption Spectroscopy. *Journal of the American Chemical Society* **137**, 15817-15824, doi:10.1021/jacs.5b09639 (2015).
154 Huang, X. *et al.* <div xmlns="http://www.w3.org/1999/xhtml">High-performance transition metal–doped Pt₃Ni octahedra for oxygen reduction reaction</div&gt. *Science* **348**, 1230 (2015).
155 Zheng, Z., Tachikawa, T. & Majima, T. Single-Particle Study of Pt-Modified Au Nanorods for Plasmon-Enhanced Hydrogen Generation in Visible to Near-Infrared Region. *Journal of the American Chemical Society* **136**, 6870-6873, doi:10.1021/ja502704n (2014).
156 Jakšić, M. M. Hypo–hyper-d-electronic interactive nature of synergism in catalysis and electrocatalysis for hydrogen reactions. *Electrochimica Acta* **45**, 4085-4099, doi:http://dx.doi.org/10.1016/S0013-4686(00)00525-9 (2000).
157 Raj, I. A. & Vasu, K. I. Transition metal-based hydrogen electrodes in alkaline solution — electrocatalysis on nickel based binary alloy coatings. *Journal of Applied Electrochemistry* **20**, 32-38, doi:10.1007/bf01012468 (1990).
158 Zarick, H. F. *et al.* Improving Light Harvesting in Dye-Sensitized Solar Cells Using Hybrid Bimetallic Nanostructures. *ACS Photonics* **3**, 385-394, doi:10.1021/acsphotonics.5b00552 (2016).
159 Wang, M. *et al.* Ratio-Controlled Synthesis of CuNi Octahedra and Nanocubes with Enhanced Catalytic Activity. *Journal of the American Chemical Society* **137**, 14027-14030, doi:10.1021/jacs.5b08289 (2015).
160 McKone, J. R., Sadtler, B. F., Werlang, C. A., Lewis, N. S. & Gray, H. B. Ni–Mo Nanopowders for Efficient Electrochemical Hydrogen Evolution. *ACS Catalysis* **3**, 166-169, doi:10.1021/cs300691m (2013).
161 Wang, Y. *et al.* A 3D Nanoporous Ni–Mo Electrocatalyst with Negligible Overpotential for Alkaline Hydrogen Evolution. *ChemElectroChem* **1**, 1138-1144, doi:10.1002/celc.201402089 (2014).
162 Gong, M. *et al.* Nanoscale nickel oxide/nickel heterostructures for active hydrogen evolution electrocatalysis. *Nat Commun* **5**, doi:10.1038/ncomms5695 (2014).
163 Tavakkoli, M. *et al.* Single-Shell Carbon-Encapsulated Iron Nanoparticles: Synthesis and High Electrocatalytic Activity for Hydrogen Evolution Reaction. *Angewandte Chemie International Edition* **54**, 4535-4538, doi:10.1002/anie.201411450 (2015).
164 Yang, H.-J., He, S.-Y. & Tuan, H.-Y. Self-Seeded Growth of Five-Fold Twinned Copper Nanowires: Mechanistic Study, Characterization, and SERS Applications. *Langmuir* **30**, 602-610, doi:10.1021/la4036198 (2014).
165 Won, Y. *et al.* Annealing-free fabrication of highly oxidation-resistive copper nanowire composite conductors for photovoltaics. *NPG Asia Mater* **6**, e105, doi:10.1038/am.2014.36 (2014).
166 Pacholski, C., Kornowski, A. & Weller, H. Self-Assembly of ZnO: From Nanodots to Nanorods. *Angewandte Chemie International Edition* **41**, 1188-1191, doi:10.1002/1521-3773(20020402)41:7<1188::aid-anie1188>3.0.co;2-5 (2002).
167 Li, P. *et al.* Solvents Induced ZnO Nanoparticles Aggregation Associated with Their Interfacial Effect on Organic Solar Cells. *ACS Applied Materials & Interfaces* **6**, 18172-18179, doi:10.1021/am5051789 (2014).

168 Blythe, A. R. Measurement Techniques for Polymeric Solids Electrical resistivity measurements of polymer materials. *Polymer Testing* **4**, 195-209, doi:http://dx.doi.org/10.1016/0142-9418(84)90012-6 (1984).
169 Liu, Z. *et al.* Synthesis of Copper Nanowires via a Complex-Surfactant-Assisted Hydrothermal Reduction Process. *The Journal of Physical Chemistry B* **107**, 12658-12661, doi:10.1021/jp036023s (2003).
170 Ye, E., Zhang, S.-Y., Liu, S. & Han, M.-Y. Disproportionation for Growing Copper Nanowires and their Controlled Self-Assembly Facilitated by Ligand Exchange. *Chemistry – A European Journal* **17**, 3074-3077, doi:10.1002/chem.201002987 (2011).
171 Battaglia, D. & Peng, X. Formation of High Quality InP and InAs Nanocrystals in a Noncoordinating Solvent. *Nano Letters* **2**, 1027-1030, doi:10.1021/nl025687v (2002).
172 Yu, W. W. & Peng, X. Formation of high-quality CdS and other II–VI semiconductor nanocrystals in noncoordinating solvents: tunable reactivity of monomers. *Angewandte Chemie International Edition* **41**, 2368-2371 (2002).
173 Al-Salim, N., Young, A. G., Tilley, R. D., McQuillan, A. J. & Xia, J. Synthesis of CdSeS Nanocrystals in Coordinating and Noncoordinating Solvents: Solvent's Role in Evolution of the Optical and Structural Properties. *Chemistry of Materials* **19**, 5185-5193, doi:10.1021/cm070818k (2007).
174 Bullen, C. R. & Mulvaney, P. Nucleation and Growth Kinetics of CdSe Nanocrystals in Octadecene. *Nano Letters* **4**, 2303-2307, doi:10.1021/nl0496724 (2004).
175 Li, L. S., Pradhan, N., Wang, Y. & Peng, X. High Quality ZnSe and ZnS Nanocrystals Formed by Activating Zinc Carboxylate Precursors. *Nano Letters* **4**, 2261-2264, doi:10.1021/nl048650e (2004).
176 Wang, W., Banerjee, S., Jia, S., Steigerwald, M. L. & Herman, I. P. Ligand Control of Growth, Morphology, and Capping Structure of Colloidal CdSe Nanorods. *Chemistry of Materials* **19**, 2573-2580, doi:10.1021/cm0705791 (2007).
177 Dumestre, F. *et al.* Shape control of thermodynamically stable cobalt nanorods through organometallic chemistry. *Angewandte Chemie* **114**, 4462-4465 (2002).
178 Jana, N. R., Chen, Y. & Peng, X. Size- and Shape-Controlled Magnetic (Cr, Mn, Fe, Co, Ni) Oxide Nanocrystals via a Simple and General Approach. *Chemistry of Materials* **16**, 3931-3935, doi:10.1021/cm049221k (2004).
179 Lu, X., Yavuz, M. S., Tuan, H.-Y., Korgel, B. A. & Xia, Y. Ultrathin Gold Nanowires Can Be Obtained by Reducing Polymeric Strands of Oleylamine−AuCl Complexes Formed via Aurophilic Interaction. *Journal of the American Chemical Society* **130**, 8900-8901, doi:10.1021/ja803343m (2008).
180 Du, Y. *et al.* A general method for the large-scale synthesis of uniform ultrathin metal sulphide nanocrystals. *Nat Commun* **3**, 1177, doi:http://www.nature.com/ncomms/journal/v3/n10/suppinfo/ncomms2181_S1.html (2012).
181 Larche, F. C., El Qebbaj, S. & Marignan, J. The swelling of a lamellar lyotropic liquid crystal by an alkane. *The Journal of Physical Chemistry* **90**, 707-710, doi:10.1021/j100276a045 (1986).
182 Lagaly, G. Interaction of alkylamines with different types of layered compounds. *Solid State Ionics* **22**, 43-51 (1986).
183 Jiu, J., Murai, K., Kim, D., Kim, K. & Suganuma, K. Preparation of Ag nanorods with high yield by polyol process. *Materials Chemistry and Physics* **114**, 333-338 (2009).

184 Generalova, A. N. *et al.* Highly fluorescent ethyl cellulose nanoparticles containing embedded semiconductor nanocrystals. *Colloids and Surfaces A: Physicochemical and Engineering Aspects* **342**, 59-64, doi:http://dx.doi.org/10.1016/j.colsurfa.2009.04.007 (2009).
185 Wang, H. *et al.* Transparent, flexible and luminescent composite films by incorporating CuInS2 based quantum dots into a cyanoethyl cellulose matrix. *RSC Advances* **2**, 2675-2677, doi:10.1039/c2ra01359b (2012).
186 Mayousse, C., Celle, C., Carella, A. & Simonato, J.-P. Synthesis and purification of long copper nanowires. Application to high performance flexible transparent electrodes with and without PEDOT:PSS. *Nano Research* **7**, 315-324, doi:10.1007/s12274-013-0397-4 (2014).
187 Zhu, R. *et al.* Fused Silver Nanowires with Metal Oxide Nanoparticles and Organic Polymers for Highly Transparent Conductors. *ACS Nano* **5**, 9877-9882, doi:10.1021/nn203576v (2011).
188 Kim, A., Won, Y., Woo, K., Kim, C.-H. & Moon, J. Highly Transparent Low Resistance ZnO/Ag Nanowire/ZnO Composite Electrode for Thin Film Solar Cells. *ACS Nano* **7**, 1081-1091, doi:10.1021/nn305491x (2013).
189 Singh, M. *et al.* Silver Nanowires Binding with Sputtered ZnO to Fabricate Highly Conductive and Thermally Stable Transparent Electrode for Solar Cell Applications. *ACS Applied Materials & Interfaces* **8**, 12764-12771, doi:10.1021/acsami.6b01506 (2016).
190 Chakraborty, M., Chowdhury, D. & Chattopadhyay, A. Spin-Coating of Polystyrene Thin Films as an Advanced Undergraduate Experiment. *Journal of Chemical Education* **80**, 806, doi:10.1021/ed080p806 (2003).
191 Giordano, M., Russo, M., Cusano, A., Mensitieri, G. & Guerra, G. Syndiotactic polystyrene thin film as sensitive layer for an optoelectronic chemical sensing device. *Sensors and Actuators B: Chemical* **109**, 177-184, doi:http://dx.doi.org/10.1016/j.snb.2004.02.053 (2005).
192 Smith, G. J. The rate constant for the reaction of the singlet state of coronene with oxygen in non-polar solvents. *Journal of Photochemistry* **22**, 51-54, doi:http://dx.doi.org/10.1016/0047-2670(93)80007-C (1983).
193 Yamauchi, T. *et al.* Magnetic Cu-Ni (core-shell) nanoparticles in a one-pot reaction under microwave irradiation. *Nanoscale* **2**, 515-523, doi:10.1039/b9nr00302a (2010).
194 Smith, A. M., Kast, M. G., Nail, B. A., Aloni, S. & Boettcher, S. W. A planar-defect-driven growth mechanism of oxygen deficient tungsten oxide nanowires. *Journal of Materials Chemistry A* **2**, 6121-6129, doi:10.1039/c3ta14163b (2014).
195 Wei Wang, J. *et al.* Atomic-scale dynamic process of deformation-induced stacking fault tetrahedra in gold nanocrystals. *Nat Commun* **4**, doi:10.1038/ncomms3340 (2013).
196 Pilling, N. B. & Bedworth, R. E. Oxidation of Copper-Nickel Alloys at High Temperatures. *Industrial & Engineering Chemistry* **17**, 372-376, doi:10.1021/ie50184a013 (1925).
197 Zeng, M. & Li, Y. Recent advances in heterogeneous electrocatalysts for the hydrogen evolution reaction. *Journal of Materials Chemistry A* **3**, 14942-14962, doi:10.1039/c5ta02974k (2015).
198 Conway, B. E. & Tilak, B. V. Interfacial processes involving electrocatalytic evolution and oxidation of H2, and the role of chemisorbed H. *Electrochimica Acta* **47**, 3571-3594, doi:http://dx.doi.org/10.1016/S0013-4686(02)00329-8 (2002).

199 Conway, B. E. *Modern Aspects of Electrochemistry, Number 38*. (Springer Science & Business Media, 2004).

200 Nørskov, J. K. *et al.* Trends in the Exchange Current for Hydrogen Evolution. *Journal of The Electrochemical Society* **152**, J23-J26, doi:10.1149/1.1856988 (2005).

201 Jaramillo, T. F. *et al.* <div xmlns="http://www.w3.org/1999/xhtml">Identification of Active Edge Sites for Electrochemical H₂ Evolution from MoS₂ Nanocatalysts</div&gt. *Science* **317**, 100 (2007).

202 Neyerlin, K. C., Gu, W., Jorne, J. & Gasteiger, H. A. Study of the Exchange Current Density for the Hydrogen Oxidation and Evolution Reactions. *Journal of The Electrochemical Society* **154**, B631-B635 (2007).

203 Marković, N. M., Grgur, B. N. & Ross, P. N. Temperature-Dependent Hydrogen Electrochemistry on Platinum Low-Index Single-Crystal Surfaces in Acid Solutions. *The Journal of Physical Chemistry B* **101**, 5405-5413, doi:10.1021/jp970930d (1997).

204 Sheng, W., Gasteiger, H. A. & Shao-Horn, Y. Hydrogen Oxidation and Evolution Reaction Kinetics on Platinum: Acid vs Alkaline Electrolytes. *Journal of The Electrochemical Society* **157**, B1529-B1536, doi:10.1149/1.3483106 (2010).